

Probing Magnetic Excitations and Correlations in Single and Coupled Spin Systems with Scanning Tunneling Spectroscopy

Markus Ternes^{a,*}

^aMax-Planck Institute for Solid State Research, Heisenbergstr. 1, D-70569 Stuttgart, Germany

Abstract

Spectroscopic measurements with low-temperature scanning tunneling microscopes have been used very successfully for studying not only individual atomic or molecular spins on surfaces but also complexly designed coupled systems. The symmetry breaking of the supporting surface induces magnetic anisotropy which lead to characteristic fingerprints in the spectrum of the differential conductance and can be well understood with simple model Hamiltonians. Furthermore, correlated many-particle states can emerge due to the interaction with itinerant electrons of the electrodes, making these systems ideal prototypical quantum systems. In this manuscript more complex bipartite and spin-chains will be discussed additionally. Their spectra enable to determine precisely the nature of the interactions between the spins which can lead to the formation of new quantum states which emerge by interatomic entanglement.

Keywords: scanning tunneling spectroscopy, inelastic tunneling spectroscopy, Kondo effect, magnetic anisotropy, spin-flip spectroscopy, coupled spin systems, spin chains

Contents

1	Introduction	2
2	The magnetic anisotropy in single spins	4
2.1	Modifying the spin state and anisotropy in CoH_x complexes	5
2.2	Renormalization of the eigenstate energies	9
2.3	The anisotropies of Fe and Mn embedded in CuN	10
3	The Kondo effect	13
3.1	The weak coupling limit in an organic radical	14
3.2	The limit of the perturbative approach	16
3.3	The strong coupling regime	20
3.4	Spin polarization of the split Kondo peak	22
4	Coupled spin systems	25
4.1	The spectrum of a prototypical molecular magnet	25
4.2	Coupling between a spin 1 and a spin $1/2$	27
4.3	Fe-Co dimers on Cu_2N	31
4.4	Co-Co dimers on Cu_2N	33
4.5	Entanglement and the zero-energy peak in spin chains	35
5	Summary and outlook	39

*Corresponding author

Email address: m.ternes@fkf.mpg.de (Markus Ternes)

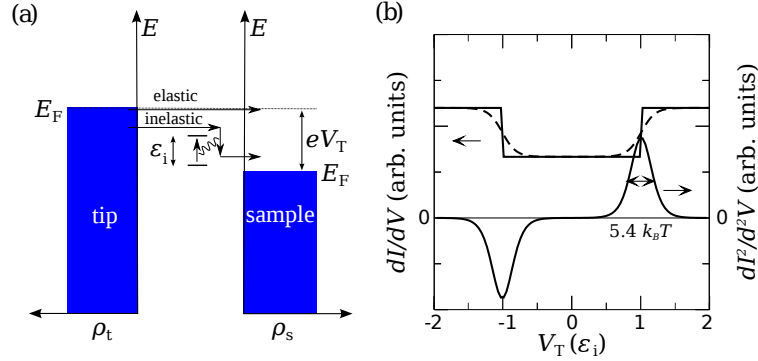


Figure 1: **(a)** Schematic view of the tunneling process between the electrodes of an idealized tip and sample with their constant densities of states ρ_t and ρ_s , respectively: In addition to the elastic tunneling current, an inelastic channel may open at a bias $|eV_T| \geq \varepsilon_i$ with ε_i as the energy difference between the ground and an excited internal state. Under this circumstances an electron crossing the barrier can change its quantum state by losing part of its energy and exciting an internal degree of freedom, for example, the spin orientation of a magnetic adsorbate on the surface. **(b)** Schematic differential conductance, dI/dV (upper curve) and dI^2/d^2V (lower curve), spectra of an inelastic tunneling process. Symmetrically around E_F a step like structure at a bias voltage $|eV_T| = \varepsilon_i$ is detected in the dI/dV curve. This is smeared out at non-zero temperature (dashed line) leading to peaks with a width of $5.4k_B T$ in the dI^2/d^2V curve. Figure adapted from reference [17].

1. Introduction

The transfer of electrons between metallic leads separated by vacuum or an insulating gap is classically forbidden. However, it becomes possible if the size of the gap is reduced to the scale of a few Angstroms due to the tunneling effect. This entirely quantum mechanical effect, which allows the electrons to cross the forbidden region, was already discussed in the early days of quantum mechanics [1] and first observed in the 1960s on planar superconducting – oxide – normal conducting junctions [2, 3].

In general, the electron transport in such tunnel junctions can be divided into two distinct classes: Elastic tunneling in which an applied bias drives electrons from the many states of one electrode to cross the junction without interaction with the local environment and inelastic tunneling, where the electrons interact with the junction environment and change their energy, phase, or angular momentum. These inelastic processes leave characteristic fingerprints in bias dependent conductance measurements. In particular, when discrete states are excited during tunneling and the tunneling electron loses partly its kinetic energy, a bias threshold voltage can be observed below which the inelastic process cannot occur (Figure 1). In this sense inelastic tunneling spectroscopy (IETS) is complementary to far-field methods such as high resolution electron energy-loss (HREELS), infrared reflection adsorption (IRRAS), Raman spectroscopy, or inelastic neutron spectroscopy [4, 5] and has been performed in planar tunnel junctions to detect vibrational excitation modes of molecules embedded in the junction for almost 50 years [6, 7, 8, 9, 10, 11]. Remarkably, besides molecular vibrations, excitations due to the interaction of electrons with localized magnetic impurities have already been studied in these pioneering days leading to the discovery of anomalies in the density of states very close to the Fermi energy, which was shown to be due to the formation of a Kondo state and inelastic spin-flip excitations [12, 13, 14, 15, 16].

While planar tunnel junctions have the disadvantage of averaging over an ill-defined contact area, the development of the scanning tunneling microscope (STM) by Binnig, Rohrer, Gerber, and Weibull in the early 1980s [18, 19, 20] opened a entirely new world for tunneling experiments. Very soon it became clear that the STM, with its capability to atomically resolve metallic and semiconducting surfaces, would become a powerful tool for the analysis of surfaces and nanoscale structures down to the single molecule or atom level. Its discovery was awarded with the Nobel prize in a surprisingly short time of only 4 years after its first successful demonstration.

In the early days of STM, collective vibrational excitations at the surface of graphite were detected [21], however, it was clear that the true capability of the STM would lie in combining its spectroscopic possibilities with its inherent atomic resolution. Nevertheless, it took about 15 years of technology development before

the mechanical stability and electronic sensibility of the STM at cryogenic temperatures and in ultrahigh vacuum was high enough to make this dream reality.

The year 1998 brought two important experimental breakthroughs: The group around Wilson Ho at the Cornell University showed for the first time that IETS was possible on the single molecular level using the spatial resolution of the STM [22]. In their experiment they detected the vibrational excitations of an isolated acetylene (C_2H_2) molecule adsorbed on a Cu(100) surface. The detection of mechanical excitation in molecular systems, has since been applied to many quite different molecular systems ranging from diatomics like carbon monoxide [23, 24], metal hydride molecules [25], and molecular hydrogen [26, 27, 28] to complex molecules like porphyrins [29] and C_{60} bucky balls [30]. However, importantly for the work discussed in this manuscript, inelastic excitations can also be observed on individual spin systems as discovered by Andreas Heinrich and co-workers at IBM Almaden first on Mn atoms adsorbed on patches of Al_2O_3 on a NiAl surface [31]. As we will discuss in the following, spin excitation spectroscopy gives unparalleled access to the quantum nature of individual and coupled spin systems enabling the determination and manipulation of their spin states, their magnetic anisotropy, and their coupling with the environment; properties which are actually mutually interdependent.

The second breakthrough was the detection of the spectroscopic signature of the correlated many-particle Kondo state of individual magnetic atoms adsorbed on non-magnetic metal substrates. This discovery was made almost simultaneously by the group around Wolf-Dieter Schneider at the University Lausanne [32]¹ and the group around Michael Crommie at the University of Boston [38].

These two hallmarking observations are the foundation on which the work presented here is based. Both rely on the interaction of individual spins, i.e. atoms or molecules which have a magnetic moment, with the local environment as is schematically illustrated in figure 2. A paramagnetic atom with a total spin $S > 1/2$ has $2S + 1$ eigenstates which are indistinguishable in the gas phase when no external magnetic field is applied. Upon adsorption on the surface this situation changes. When the atom is physisorbed, the out-of-plane direction forms a distinct axis, different from all other directions. This symmetry breaking is the origin of magnetic anisotropy which lifts the degeneracy and defines the stability of a spin in a preferred direction [41] (figure 2a). In the case the atom is chemisorbed onto the surface, that means it forms covalent chemical bonds and is rather incorporated into the surface, complex molecular networks might form, further reducing the system's symmetry. Additionally, spin-orbit coupling, charge transfer, and delocalized spin polarization in the substrate influences the effective magnetism of the atom [42].

The influence of the magnetic anisotropy on the tunneling spectra will be briefly discussed in section 2. Here, we will additionally see how the strength of the direct exchange coupling between the localized magnetic moment and the itinerant electron bath of the substrate modifies the magnetic anisotropy via virtual coherences between the eigenstates [43, 44].

While the magnetic anisotropy removes the degeneracies of high spin systems, for half-integer spins Kramers theorem prevails the full lifting of all degeneracies [45]. In these systems every energy level is at least doubly degenerate at zero field. The ground state degeneracy has, in particular for $S = 1/2$ systems, dramatic consequences which leads to an entirely new area of physics in which correlations between the localized magnetic moment and the many electrons of the substrate form, at low enough temperature, a new singlet ground state creating a prominent resonance at the Fermi energy (see figure 2b) [46, 47]. Section 3 will discuss this Kondo effect in detail. Starting with the temperature and magnetic field dependence in the weak coupling limit which was first measured on an organic radical [48] we will elaborate a perturbative scattering model up to 3rd order in the exchange interaction and show under which circumstances the model breaks down and other, more sophisticated models have to be used [40]. Here, individual Co atoms on different substrates can act as examples for this strong coupling regime [49]. Intriguingly, Co atoms on a Cu_2N substrate possesses a spin of $S = 3/2$ and are thereby also influenced by the magnetic anisotropy leading to a directionally dependent magnetic field behavior [50]. Additionally, on this system the spin polarization of the split Kondo state was determined [51].

¹Note, that due to newer measurements which revealed that single Ce adatoms on Ag(111) are even at 5 K still very mobile [33, 34, 35, 36], the original publications was presumably measured on a small Ce cluster, which can indeed show a Kondo state [37].

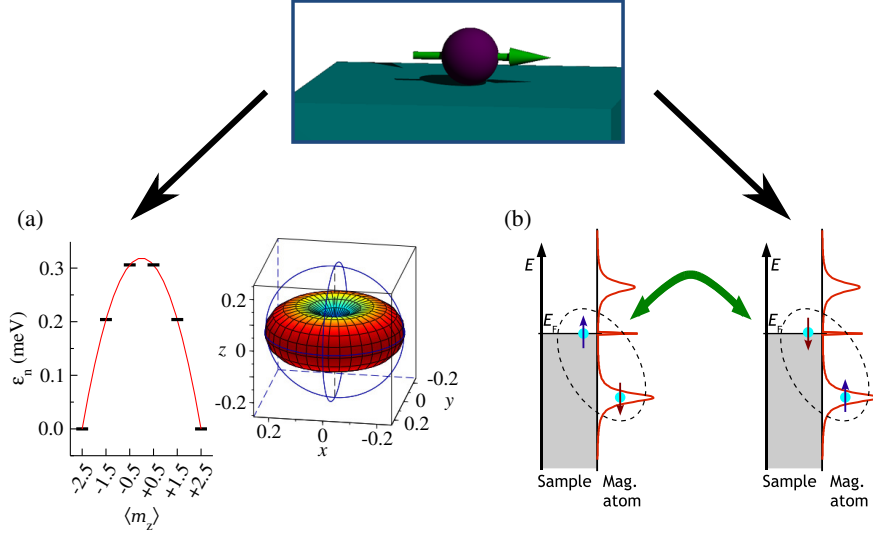


Figure 2: Schematic view of the emergent physical phenomena upon absorption of a paramagnetic spin onto a surface. **(a)** The surface breaks the symmetry and leads to magnetic anisotropy in which the spin prefers distinct alignments. As an example the energy level diagram for a Mn adatom on Cu_2N with axial anisotropy of $D = -40\mu\text{eV}$ is shown (left). Here, the projected magnetic moment m_z along the hard axis is a good quantum number allowing us to distinguish the 6 eigenstates of the effective spin $S = 5/2$ system. The visualization of the magnetic anisotropy shows the magnetic easy axis (z -axis) and the $x - y$ hard plane (right, scale in meV) [39, 40]. **(b)** Degenerate ground states, as for example in spin $S = 1/2$ systems (illustrated as singly occupied level below E_F), can interact with the electrons of the sample leading to the formation of a new singlet state in which the localized magnetic moment is screened by the many-electrons of the bath. This Kondo state leaves a characteristic signature in the quasiparticle excitation spectrum close to the Fermi energy E_F . Note that the processes (a) and (b) can compete against each other. Figure adapted from references [37] and [40].

After the discussion of the emergence of anisotropy and correlations in single spin systems, section 4 will discuss coupled systems containing more than one paramagnetic spin center. Starting with the prototypical molecular magnet $\text{Mn}_{12}\text{Acetate}_{16}$ which has a total ground state spin of $S_T = 10$ we will observe that S_T is not a conserved quantity and that spin excitations can change the total spin S_T leaving characteristic fingerprints in the IETS spectrum [52]. Afterward, spin dimer systems will be inspected with a particular focus on the description in the perturbative transport model [40, 53] and the appearance of different quantum phases in the two-impurity Kondo system. Last, coupled spin chains are discussed which are of particular interest due to the emergence of entanglement that can be directly observed in the zero-energy peak [54]. Finally, section 5 summarizes the manuscript and outlines possible routes for future research.

2. The magnetic anisotropy in single spins

Magnetic anisotropy defines the preferred directions in which the magnetic moment of a spin of strength S likes to be aligned and is crucial for the lifetime in which the direction of magnetization is maintained [41, 42, 55]. While a spin carrying atom in gas phase can not have any magnetic anisotropy due to its spherical symmetry, the situation changes when the spin is embedded into a crystal structure. The crystal field and the spin-orbit coupling lead to a lifting of the degeneracies. In general the crystal field spin Hamiltonian \hat{H}_{ani} can be perturbatively constructed from an infinite series of quadratic, cubic, etc. spin operators, which are usually expressed in Stevens operators \hat{O}_N^k to easily connect to point group symmetries [56]:

$$\hat{H}_{\text{ani}} = \sum_{\substack{N=2,4,\dots,2S \\ -N \leq k \leq N}} B_N^k \hat{O}_N^k, \quad (1)$$

with B_N^k as the parameters. As we will see, it is often a good approximation to assume the crystal field spin Hamiltonian to be only quadratic in the spin operators with a symmetric coupling matrix \mathbf{D} :

$$\hat{H}_{\text{ani}} = \hat{\mathbf{S}} \cdot \mathbf{D} \cdot \hat{\mathbf{S}} \equiv D\hat{S}_z^2 + E\left(\hat{S}_x^2 - \hat{S}_y^2\right), \quad (2)$$

where the scalar parameter D determines the axial and E the transverse anisotropy, and $\hat{\mathbf{S}} = (\hat{S}_x, \hat{S}_y, \hat{S}_z)^T$ is the total spin operator.

For adatoms on surfaces, a low coordination number and changes in hybridization can lead to a dramatic enhancement of magnetic anisotropy [57, 58, 59, 60] which have been shown to reach values of up to ≈ 60 meV for Co adatoms on MgO [60]. Additionally, different surface adsorption sites or the bonding to hydrogen alter the magnetic anisotropy or even the total spin of the adatoms [61, 62, 63, 44, 64, 65]. Furthermore, the exchange interaction with the substrate can affect the observed magnetic anisotropy as it has been found for 3d metal adatoms on Cu₂N islands on Cu(100) [43, 66, 67] or metal-hydrates on *h*-BN on Rh(111) [44]. For single molecule magnets containing 3d or 4f spin centers it is well known that chemical changes to the ligands surrounding the spin can affect the magnetic anisotropy [68, 69, 70]. However, the most important factor for creating and maintaining magnetic anisotropy in single molecule magnets remains a low coordination number and a high axial symmetry [60, 71, 72]. Under such conditions the symmetry-protected magnetic ground state of single Ho-atoms adsorbed on a double-layer of MgO on Ag(100) can lead to relaxation times of 1 h at a temperature of 2.5 K as recently observed in magnetic circular dichroism measurements [73].

In this section we will discuss the use of scanning tunneling spectroscopy to measure IETS on individual magnetic spin systems. Such measurements enable the determination of the total spin as well as the orientation and strength of the magnetic anisotropies. Additionally, we will show that a perturbative scattering model [40] can accurately reproduce the experimental observations enabling us to precisely measure the coupling to the underlying substrate. On hydrogenated metal complexes not only energetically low vibrational modes have been found [25, 74] but also a wide range of magnetic excitations have been detected [62, 63, 44, 64]. Therefore, we will focus on CoH_{*x*} complexes coupled to the spatially varying template *h*-BN/Rh(111) moiré as an example of hydrogenated metal complexes.

2.1. Modifying the spin state and anisotropy in CoH_{*x*} complexes

CoH_{*x*} ($x = 0 - 3$) complexes on the *h*-BN/Rh(111) moiré form when Co atoms from a metallic rod are deposited by an e-beam evaporator onto the cold ($T \approx 30$ K) surface together with residual hydrogen from the background vacuum [44]. The *h*-BN monolayer, a two dimensional material with a wide band gap, decouples the CoH_{*x*} from the underlying Rh(111) metal while the lattice mismatch leads to a spatial corrugation resulting in an enlarged supercell with 3.2 nm periodicity corresponding to 13 BN units on top of 12 Rh atoms [75, 76].

Figure 3a shows a typical STM constant-current topography of the *h*-BN/Rh(111) moiré with isolated CoH_{*x*} ($x = 1, 2$) complexes imaged as protrusions. Line profiles indicate that CoH_{*x*} can adsorb at multiple positions within the moiré (Figure 3b) [77, 44]. The differential conductance spectra, dI/dV , measured at low-temperature ($T = 1.4$ K) and zero magnetic field ($B = 0$ T) on these CoH_{*x*} complexes can be divided into two broad classes: a sharp peak centered at zero bias or two symmetric steps of increasing conductance at well-defined threshold energies (Figure 3c). The peak at zero bias is consistent with a spin $S = 1/2$ Kondo resonance which will be discussed in detail in section 3 while the steps correspond to the onset of inelastic excitations from the magnetic ground state to excited states. The observation of two steps hints towards an effective $S = 1$ system with zero-field splitting. The two lower spectra (Figure 3c, red and blue curves) are measured on CoH at different parts of the moiré and share the same overall characteristics but the step positions vary.

Employing density functional theory (DFT) performed by Oleg Brovko and Valerie Stepanyuk from the MPI Halle enables us to correlate the magnetic properties of the CoH_{*x*} with the local adsorption configuration [44]. The calculations show that adsorption in the BN hexagon, i.e. hollow site, is preferable for bare Co leading to a magnetic moment of 2.2 Bohr magnetons (μ_B). The addition of a hydrogen atom shifts the preferred adsorption site to N and concomitantly lowers the magnetic moment to $2.0\mu_B$, equivalent to a

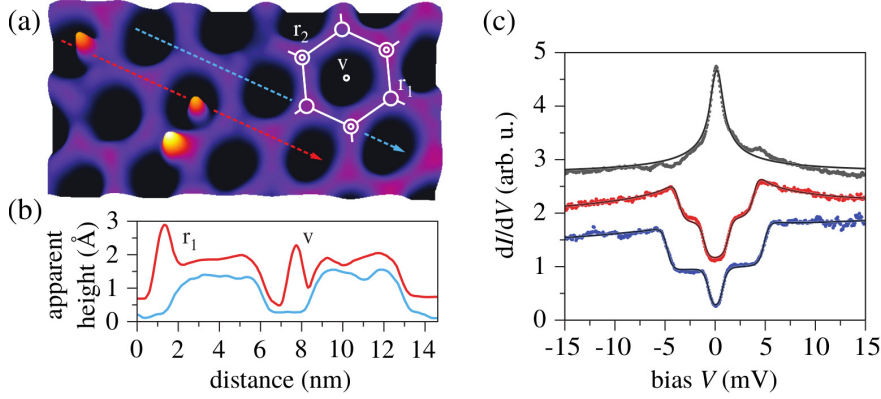


Figure 3: Cobalt hydrates adsorbed on a *h*-BN/Rh(111) surface. **(a)** Constant current STM topography with three CoH_x complexes (protrusions) adsorbed on different sites of the highly corrugated surface. (image size $15 \times 4 \text{ nm}^2$, $V = 100 \text{ mV}$, $I = 20 \text{ pA}$, $T = 1.4 \text{ K}$). High symmetry points of the moiré are marked by the white overlay. **(b)** Line profiles along the dashed lines indicated in (a) show two CoH_x systems with adsorption sites r_1 and v (red line) and a *h*-BN reference cut (blue line), offset by 0.5 \AA . **(c)** Differential conductance dI/dV curves measured on top of three different CoH_x systems (stabilization setpoint: $I = 500 \text{ pA}$, $V = -15 \text{ mV}$, $T = 1.4 \text{ K}$, curves vertically offset for clarity). The upper curve (grey) shows a spin $1/2$ Kondo resonance (see section 3) centered at zero bias. The two lower curves (red and blue) show step-like conductance increases symmetric around zero bias indicating a $S = 1$ system. Solid black lines are least-square fits using the perturbative transport model. Figure adapted from reference [44].

$3d^8$ configuration. The second hydrogen changes the picture significantly, with the $sp - d$ hybridization sufficient to bring the Co d -levels closer together, reducing the magnetic moment to $1.2\mu_B$ resulting in a $3d^9$ configuration [44].

An important consequence of the N adsorption site is the linear crystal field acting on the cobalt (i. e. N–Co–H) removing the 5-fold degeneracy of the d -levels. From these results and the spectroscopic observations we can identify CoH as an effective $S = 1$ and CoH_2 as an $S = 1/2$ Kondo system. The strong vertical bond between Co and N can be expected to provide the system with an out-of-plane magnetic anisotropy (Figure 4a). While the hydrogen is not rigidly pinned to the cobalt, tilting of the hydrogen combined with the underlying lattice mismatch reduces the C_{3v} symmetry and introduces small shifts in the d_{xz} , d_{yz} levels producing a non-negligible in-plane component of the anisotropy lifting all degeneracies of the spin system (Figure 4b).

To analyze the experimental data we use an impurity Hamiltonian which includes the Zeeman energy and the magnetic anisotropy (equation 2), and which is sufficient to fully explain the spectroscopic features observed in our scanning tunneling spectroscopy measurements [78, 50, 79, 43, 66, 40]:

$$\hat{H}_{\text{imp}} = g\mu_B \vec{B} \cdot \hat{\mathbf{S}} + D\hat{S}_z^2 + E(\hat{S}_x^2 - \hat{S}_y^2). \quad (3)$$

In this equation is g the gyromagnetic factor, μ_B the Bohr magneton, \vec{B} is the external applied magnetic field and D , E , and $\hat{\mathbf{S}}$ the axial and transverse anisotropy, and the total spin operator for the $S = 1$ spin with the components ($\hbar = 1$):

$$\hat{S}_x = \begin{pmatrix} 0 & \frac{1}{\sqrt{2}} & 0 \\ \frac{1}{\sqrt{2}} & 0 & \frac{1}{\sqrt{2}} \\ 0 & \frac{1}{\sqrt{2}} & 0 \end{pmatrix}, \quad \hat{S}_y = \begin{pmatrix} 0 & \frac{-i}{\sqrt{2}} & 0 \\ \frac{i}{\sqrt{2}} & 0 & \frac{-i}{\sqrt{2}} \\ 0 & \frac{i}{\sqrt{2}} & 0 \end{pmatrix}, \quad \hat{S}_z = \begin{pmatrix} 1 & 0 & 0 \\ 0 & 0 & 0 \\ 0 & 0 & -1 \end{pmatrix}. \quad (4)$$

In the absence of a magnetic field the three eigenvectors $|\Psi\rangle_i$ and eigenenergies ε_i of equation 3 are

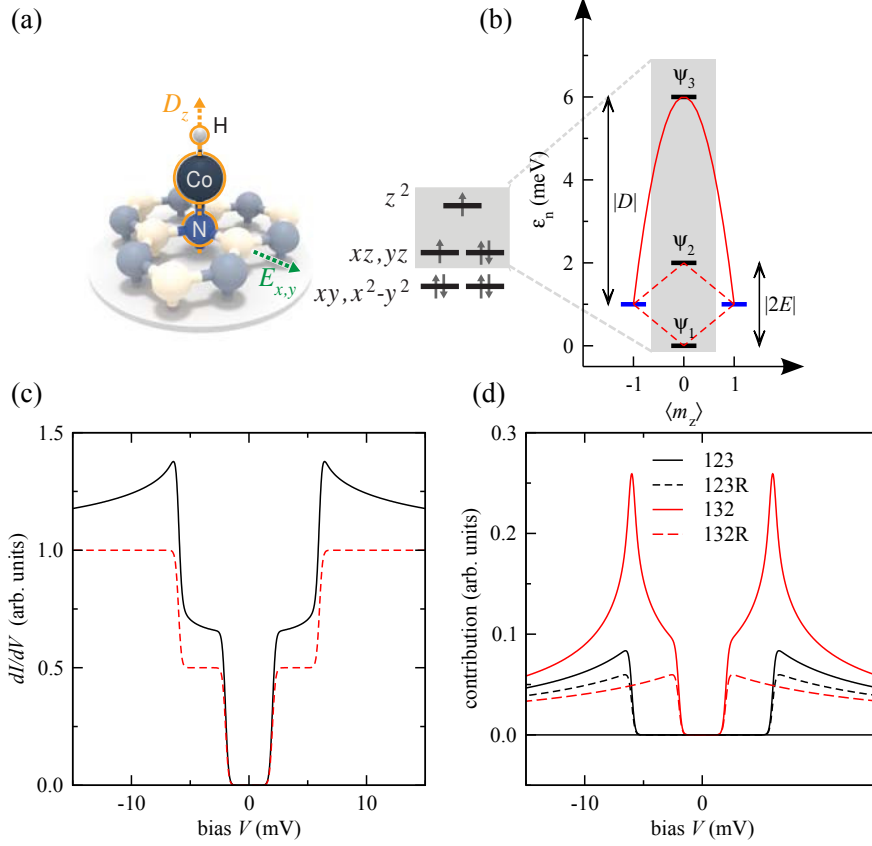


Figure 4: The magnetic properties and the tunneling spectra of CoH. **(a)** Ball and stick model of the adsorption of CoH on *h*-BN. The linear adsorption geometry of CoH on the N atom is emphasized and marks the main (axial) magnetic anisotropy (D) along the z -axis. **(b)** Additional transverse anisotropy (E) in the $x - y$ plane lifts all degeneracies at zero field. The plot shows the state energy over the m_z expectation value $\langle m_z \rangle = \text{tr}(\hat{S}_z |\Psi_i\rangle \langle \Psi_i|)$ with $D = -5$ meV and $E = 1$ meV as an example. **(c)** The total spectrum with $J\rho_0 = 0$ (dashed red line) and -0.1 (full black line) calculated for $T = 1$ K, $B = 0$ T. **(d)** The significant higher order processes where the digits refer to the visited eigenstates during the scattering process. Figure adapted from reference [44].

calculated in the m_z basis to

$$\begin{aligned}
 \varepsilon_1 &= 0, & |\Psi_1\rangle &= +\frac{1}{\sqrt{2}}|+1\rangle - \frac{1}{\sqrt{2}}|-1\rangle, \\
 \varepsilon_2 &= 2E, & |\Psi_2\rangle &= +\frac{1}{\sqrt{2}}|+1\rangle + \frac{1}{\sqrt{2}}|-1\rangle, \\
 \varepsilon_3 &= E - D, & |\Psi_3\rangle &= |0\rangle,
 \end{aligned}$$

as shown in figure 4b for hard axis anisotropy ($D < 0$) and non negligible transverse anisotropy ($E \neq 0$).

To calculate the tunneling spectrum we use a model based on the perturbative approach first established by Appelbaum, Anderson, and Kondo [46, 80, 81, 82] in which spin-flip scattering processes up to the 2nd order Born approximation are accounted for. While we will outline the main components of this model, a more detailed approach can be found in [40].

In this model the transition probability $W_{i \rightarrow f}$ for an electron to tunnel between tip and sample and

concomitantly change the spin state of the CoH complex from its initial (i) to its final (f) state is

$$W_{i \rightarrow f} \propto \left(|M_{i \rightarrow f}|^2 + \rho_0 J \sum_m \left(\frac{M_{i \rightarrow m} M_{m \rightarrow f} M_{f \rightarrow i}}{\varepsilon_i - \varepsilon_m} + \text{c. c.} \right) \right) \delta(\varepsilon_i - \varepsilon_f), \quad (5)$$

with $M_{i \rightarrow j}$ as the matrix elements given by the Kondo-like interaction of the scattering electron with the wavevector $|\varphi\rangle$ with the localized spin of the CoH complex

$$M_{i \rightarrow f} = \sum_{i', f'} \langle \varphi_{f'}, \Psi_f | \frac{1}{2} \hat{\sigma} \cdot \hat{\mathbf{S}} | \varphi_{i'}, \Psi_i \rangle. \quad (6)$$

In this equation $|\varphi_i, \Psi_i\rangle$ is the combined state vector of the localized $S = 1$ spin and the interaction electron. $\hat{\sigma} = (\hat{\sigma}_x, \hat{\sigma}_y, \hat{\sigma}_z)^T$ is the total spin operator for the spin-1/2 electrons, with $\hat{\sigma}_{x,y,z}$ as the standard Pauli matrices.

The first term in equation 5 is responsible for the conductance steps observed in our spectra. When we assume zero magnetic field and no spin-polarization in the two electron reservoirs of tip and sample, the matrix elements are easily calculated to $|M_{i \rightarrow j}|^2 = 0.5$ for $i \neq j$ and $|M_{i \rightarrow i}|^2 = 0$ otherwise. This leads, at low temperature, i. e. $k_B T \ll \varepsilon_2$, when only the ground state $|\Psi_1\rangle$ is significantly occupied, to two, increasing steps in the differential conductance dI/dV with identical amplitude at the energies $\pm \varepsilon_2$ and $\pm \varepsilon_3$ (red dashed line in Figure 4c):

$$\sigma_1(eV) = \frac{1}{2} \sigma_0 \left[\Theta \left(\frac{\varepsilon_2 + eV}{k_B T} \right) + \Theta \left(\frac{\varepsilon_2 - eV}{k_B T} \right) + \Theta \left(\frac{\varepsilon_3 + eV}{k_B T} \right) + \Theta \left(\frac{\varepsilon_3 - eV}{k_B T} \right) \right], \quad (7)$$

with $\Theta(\varepsilon) = [1 + (\varepsilon - 1) \exp(\varepsilon)] [1 - \exp(\varepsilon)]^{-2}$ as the thermally broadened step function [83], and σ_0 as the total conductance in the limit of high bias.

The second term of equation 5 is due to the 2nd order Born approximation and accounts for scattering processes involving an intermediate state $|\Psi_m\rangle$. At the bias voltage where this process changes from being virtual to real, the denominator approaches zero which leads to a temperature broadened logarithmic divergence in the spectrum:

$$g(\varepsilon) = - \int_{-\infty}^{+\infty} d\varepsilon'' \int_{-\omega_0}^{+\omega_0} d\varepsilon' \frac{1 - f(\varepsilon', T)}{\varepsilon' - \varepsilon''} f'(\varepsilon'' - \varepsilon, T), \quad (8)$$

with $f(\varepsilon, T) = [1 + \exp(\varepsilon/(k_B T))]^{-1}$ as the Fermi-Dirac distribution and $f'(\varepsilon, T) = \partial f / \partial \varepsilon = (k_B T)^{-1} \times \text{sech}^2[\varepsilon/(2k_B T)]$ as its derivation [14, 40]. For the tunneling spectra the correct value of the cut-off energy ω_0 is uncritical, but is of crucial importance for the energy renormalization, as we will see in the section 2.2. The dimensionless scaling factor $-J\rho_0$ accounts for the fact that either the scattering into the intermediate or the final state is performed with electrons originating and ending in the substrate. Here, J is the coupling strength between substrate electrons and the localized spin and ρ_0 the substrate electron density at E_F .

In the case discussed here, with an effective spin $S = 1$ and all state degeneracies broken, the real parts of the matrix elements at zero field are calculated to $\Re(M_{i \rightarrow m} M_{m \rightarrow f} M_{f \rightarrow i}) = -1/4$ for the processes which go over all states and otherwise zero. Assuming again that solely the ground state is thermally populated, only the processes $1 \rightarrow 2 \rightarrow 3$ and $1 \rightarrow 3 \rightarrow 2$ can account to the tunneling transport leading to an additional conductance of:

$$\begin{aligned} \sigma_2(eV) = -\frac{1}{4} \sigma_0 J \rho_0 \left\{ [g(\varepsilon_2 + eV) + g(\varepsilon_2 - eV)] \left[\Theta \left(\frac{\varepsilon_3 + eV}{k_B T} \right) + \Theta \left(\frac{\varepsilon_3 - eV}{k_B T} \right) \right] \right. \\ \left. + [g(\varepsilon_3 + eV) + g(\varepsilon_3 - eV)] \left[\Theta \left(\frac{\varepsilon_2 + eV}{k_B T} \right) + \Theta \left(\frac{\varepsilon_2 - eV}{k_B T} \right) \right] \right\}. \end{aligned} \quad (9)$$

Interestingly, the conductance σ_2 changes in a very particular fashion the observed spectra which is the sum of σ_1 and σ_2 : Additional peak-like structures arise at the energy ε_3 due to the scattering processes via the states $1 \rightarrow 3 \rightarrow 2$ which allow us to determine $J\rho_0$ very precisely from fits of equations 7 and 9 to the spectra measured at zero field. However, the scattering processes $1 \rightarrow 2 \rightarrow 3$, which has at $B = 0$ the same weight to equation 9, does not lead to significant peaks at ε_2 due to the cut-off for electrons with a kinetic energy $|eV| < \varepsilon_3$ (Figure 4d).

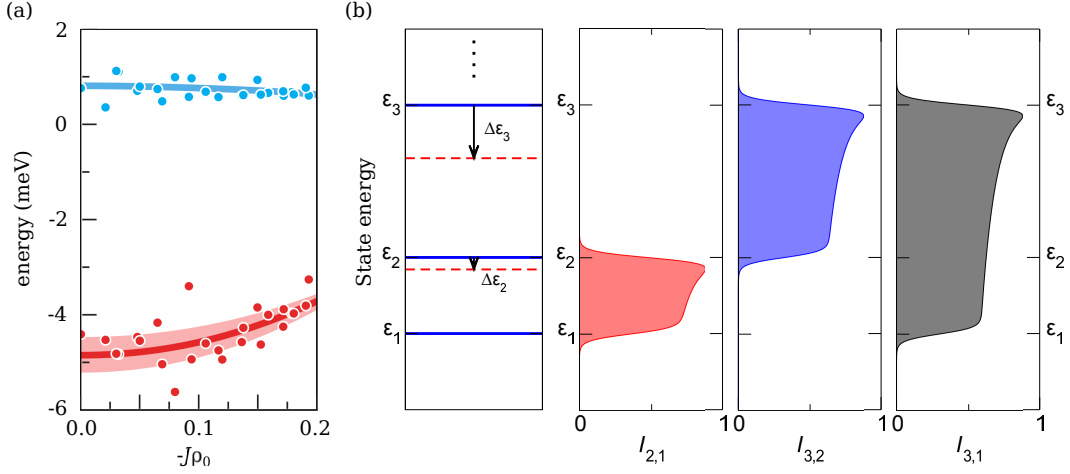


Figure 5: Magnetic anisotropy renormalization due to the coupling to the substrate. **(a)** Experimentally determined D and E (red and blue dots) parameters plotted versus the coupling strengths $-J\rho_0$. Full lines show the expected renormalization of D and E due to virtual coherences calculated with a Bloch-Redfield approach taking exchange scattering with the dissipative substrate electron bath into account. Shaded region shows the experimental uncertainty. **(b)** Principle scheme of the shift of the state energies. The integral contributions $I_{i,j}$ to the energy shift $\Delta\varepsilon_i$ are displayed in the right hand side graphs revealing that for the low lying state at the energy ε_2 only $I_{2,1}$ has weight in the equation 11, while for ε_3 the weights $I_{3,2}$ and $I_{3,1}$ have to be accounted for. Figure adapted from reference [44].

2.2. Renormalization of the eigenstate energies

As shown in figure 3c different CoH complexes on h -BN have different step energy positions which correspond to different anisotropy parameters D and E . Statistical analysis neither lead to a sharp distribution nor to a correlation with the adsorption site of the CoH on the corrugated h -BN substrate. However, by considering the values of $-J\rho_0$ from the fits to the IETS spectra, we observe a correlation between the magnetic anisotropy and the coupling with the substrate, $-J\rho_0$ [44]. The red branch in figure 5a shows that as the substrate coupling increases, the axial magnetic anisotropy decreases. For this analysis we restricted the evaluation to complexes with a clear out-of-plane anisotropy [42] determined by the criterion $\frac{|D|}{3E} > 1.5$.

To rationalize this finding, we treat the quantum mechanical system of the impurity \hat{H}_{imp} (equation 3) not as a separated system but as coupled to the dissipative bath of the substrate electrons. We then employ a Bloch-Redfield approach to account for the decay of excited states and coherences in the density matrix [84]. Interestingly, this approach leads for the off-diagonal elements of the reduced density matrix $\chi = |\Psi\rangle\langle\Psi|$ of \hat{H}_{imp} not only to a fast decoherence but additionally to an energy shift of the eigenstates due to the interaction between \hat{H}_{imp} and the reservoir. We will restrict ourselves to the Kondo-like scattering between the substrate electrons and the localized spin, as described by equation 6, up to second order leading to a correction term of the form [84, 43]:

$$\Delta\varepsilon_\alpha = (J\rho_0)^2 \sum_n \sum_{n',\alpha'} \frac{\left| \langle \varphi_{n'}, \Psi_n | \frac{1}{2} \hat{\sigma} \cdot \hat{\mathbf{S}} | \varphi_{\alpha'}, \Psi_\alpha \rangle \right|^2}{\varepsilon_\alpha - \varepsilon_n + \varepsilon_{\alpha'} - \varepsilon_{n'}}. \quad (10)$$

Knowing the scattering matrix elements and making use of equation 8 we can rewrite the energy shift as:

$$\Delta\varepsilon_\alpha = \frac{(J\rho_0)^2}{2} \sum_n \int_{-\infty}^{+\infty} d\varepsilon g(\varepsilon_\alpha - \varepsilon_n + \varepsilon) f(\varepsilon_n - \varepsilon) [1 - f(\varepsilon_\alpha - \varepsilon)]. \quad (11)$$

Figure 5b illustrates the effect of the energy renormalization. The energetically higher excited state at ε_3 is stronger affected than the low lying state at ε_2 . For the magnetic anisotropy parameters D and E of the

CoH system the shift can be approximated as:

$$D(J\rho_s) \approx D_0 (1 - \alpha(J\rho_0)^2), \quad \text{and} \quad E(J\rho_s) \approx E_0 (1 - \beta(J\rho_0)^2), \quad (12)$$

with the coefficients α and β given by the integrals of equation 11.

The solid red line in figure 5a shows the best fit when employing this model onto our data and follows the trend of equation 12. The shaded regions accounts for the possible range of α and β by considering an effective bandwidth of $\omega_0 = 0.4 - 1.2$ eV [44].

2.3. The anisotropies of Fe and Mn embedded in CuN

After the $S = 1$ CoH on *h*-BN system, we will now focus on the experimentally and theoretically intensively studied single 3*d* transition metal atoms Fe and Mn adsorbed on a monolayer of Cu₂N on Cu(100). It was on these two systems that the magnetic anisotropy of individual, single atoms was measured by IETS for the first time [78].

When Fe or Mn atoms are placed on top of a Cu site they form strong covalent bonds with the neighboring N atoms, as revealed by DFT calculations performed by Chiung-Yuan Lin and Barbara Jones and shown in figure 6a, b [78, 85]. This highly anisotropic adsorption geometry leads to three distinct symmetry axes that are perpendicular to each other: The direction out-of-plane and two in-plane directions along the Cu-N bonds and perpendicular to it, along the so called vacancy rows (Figure 7a inset).

Single Fe atoms adsorbed on this surface have been found to be in the effective $S = 2$ state with a magnetic easy-axis along the N rows (*z*-direction) and a magnetically hard-axis along the vacancy row (*x*-direction). These main anisotropy axes are directly visible in spin-resolved DFT calculations as shown in figure 6c and d. Using anisotropy values of $D = -1.55$ mV and $E = 0.31$ mV, and a gyromagnetic factor of $g = 2.11$ described the experimental data well using the spin Hamiltonian of equation 3 and a second order tunneling model [78, 79, 86]. Note that possible forth order anisotropy parameters as B_4^0 , B_4^2 , B_4^4 (see equation 1) have been found to be < 10 μ eV [87]. The Hamiltonian has as solution five non-degenerate eigenstates and, due to $D < 0$, favors, at zero field, ground states with weights at high m_z values. Similarly to the $S = 1$ system the transverse anisotropy breaks the degeneracies leading to a symmetric and antisymmetric solution with the main weights at $|\pm 2\rangle$ as ground and first excited state and weights in $|\pm 1\rangle$ for the second and third excited state (Figure 7b).

In second order, spin-flip scattering is allowed between the groundstate and the three lowest excited states but a transition to the highest state is forbidden because this would require an exchange of $\Delta m = \pm 2$. Experimental dI/dV measurements on this system show, in addition to the conductance steps, peak-like structures at the second and third step but not at the lowest one (Figure 7a). Additionally, they show an asymmetry between positive and negative bias. To rationalize these observations we can follow a similar argument as in the $S = 1$ case (see section 2.1): In third order, transitions like (121) are not possible and processes like (123) or (124) are strongly cut off due to the high energy difference between ε_2 and ε_3 or ε_4 . In contrast, the processes (132) and (142) scale with $J\rho_s$ leading to the peak features in the differential conductance. The additional asymmetry hints at a non-negligible potential scattering with matrix elements of the form

$$M_{i \rightarrow f} = \sum_{i', f'} \langle \varphi_{f'}, \Psi_f | U | \varphi_{i'}, \Psi_i \rangle = U \delta_{if}. \quad (13)$$

This *elastic* scattering term can interfere with the exchange scattering matrix elements (equation 6) leading to bias asymmetries in the spectrum (see also section 3.3) [40]. As the computed curves in figure 7a reveal, this model almost perfectly fits the magnetic field data without any adaption of the parameters. The coupling strength in these simulations is $J\rho_s = -0.087$, close to the -0.1 found in a similar perturbative approach [89]. A potential scattering term of $U = 0.35$ is necessary to reproduce the asymmetry. This value is significantly smaller than the $U \approx 0.75$ found in experiments where the magneto-resistive elastic tunneling was probed [88]. Part of this discrepancy can be understood by an additional conductance term that does not coherently interact with the spin-system and which would lead to an overestimation of U in magneto-resistive measurements. Indeed we need a constant conductance offset of about 20%, which is added to the calculated conductance to reproduce the spectra.

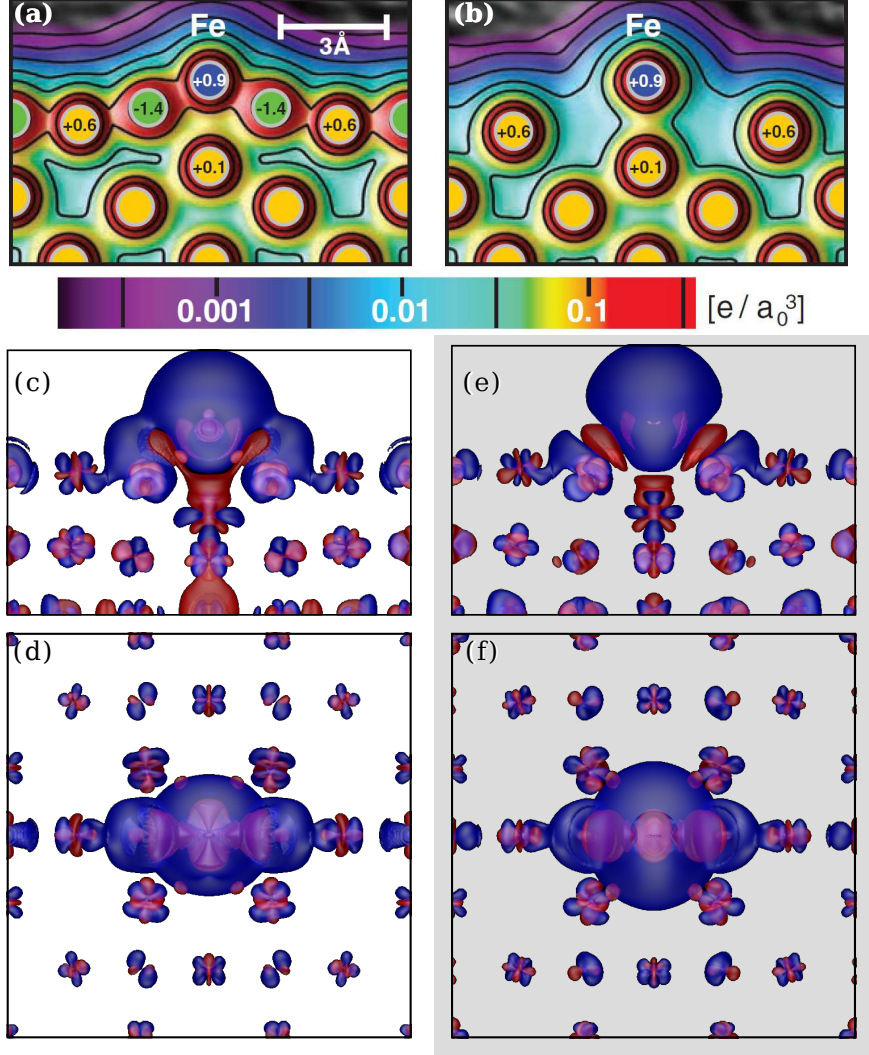


Figure 6: Adsorption of Fe and Mn on Cu₂N. **(a)** The charge density for a Cu₂N surface on Cu(100) with an Fe atom (blue) adsorbed on top of a surface Cu site along the N direction. Solid yellow and green circles label the centers of the Cu and N atoms, respectively. The numbers inside the circles indicate the net charge on selected atoms in units of e . **(b)** Same as (a) along the vacancy direction. **(c–f)** Calculated spin-density distribution for Fe (c, d) and Mn (e, f) on CuN. Contours in blue and red show the majority and minority constant spin density ($0.01e/a_0^3$) as calculated by DFT. Abscissa is along the N direction. Ordinate in panel (c, e) [(d, f)] is the out of plane [vacancy] direction. $a_0 = 52.9$ pm is the Bohr radius. Figure adapted from reference [78].

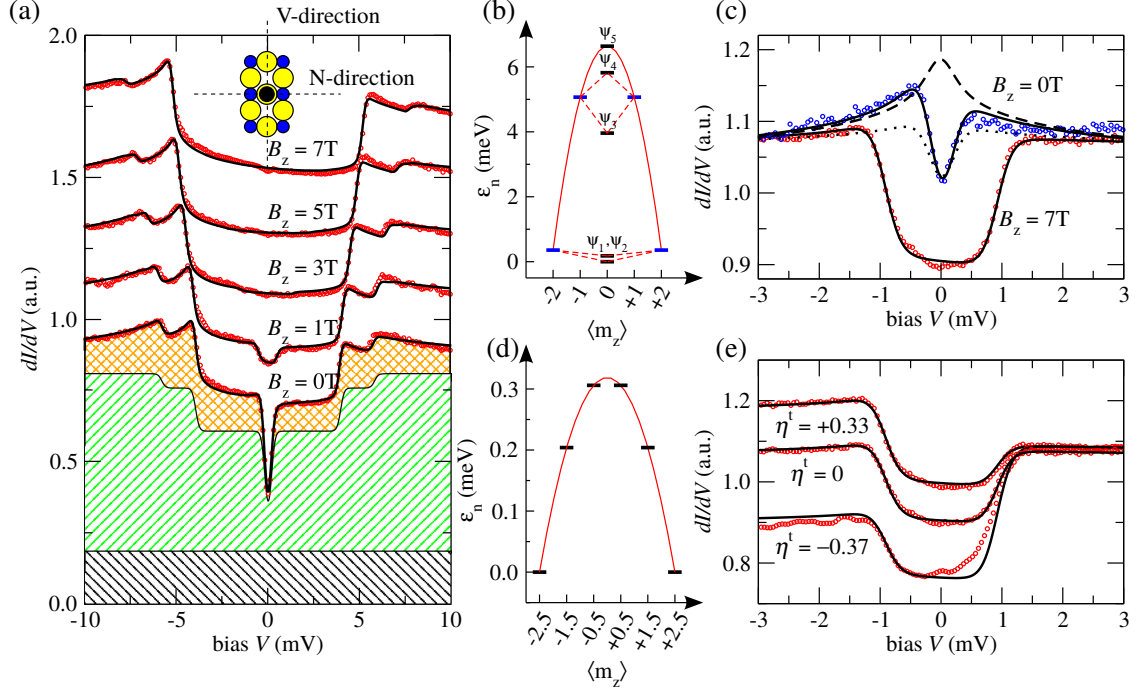


Figure 7: Comparison of experimental and calculated spectra on Fe and Mn atoms adsorbed on Cu₂N. **(a)** Experimental data measured on a single Fe atom at increasing field B_z along the easy axis (N-direction) and at a temperature of $T = 550$ mK (red circles). The simulations (black lines) for all plots are obtained with one set of parameters: $g = 2.11$, $D = -1.57$ meV, $E = 0.31$ meV, $J\rho_0 = -0.087$, $U = 0.35$, and $T_{\text{eff}} = 740$ mK. Additionally, a constant offset of $\approx 20\%$ of the total conductance has been added (black shaded area). For $B_z = 0$ the second (green shaded area) and third order (orange hatched area) contributions to the conductance are indicated. The spectra at field are vertically shifted for better visibility. The inset shows the adsorption site of the 3d atoms (black circle) on the Cu₂N (Cu yellow, N blue circle) and the two distinct surface directions. **(b)** Schematic state diagram for Fe. **(c)** Experimental data of two different Mn atoms at $B_z = 0$ and $B_z = 7$ T (colored circles). The fits (full lines) for the $B_z = 0(7)$ T data results in $J\rho_0 = -0.029(-0.0091)$, $U = 1.35(1.28)$, $D = -51(-39)$ μ eV, $g = 1.9$, and $T_{\text{eff}} = 790(930)$ mK. The dashed line shows simulated data for zero field and the absence of any anisotropy. The dotted line shows simulated data with the 7 T parameters in the absence of a magnetic field. **(d)** Schematic state diagram for Mn. **(e)** The 7 T atom as in (c) probed with tips of different spin polarizations η^t (Data from ref. [88]). Figure adapted from reference [40].

Switching from an integer to a half-integer spin system we now discuss individual Mn atoms on Cu_2N , which have a spin of $S = 5/2$ and only a small easy-axis anisotropy of $D \approx -40 \mu\text{eV}$ along the out-of-plane direction and a negligible transverse anisotropy [90, 78]. Also here spin-resolved DFT can visualize the main anisotropy axis (Figure 6e, f). The easy-axis anisotropy prohibits the immediate formation of a Kondo state due to a Kramer's degenerate ground state doublet with $m_z = \pm 5/2$, which would require a $\Delta m = 5$ to flip (Figure 7c). At zero field a typical spectrum shows only one step, which belongs to the transition between the $\pm 5/2$ and the $\pm 3/2$ states that have superimposed asymmetric peak structures (Figure 7d). The fit to the model yields $J\rho_s = -0.029$ and resembles a $S = 1/2$ split-Kondo peak at small magnetic fields (see next section, figure 9e). A different Mn atom investigated at $B_z = 7 \text{ T}$ shows a significantly reduced $J\rho_s = -0.0091$. Interestingly, we find for both atoms a potential scattering value of $U \approx \frac{1}{2}S$, which allows one to describe the spectra without the need of any additional conductance offset. This high U value that is the origin of the bias asymmetry has been independently found in spin-pumping experiments [91] and by measuring the magneto-resistive elastic tunneling contribution [88]. The extraordinary agreement between model and experiment can be seen in measurements using different spin-polarized tips on the same atom (Figure 7e). Here, the strong influence of the tip-polarization on the inelastic conductance at bias voltages $|V| < 1 \text{ mV}$ is evident while the differential conductance at $V > 1.5 \text{ mV}$ stays constant for all tips.

3. The Kondo effect

The electrical resistance of pure metals usually decreases when they are cooled down because one of the main origin of the resistivity, the scattering of electrons on lattice vibrations, is frozen out at reduced temperature. However, already in the 1930s it was discovered that in some metals containing diluted magnetic impurities the electrical resistance increases again below a certain temperature [92, 93].

The origin of this effect remained obscure for a long time but was explained in 1964 by Jun Kondo [46, 94]. He showed that these experimental observations can be understood within a scattering model, which explicitly takes into account the interaction of the spins of the conduction electrons of the host metal with the localized spin of the magnetic impurities. This interaction is usually considered to be antiferromagnetic (AFM), i.e. the spin-spin exchange coupling J is negative, and creates correlations between the localized magnetic moment and the surrounding host electrons. This leads to a screening of the impurity magnetic moment and to the formation of a new, non-magnetic, many-electron singlet ground-state below a critical temperature T_K [47] (Figure 8).

Interestingly, this so-called 'Kondo effect' emerges in quite a broad range of different physical contexts, such as the zero-bias anomalies observed in quantum dots and nanowires [97, 98, 99, 100, 101, 102, 103], or the dynamical behavior close to a Mott transition [104, 105]. The simplicity of the underlying model Hamiltonian (equation 6) contrasts the complex physics and the non-trivial solutions that occurs in the strong coupling regime. The origin of this Kondo problem lies in the appearance of logarithmic divergences which make perturbative models fail for $T \rightarrow 0$. Only the development of a completely new theoretical understanding clarified the nature of the many-electron ground state which manifest itself in a strong resonance close to the Fermi-energy [95, 106, 107].

The existence of the Kondo resonance in dense Kondo systems like solid surfaces or thin films of γ - and α -cerium as well as in Ce-heavy-fermion compounds has been experimentally confirmed by high-resolution photoemission electron spectroscopy (PES) [108, 109, 110, 111, 112, 113] and by inverse photoemission [114, 115]. While these measurements always probe an ensemble of impurities due to the limited spatial resolution in PES, STM opened the unique opportunity to detect the Kondo effect in the smallest conceivable Kondo system: a single magnetic impurity supported on top of a nonmagnetic metal [32, 38, 116, 117, 118, 119, 120, 121, 122].

While most of these experiments were performed at $T \ll T_K$ much less attention has been paid to the weak coupling regime, which is relevant either at elevated temperatures ($T \gg T_K$) or for ferromagnetic (FM) interactions ($J > 0$). In the case of FM interaction, the impurity spin is always weakly coupled and becomes asymptotically free in the limit of low temperature [95, 123]. A possible path for creation of such a state will be discussed in section 4. For AFM interactions at high temperatures, thermal fluctuations destroy the singlet state enabling the physics to be described by perturbation theory [95].

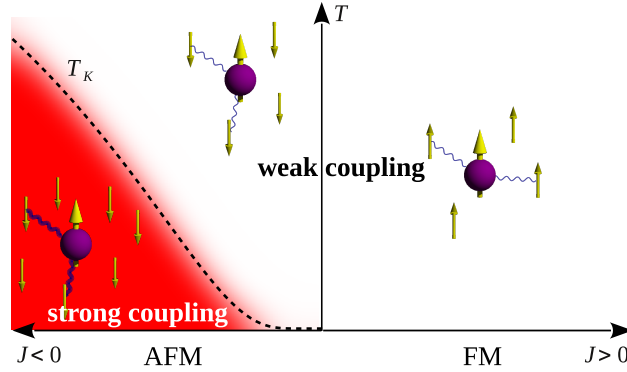


Figure 8: The different regimes of the Kondo effect. The Kondo interaction $J\hat{\mathbf{S}} \cdot \hat{\boldsymbol{\sigma}}$ couples itinerant electrons of the host to a magnetic impurity. For exchange interaction $J < 0$, the antiferromagnetic (AFM) coupling leads to an entangled many-body state, where the antiparallel alignment of the spins of the conduction electrons effectively screens the impurity spin. The ground state at temperatures T below the characteristic Kondo temperature T_K is a singlet with total spin $S = 0$ (red area), well protected from higher energy states. In contrast, for $J > 0$, the ferromagnetic (FM) coupling tends to create a screening cloud of spins aligned parallel to the impurity spin, which becomes asymptotically free at low temperatures [95, 96]. For FM coupling or at temperatures $T \gg T_K$, the system is in the weak coupling regime, which can be treated perturbatively. Figure adapted from reference [48].

In this section we will start our discussion with the results obtained on a fully organic radical molecule which was the first detailed study of the Kondo effect in the weak coupling limit [48]. From thereon, we will briefly summarize the externally controllable conditions, like temperature and magnetic field, that causes the perturbative approach to breakdown [40]. Therefore, individual Co atoms on Cu_2N , with their high effective spin $S = 3/2$ will link the Kondo physics with the magnetic anisotropy discussed in section 2 [50, 43]. Additionally, this system is particularly interesting because it was the one used to determine the spin polarization of the field split Kondo state [51].

3.1. The weak coupling limit in an organic radical

In this study we used a purely organic molecule, which has a radical nitronyl-nitroxide side group [124], adsorbed on a clean Au(111) surface as sketched in figure 9a. Molecular crystals containing the same radical side group showed ferromagnetic coupling below a Curie temperature of 0.6 K [125]. In this molecule the unpaired electron is spatially delocalized over the O–N–C–N–O part of the side group instead of being localized on a specific atom (Figure 9b). This delocalization stabilizes the unpaired electron against chemical reaction and charge transfer, which would lead to a spin zero system. Constant-current STM images show the elongated molecular backbone and the radical side group, which is imaged as a ≈ 0.3 nm high and 1.0 nm wide protrusion (Figure 9c).

Figure 9d shows the differential conductance measured at zero-field on the side-group of the molecule revealing a strongly temperature dependent peak at zero bias. Field dependent measurements at low temperature ($T = 1.8$ K) show that this peak is split into two peaks as soon as the Zeeman-energy $g\mu_B B$, with $g \approx 2$ for a free $S = 1/2$ spin, is comparable to $k_B T$ (see figure 9e). At higher fields ($B \gtrsim 10$ T) the spectra show a clear steplike structure symmetrically around zero bias and additional peak-like conductance increases at the step-positions.

To describe the excitation processes during tunneling we use a model based on the perturbative approach established by Appelbaum, Anderson, and Kondo [46, 80, 81, 82] in which spin-flip scattering processes up to 3rd order in the spin-spin exchange coupling J are accounted for (Figure 9a). This model is equivalent to the one discussed in section 2.1 and leads to a tunneling conductance $\sigma(eV) = dI/dV(V)$ due to the

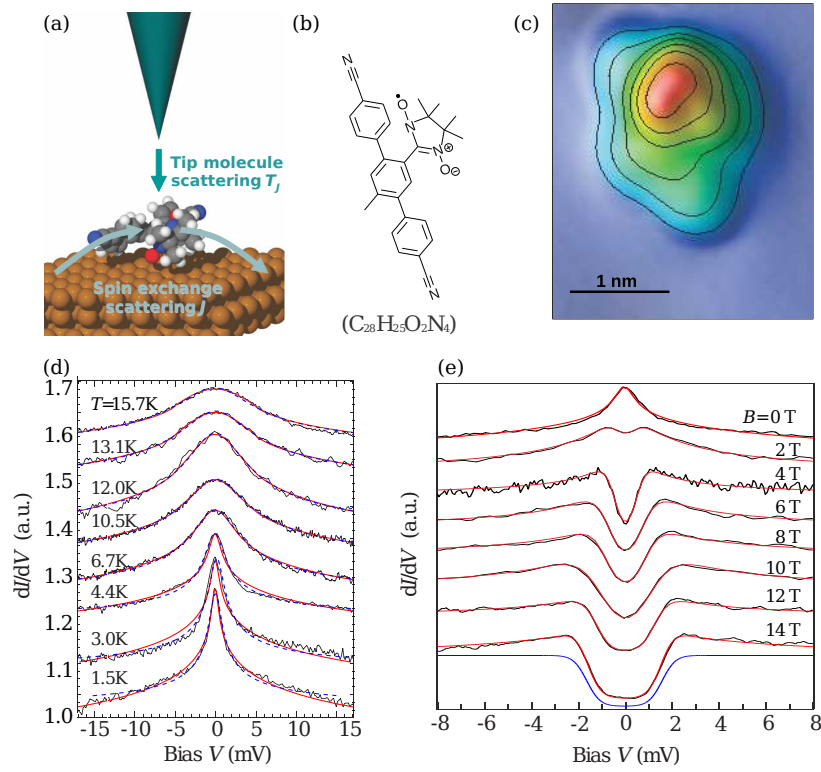


Figure 9: The weak coupling Kondo effect in an organic radical molecule. **(a)** Principle scheme of the experiment. **(b)** Chemical structure of the studied organic radical molecule ($C_{28}H_{25}O_2N_4$) with a nitronyl-nitroxide side group that contains a delocalized singly occupied molecular orbital. The molecule is drawn with a similar orientation as in the topography in **(c)**. **(c)** Topography of one organic radical molecule ($V = 100$ mV, $I = 33$ pA). Contour lines are at height intervals of 50 pm. **(d)** Typical dI/dV spectra taken on the radical side group of the molecule (black) and simulated spectra using the perturbation model (red). **(e)** Spectra taken at successively increased magnetic fields at $T = 1.8$ K. Blue line at 14 T shows simulation in 2nd order only. All spectra in **(d)** and **(e)** are normalized and offset for visual clarity. Figure adapted from reference [48].

electron-spin interaction with the following contributions:

$$\sigma_1(eV) = \frac{e^2}{h} T_J^2 \left(1 + 2 \sum_{\substack{i,f \\ i \neq f}} \varrho_i(T) \left[\Theta \left(\frac{\Delta_{if} + eV}{k_B T} \right) + \Theta \left(\frac{\Delta_{if} - eV}{k_B T} \right) \right] \right) \quad (14)$$

$$\begin{aligned} \sigma_2(eV) = \frac{e^2}{h} T_J^2 J \rho_0 \sum_{\substack{i,f \\ i \neq f}} \varrho_i(T) & \left\{ \left[\Theta \left(\frac{\Delta_{if} + eV}{k_B T} \right) + \Theta \left(\frac{\Delta_{if} - eV}{k_B T} \right) \right] \times \right. \\ & \left[\underbrace{2 \times g(eV)}_{112 \text{ and } 112R} + \underbrace{g(\Delta_{if} + eV) + g(\Delta_{if} - eV)}_{122 \text{ and } 122R} \right] \\ & \left. + \underbrace{g(\Delta_{if} + eV) + g(\Delta_{if} - eV)}_{121 \text{ and } 121R} \right\} \end{aligned} \quad (15)$$

Here, T_J is the coupling constant determining the overall conductance of the tunnel junction, $\varrho_i(T) = Z^{-1} \times \exp[-\varepsilon_i/(k_B T)]$, with $Z = \sum_i \exp[-\varepsilon_i/(k_B T)]$, is the thermal occupation of the localized spin in the state $|\Psi_i\rangle$, $\Theta(\varepsilon)$ is the thermally broadened step function (see page 8) [83], $\Delta_{if} = \varepsilon_f - \varepsilon_i = \pm g\mu_B B$ is the energy difference (Zeeman energy) between the two spin states of the molecule, and $g(\varepsilon)$ is the function originating from the divergence of the second term in equation 5 as defined in equation 8.

At zero field the conductance simplifies to $\sigma(eV) = \sigma_0 - \alpha \times g(eV/(k_B T))$, a temperature broadened logarithmic function, with the temperature T as the only relevant fit parameter. At $B \neq 0$ the step-like structure is governed by ordinary inelastic spin-flip scattering of σ_1 in equation 14 as illustrated in figure 10a [50, 88, 40]. The additional logarithmic peaks in the conductance result from the different possible higher order scattering paths described by σ_2 and labeled as Feynman diagrams illustrated in figure 10b. We see that there are in total 6 processes of order three per initial state which have to be accounted for and which are reflected in the terms of σ_2 in equation 15.

The model fits exceptionally well with our data (see red lines in figure 9d, e) using a coupling to the substrate electrons of $J\rho_0 = -0.04 \pm 0.01$. Different as for the case of the spin $S = 1$ system discussed in section 2.2, in this half-integer Kondo system energy renormalization occurs already in first order of the coupling strength $J\rho_0$ leading to an effective gyromagnetic factor of $g_{\text{eff}} = g_0(1 + J\rho_0)$ [126]. For the highest fields $B \geq 10$ T this is in good agreement with an experimentally observed $g_{\text{eff}} = 1.93 \pm 0.02$ [48]. Note, however that this perturbative approach only holds as long as higher order contributions can be neglected, that is, as outlined in the next section, as long as the temperature is high compared to the Kondo temperature T_K of the system.

3.2. The limit of the perturbative approach

When a half-integer spin with $S > 1/2$ has easy-plane anisotropy $D > 0$, its ground state at zero field is a doublet with its main weights in $m_z = \pm 1/2$. This enables an effective scattering with the substrate electrons and leads, at low enough temperatures, to the formation of a Kondo state. Experimentally, this has been observed for bare Co on h -BN/Rh(111) [44] and for Co atoms on Cu_2N [51, 50, 127, 43, 128, 129, 130]. Both systems can be described as effective $S = 3/2$ whereby the latter enters the correlated Kondo state with a characteristic Kondo temperature of $T_K = 2.6$ K in experiments performed on small patches of Cu_2N at temperatures down to $T = 550$ mK [50]. Apart from $D > 0$, Co on Cu_2N also has a small in-plane anisotropy ($E \neq 0$) which creates an easy axis (x) along the nitrogen row and a hard axis (z) along the vacancy rows (Figure 11a).

Interestingly, in this system the coupling to the substrate $J\rho_0$ changes with the position of the Co atom on larger Cu_2N patches, concomitant with a change in the anisotropy energies which separates the $|\pm 1/2\rangle$

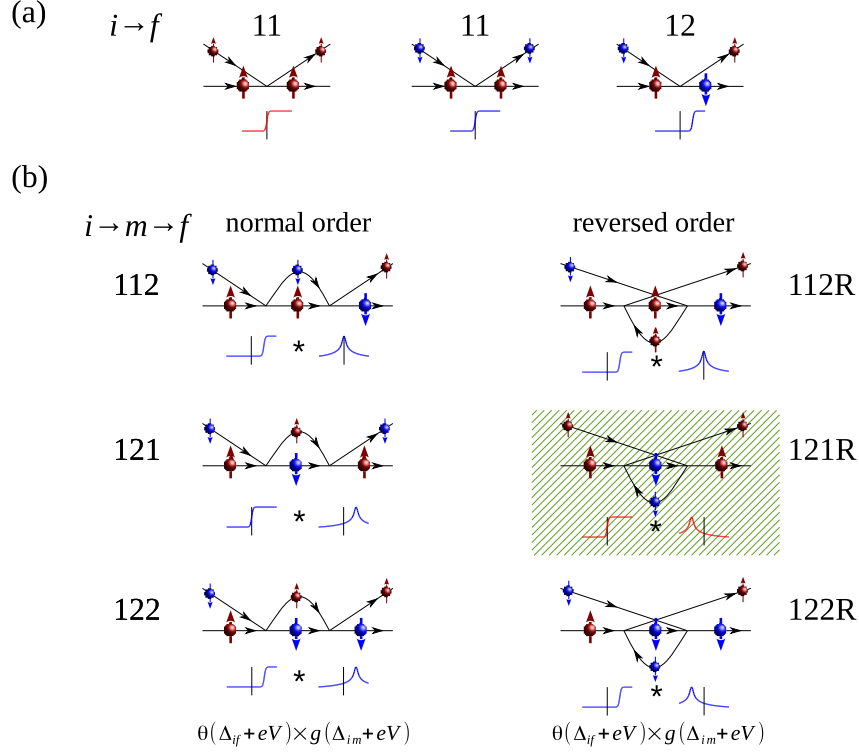


Figure 10: Interaction diagrams of order two (a) and three (b) for an electron tunneling from tip to sample into a two level $S = 1/2$ spin system. The large spheres depict the state of the localized spin and the small spheres the state of the interaction electron. Schematic spectra show their contributions to the conductance at positive bias. The numbers label the processes with the state order of the localized spin-system. An appended 'R' label processes in which the scattering into the intermediate state is performed *before* the tunneling electron interacts (exchange diagrams). Note that the time order of the processes strongly influences the conductance spectra as schematically displayed in the small graphs (vertical line is E_F ; the * means multiplication). Figure adapted from reference [40].

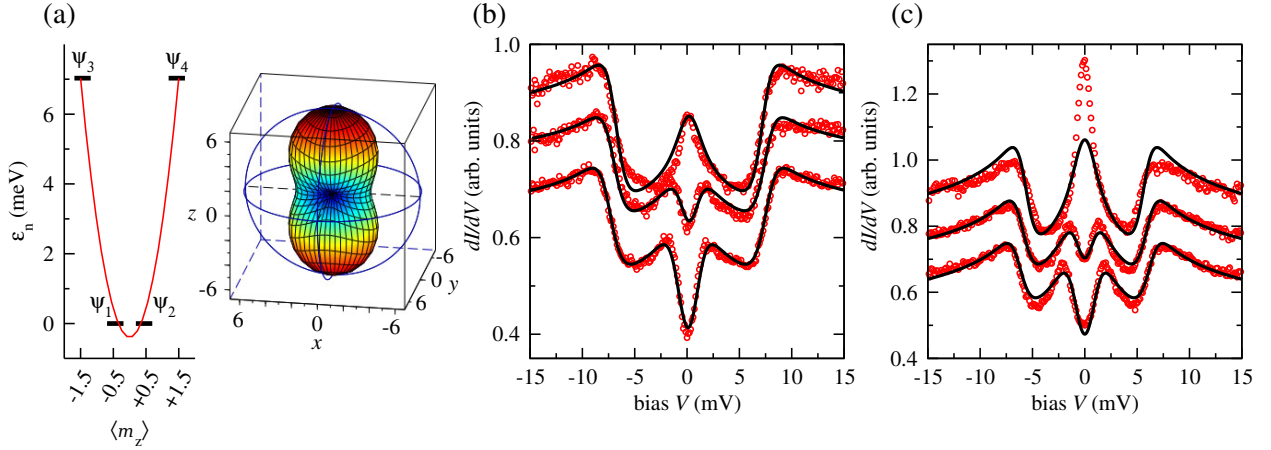


Figure 11: The tunneling spectra of Co atoms ($S = 3/2$) on Cu_2N . (a) Schematic state diagram and visualizations of the magnetic anisotropy (in meV). At $B = 0$ the states $|\psi_1\rangle$ and $|\psi_2\rangle$ are degenerated and differ by $\Delta m_z = \pm 1$. (b) and (c) Experimental data from reference [43] of two different Co atoms at $B_x = 0, 4, 6$ T (colored circles, top to bottom, shifted for clarity). The best fits (full lines) results in $T_{\text{eff}} = 4$ K, $D = 3.3$ meV, $E = 0.7$ meV, $g = 2$, $J\rho_0 = -0.11$ for (b) and $T_{\text{eff}} = 3.8$ K, $D = 2.7$ meV, $E = 0.5$ meV, $g = 2$, $J\rho_0 = -0.25$ for (c). Figure adapted from reference [40].

states from the $|\pm 3/2\rangle$ states [43, 67]. This effect can be rationalized by virtual coherences as discussed in section 2.2. For us this allows the study of the transition from the weak coupling to the strong coupling regime. In the case where the Co atom is relatively weakly coupled to the substrate ($J\rho_0 \approx -0.1$) the experimental data can be consistently fitted to the 3rd order perturbation model even at different field strengths along B_x (Figure 11b) [40]. We observe a zero-energy peak that splits at applied fields similar to the $S = 1/2$ radical molecule shown in figure 9e. But while for $S = 1/2$ the field direction does not play a role, here the peak splitting depends strongly on the direction due to the magnetic anisotropy [50]. For this high-spin system we furthermore observe inelastic steps due to the transition to energetically higher excited states which are located at $|eV| = 2|D|$ for $B = 0$ and whose additional peak structure is well described within the scattering model [40].

For Co atoms adsorbed closer to the edges of the Cu_2N patches, the coupling to the substrate increases and the fit to the model worsens significantly (Figure 11c). While the experimental data measured for non-zero fields are reasonably well described with $J\rho_0 \approx -0.25$, at $B = 0$ the experimentally detected peak at E_F is stronger than the peak created by the model. Additionally, the experimental peak-width appears to be smaller than the temperature broadened logarithmic function. Furthermore, we observe that the calculated spectrum no longer accurately describes the steps at $2|D|$. At this energy the third order contributions are less pronounced in the experimental data, indicating that we reach the limit of the perturbative approach.

The full description of a spin system in the strong coupling regime requires complex theoretical methods like numerical renormalization group theory [106, 47, 131] which are beyond the scope addressed here. Nevertheless, we can discuss some of the physical consequences within the perturbative model. In contrast to the examples discussed in section 2, the two lowest degenerate ground states of the Co/ Cu_2N system, as well as any $S = 1/2$ system, have weights in states that are separated by $\Delta m = \pm 1$. Thus, at zero field, electrons from the substrate can efficiently flip between these two states. The computation of the transition rate between the two degenerate states $|\Psi_i\rangle$ and $|\Psi_f\rangle$ of the spin system up to second order only is directly proportional to the temperature (Figure 12a) [40]:

$$\Gamma_{12}^{(2)s \rightarrow s} = \frac{2\pi}{\hbar} (J\rho_s)^2 |M_{12}|^2 k_B T, \quad (16)$$

with the scattering matrix M_{12} as defined in equation 6.

These scattering processes tend to change the spin polarization of the electronic states in the sample *near the adsorbate* to be correlated with the localized spin. Nevertheless, this local correlation will be quickly destroyed by decoherent scattering processes with the remaining electron bath, which we can assume to be large and dissipative. This decoherence rate is also proportional to the temperature, $\Gamma_{\text{decoh}} \propto k_B T$ [132], but usually stronger so that no highly correlated state can form. This picture changes when we additionally consider third order scattering processes which yield the probability [40]:

$$\begin{aligned} \Gamma_{if}^{(3)s \rightarrow s} &= \frac{4\pi}{\hbar} (J\rho_s)^3 \int_{-\infty}^{\infty} d\varepsilon \sum_m \Re(M_{fi} M_{mf} M_{im}) \\ &\times [g(\varepsilon_{mi} - \varepsilon, T) + g(\varepsilon_{im} - \varepsilon, T)] f(\varepsilon, T) [1 - f(\varepsilon - \varepsilon_{if}, T)]. \end{aligned} \quad (17)$$

Due to the growing intensity of $g(\varepsilon = 0)$ at reduced temperatures, for temperatures $T \rightarrow 0$, the scattering $\Gamma^{(3)}$ decreases significantly more slowly than $\Gamma^{(2)}$ (see figure 12b) so that their ratio steadily increases (see figure 12c):

$$\frac{\Gamma^{(3)}}{\Gamma^{(2)}} \approx J\rho_s \ln \left(\frac{k_B T}{\omega_0} \right). \quad (18)$$

In contrast, the decoherent scattering rate with the bath Γ_{decoh} lacks localized scattering centers and therefore has no significant third order contributions. Equation 18 leads to a characteristic temperature, the Kondo temperature (T_K), where $\Gamma^{(3)}$ and higher order scattering terms become the dominant processes and perturbation theory breaks down [46, 133, 134, 47]:

$$T_K \approx \frac{\omega_0}{k_B} \exp \left(\frac{1}{J\rho_s} \right). \quad (19)$$

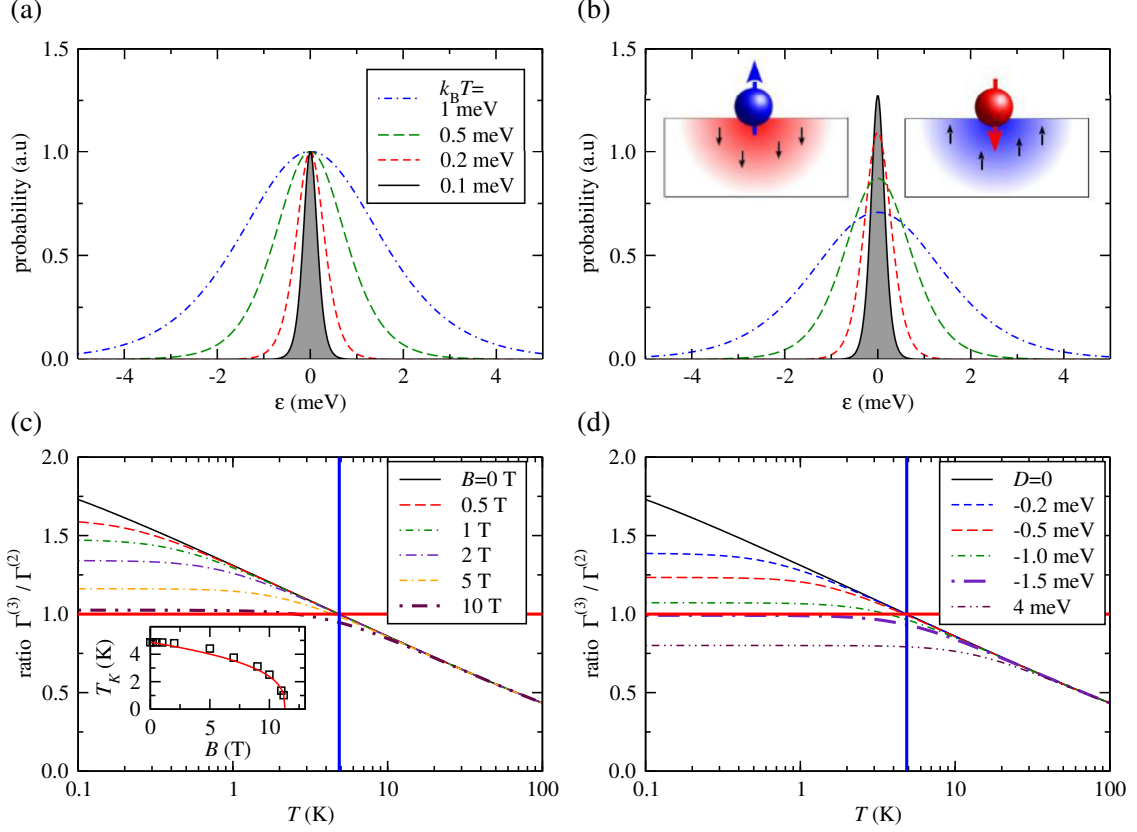


Figure 12: Correlations induced by substrate electrons. **(a)** In second order the scattering probability of a substrate electron with energy ε is given by the overlap of the electron and hole-like Fermi-Dirac distributions (area underneath the curve) and is for degenerate ground states directly proportional to the temperature. Third order scattering **(b)** gets logarithmically stronger than the second order processes with decreasing temperature. The graphical inset illustrate the entangled state at temperatures below the characteristic Kondo temperature. **(c)** Ratio of the 2nd and 3rd order contributions when an additional external field is applied ($S = 1/2$, $g = 2$, $J\rho_0 = -0.1$, $\omega_0 = 100$ meV). The inset show T_K as defined by $\Gamma^{(2)}/\Gamma^{(3)} = 1$ for different fields B . **(d)** Same as (c) but for a $S = 1$ system with varying magnetic anisotropies D and $E = 0.2D$. At $D \approx -1.5$ meV, the strong correlation regime cannot be reached even at $T \rightarrow 0$. Figure adapted from reference [40].

Below this temperature the assumption used up to now, i.e. that the electronic states in the sample are not influenced by the presence of the spin system, no longer applies. Using exact methods like the modified Bethe ansatz [107, 135] or numerical renormalization group theory [131] reveals that the sample electrons in the vicinity rather form an entangled state with the impurity, i.e.

$$\Psi^{\text{total}} = \frac{1}{\sqrt{2}} \left(\left| \downarrow^s \right\rangle \left| +\frac{1}{2} \right\rangle - \left| \uparrow^s \right\rangle \left| -\frac{1}{2} \right\rangle \right), \quad (20)$$

as illustrated in the inset of figure 12b. This combined state is quite complicated because the electronic states in the sample are continuous in energy and extend spatially, and therefore strongly alter the excitation spectrum of the adsorbate [136, 137].

An externally applied magnetic field will counteract the formation of the singlet Kondo state. However, while the precise calculation at finite temperature and field is rather difficult, we can use our definition of T_K , which is the break-down of the perturbative approach, to estimate the behavior at applied field. Figure 12c shows the result for a prototypical $S = 1/2$ system. We see that the increasing field reduces the Kondo temperature T_K and that at $B \geq B_C$ the 3rd order scattering rate $\Gamma^{(3)}$ will not exceed the 2nd order scattering rate $\Gamma^{(2)}$ even at $T \rightarrow 0$. In this example the ratio $g\mu_B B_C/k_B T_K \approx 3$ differs from the usually cited ratio of ≈ 0.5 at which the splitting of the Kondo state can be observed [136]. Note also, that this approach has neglected the renormalization of the gyromagnetic factor due to the coupling with the substrate (see page 16) [126]. The relationship between the Kondo temperature and the critical field can be described with a simple equation,

$$\frac{B_C(T)}{B_C(T=0)} = 1 - \left(\frac{T}{T_K(B=0)} \right)^\alpha, \quad (21)$$

with the exponent $\alpha \approx 3$ (see inset figure 12c). Note, that equation 21 is formally identical to the relation between the critical magnetic field and the transition temperature in classical, BCS-like, superconductors [138].

We can use the same approach to determine under which conditions a non-degenerated high-spin system might enter the strongly correlated Kondo state. As an example we will use a spin $S = 1$ system, similar to the one discussed in section 2.1. While we have already seen that *virtual* coherences lead to an energy renormalization (see section 2.2), we now ask about the interplay between magnetic anisotropy and the high-spin Kondo screening phase. Figure 12d shows the result, which behaves similarly to the $S = 1/2$ system in an external magnetic field. The introduction of an easy axis anisotropy reduces T_K , eventually prohibiting the formation of the highly correlated state Kondo state even at zero temperature. In the example here, that uses parameters close to the ones discussed for CoH on *h*-BN, the critical anisotropy is $D \approx -1.5$ meV. Thus, the evaluation of the $S = 1$ system with $D \leq -3$ meV (see figure 5a) in terms of a purely perturbative model is appropriate.

3.3. The strong coupling regime

At temperatures $T \ll T_K$ the zero bias anomaly peak at the Fermi energy can no longer be well reproduced by a temperature broadened logarithmic function which in any case must diverge for $T \rightarrow 0$. While the quantum system enters the Fermi liquid regime [139], the zero-bias peak remains at finite width and amplitude. Such a bias dependent peak is much better described by either a Lorentzian function or the so-called Frota function [140, 141, 142] which has additional weight at elevated biases to account for the logarithmic tails:

$$g_{\text{Frota}}(\varepsilon) = \Re \left(\sqrt{\frac{i\Gamma_F}{i\Gamma_F + \varepsilon}} \right). \quad (22)$$

This peak reveals itself as an apparent increase of the local density of states or, more precisely, as a weight increase of the spectral function of the many particle system in tunneling experiments. If an additional coherent tunneling channel exists, then interferences can change the differential conductance significantly, leading to strongly asymmetric peaks or even dips in the spectrum [37]. This behavior is quite

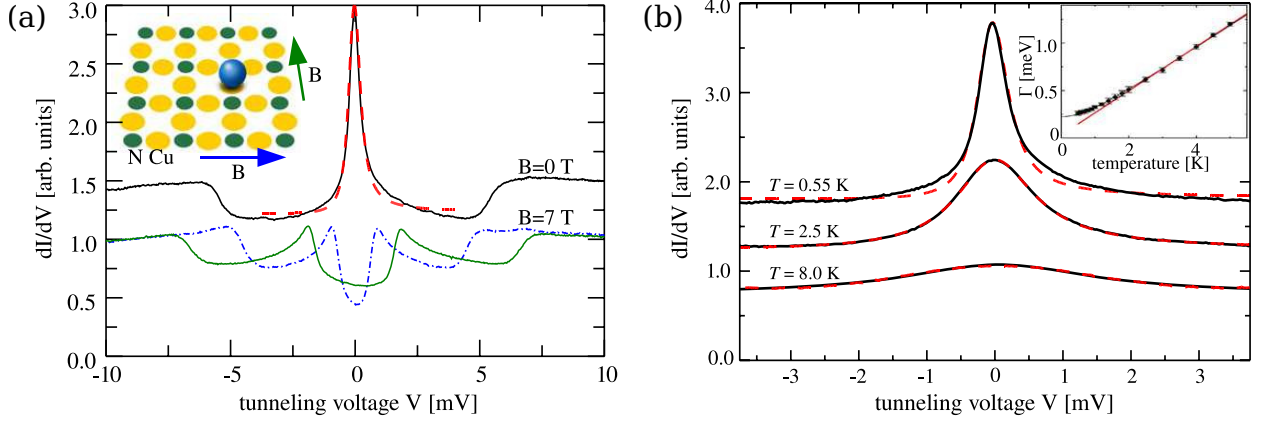


Figure 13: **(a)** Spectra of a Co atom on $\text{Cu}_2\text{N}/\text{Cu}(100)$ measured at a temperature of $T = 0.5$ K and an external magnetic field of $B = 0$ and 7 T. The zero-field spectrum reveals a Kondo peak which is fitted to a temperature-broadened Fano function (red dashed line) and IETS steps at $V \approx \pm 6$ mV due to spin-flip transitions [50]. At $B = 7$ T, the spin-flip step positions have moved and the Kondo peak has split. This splitting depends strongly on the direction of the magnetic field. **(b)** The central Kondo peak measured at different sample temperatures (black lines) and fitted with a temperature-broadened Fano function (red dashed lines) Inset: intrinsic half-width Γ extracted from the fits. The red line shows the linear behavior of Γ at high temperature and has a slope of $(5.4 \pm 0.1)k_B$. The black line is a fit to equation 25. Figure adapted from reference [37].

easy to understand; let us assume that the bare Kondo peak can be well described by a Lorentzian which has the transfer function $t_1 = (1 + i\varepsilon)^{-1}$, with $\varepsilon = (E - E_0)/\Gamma$ as the normalized energy. Additionally, we will assume an energy independent constant direct tunneling channel which we describe without any restrictions as $t_0 = -(1 - iq)^{-1}$.

Tunneling experiments detect the absolute square of the sum of all possible transfer channels. Using the above defined t_0 and t_1 results in the well known Fano equation [143]

$$g_{\text{Fano}}(\varepsilon) = |t_0 + t_1|^2 = \left| -\frac{1}{1 - iq} + \frac{1}{1 + i\varepsilon} \right|^2 = \frac{1}{1 + q^2} \frac{(q + \varepsilon)^2}{1 + \varepsilon^2}, \quad (23)$$

in which q determines the asymmetry. Equivalently, equation 22 can be generalized [144] leading to an asymmetric Frota function as:

$$g_{\text{Frota}}(\varepsilon, q) = \frac{q^2 - 1}{q^2 + 1} \Re \left(\sqrt{\frac{i\Gamma_F}{i\Gamma_F + \varepsilon}} \right) + \frac{2q}{q^2 + 1} \Im \left(\sqrt{\frac{i\Gamma_F}{i\Gamma_F + \varepsilon}} \right). \quad (24)$$

For bare metal adatoms on metal surfaces, typically $q \approx 0$ has been found [118, 119], in which case $g(\varepsilon)$ becomes a dip. For $q \approx 1$, the line shape becomes strongly asymmetric, and for $q \rightarrow \infty$, the peak is recovered.

At $T \ll T_K$ the half-width Γ of the Lorentzian (or the effective half-width of the Frota function $\Gamma \approx 2.54\Gamma_F$ [140]) is directly related to the Kondo temperature and the correlation energy of the Kondo state: $k_B T_K = \Gamma$. This zero-temperature result can be expanded in the Fermi-liquid framework to elevated temperatures using corrections in first leading order [116]:

$$\Gamma(T) = \sqrt{(k_B T_K)^2 + \alpha(k_B T)^2}. \quad (25)$$

Here, one expects theoretically $\alpha = 2\pi$, close to the experimentally observed $\alpha = 4.5$ in quantum dots [145], $\alpha \approx 5$ for individual Ti atoms on Cu(100) [116], and $\alpha = 5.4 \pm 0.1$ in low temperature measurements on (relatively) strongly coupled Co atoms on small patches of Cu_2N [50].

The latter system is of particular interest because here the many-body Kondo effect and the magnetic anisotropy, usually described within a single-particle approximation, are of similar strength. Figure 13a shows such spectra measured at $T = 0.5$ K at zero magnetic field B and at $B = 7$ T [50]. The spectra

can be well described with an asymmetric Lorentzian and additional conductance steps at voltages that enable scattering of the spin system. Surprisingly, these steps are well described using only a second order perturbation spin-flip model and do not show any third order logarithmic contributions. This means that the probability of the third order scattering channels must be closed due to the ground-state correlation between the localized spin and the substrate electrons.

Under an applied magnetic field, the peak splits and the spin-flip excitation step positions shift in energy. Interestingly, the single-particle magnetic anisotropy Hamiltonian of equation 3 not only describes the energy shift of the inelastic conductance steps accurately, but also the positions of the split Kondo peak. The peak width at zero-field corresponds to a Kondo temperature of $T_K = 2.3 \pm 0.3$ K and the broadening of the peak at elevated temperatures follows equation 25 as expected from Fermi liquid theory [139, 116] and as shown in the inset of figure 13b. Note, that at even higher temperatures, where $T \gg T_K$, we reach again the weak-coupling limit and the spectrum is better described with the perturbative model and temperature broadened logarithmic divergences as shown in figure 11. Due to the limitations of equation 25, which is only valid at $T \lesssim T_K$, fitting temperature dependent experimental data in the weak coupling limit with Lorentzian or Frota functions can lead to unphysically high α values [48]. In such cases, T_K is presumably much smaller than the experimentally accessed temperatures.

3.4. Spin polarization of the split Kondo peak

As we have seen in the last section, when external magnetic fields which exceed the Kondo correlation energy, i.e. $g_{\text{eff}}\mu_B B > k_B T_K$, are applied to a strongly coupled Kondo system the zero-bias resonance splits into two distinct parts (Figure 13a) [50]. However, while this has been observed also for other systems [146, 62], the spin-resolved properties of such a split Kondo state and, in particular, the amount of spin polarization of the two resulting peaks remains elusive [147, 148]. While there is one early spin-resolved measurement of a split Kondo state [149], the asymmetry of the peaks was not studied systematically and a comprehensive picture was only found recently using individual Co adatoms on Cu_2N as a test system [51].

In this experiment a spin-polarized tip was prepared by picking up Mn atoms from the Cu_2N surface with a conventional STM tip [91]. Since the measured asymmetry in the spectrum is the product of sample and tip spin polarization, $\eta^{\text{eff}} = \eta_{\text{sample}} \times \eta_{\text{tip}}$, it is crucial to characterize the degree of spin polarization of the tip. This was done by spin-resolved measurements of individual Mn atoms on the same surface. As discussed in section 2.3 and displayed in figure 7c and 7e, Mn atoms on Cu_2N show one spin-flip excitation at about 1 mV. When measured with a spin-polarized tip, the heights of the inelastic steps at positive and negative voltage (h^+ and h^-) differ [91, 150]. The asymmetry of the step heights $\eta^{\text{eff}} = (h^- - h^+)/ (h^- + h^+)$ can now be measured as a function of the external magnetic field. Because of the small magnetocrystalline anisotropy of Mn the nominal spin polarization of the step is $\eta_{\text{Mn}} = 1$ and therefore the experimental η^{eff} is a quantitative measure of the tip spin polarization η_{tip} . The magnetic-field dependence of the tip's spin polarization was found to be consistent with a paramagnetic behavior of the Mn atoms on the sample and the metallic tip. Hence the magnetic field-dependent spin polarization of the tip can be well described by the Brillouin function:

$$\eta_{\text{tip}} = \eta_{\text{max}} \left(\frac{2S+1}{2S} \coth \left(\frac{2S+1}{2S} x \right) - \frac{1}{2S} \coth \left(\frac{1}{2S} x \right) \right), \quad (26)$$

with $x = \frac{g\mu_B S |\vec{B}|}{2k_B T}$, $g = 2$, $S = 5/2$, and a maximal polarization $\eta_{\text{max}} = 0.5 \pm 0.05$.

Utilizing this spin-polarized tip at magnetic fields leads to spectra on the Co atoms as displayed for $B = 5$ T in figure 14. The two spectra differ by the adsorption site of the Co atom and therefore correspond to the situation where the magnetic field is either applied along (a) or perpendicular (b) to the main anisotropy axis (see also figure 13a). These spectra can be excellently fitted by using the sum of two double-step functions with step-energies symmetrically around zero-bias and asymmetric step-heights, and two Frota peak-functions (equation 22) at the energies of the energetically low-lying step, with identical half-width but different intensities. Surprisingly, the step-functions, that are due to inelastic spin-flip excitations, can be fully described in a second order transport model using the standard anisotropy Hamiltonian of equation 3 taking into account the spin-polarization governed by equation 26 [51, 91, 88].

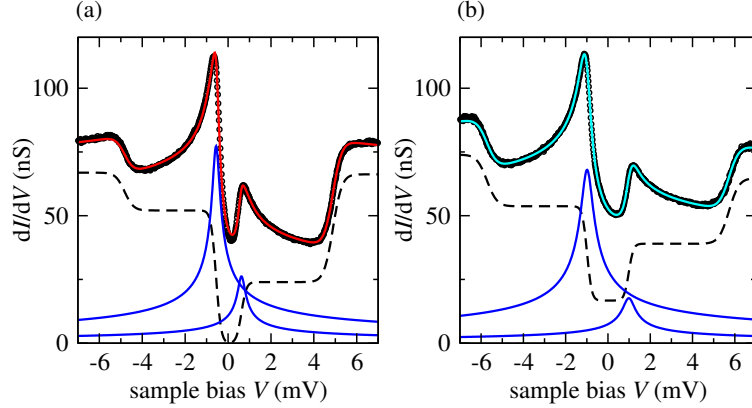


Figure 14: (a), (b) Experimental data (circles) measured on Co atoms on Cu₂N at $B = 5$ T applied along the vacancy row (a) and along the N-row (b). Stabilization setpoint $\sigma = 80$ nS, $V = +25$ mV, $I = 2$ nA. Upper solid line: best fit using the sum of an asymmetric double step function (dashed line) and two Frota functions (lower solid lines). Figure adapted from reference [51].

We now continue to evaluate spectra measured at different fields by subtracting the inelastic, step-like contributions, and analyzing the Kondo peaks using Frota functions as shown in figure 15a and 15b. Interestingly, the behavior of the Kondo peak seems to be related to the splitting energy as the data applied along the vacancy row and along the N-row fall on top of each other when plotted versus the peak energy ε_K . Plotted with this abscissa, the peak height h_K decays with $1/\varepsilon_K$ as shown in figure 15d.

From the peak width Γ_K^0 measured at $B = 0$ the Kondo temperature is extracted to $T_K = 2.4 \pm 0.2$ K, equal to the previously stated $T_K = 2.3 \pm 0.3$ K (Figure 13) [50], which corresponds to a correlation energy of $k_B T_K = 0.21$ meV. When the splitting exceeds this energy, we observe that the spectral weight of the correlated state, i.e. the area $h_k \times \Gamma_K$ underneath the Kondo peak, settles at about twice the zero field value and remains afterward constant irrespective of magnetic field strength up to 7 T or, equivalently, $\varepsilon_K \approx 6 \times k_B T_K$ (Figure 15e). Presumably, this stems from the lifting of the spin degeneracy of the Kondo singlet state at significant field. Note, that the transport measurement, as it is performed here, might introduce additional spectral weight created by the hot electrons at finite bias, similar as observed with spin-polarized currents on Fe atoms on Cu₂N [88] and rationalized with a 3rd order scattering transport model including rate-equations [40]. Here, however, we have not observed any strong current dependencies.

In the regime, where $\varepsilon_K > k_B T_K$, our data suggest a linear dependence of Γ_K on ε_K , (Figure 15c) which leads to a surprisingly simple equation:

$$\Gamma_K(\varepsilon_K) = (2 \pm 0.1)\Gamma_K^0 + (1 \pm 0.03)\frac{1}{\pi}\varepsilon_K, \quad (27)$$

where we relate the linear term to an increased scattering with bulk electrons which reduces the lifetime [91]. The factor 2 hints to an equal contribution of correlations induced by the bulk electrons and by the biased electrons in the transport experiment when ε_K exceeds the Kondo energy scale.

Finally, figure 15f shows that the effective polarization of the Kondo peak η_K^{eff} for the two different field directions stays approximately constant and is close to 0.5, with a small systematic offset between the two field directions. In order to derive the spin polarization of the split Kondo peak η_K , we need to consider the spin-polarization of the tip $\eta_{\text{tip}} \approx 0.5$ leading to:

$$\eta_K = \frac{\eta_K^{\text{eff}}}{\eta_{\text{tip}}} \approx 1.0. \quad (28)$$

In summary, this experiment shows that the split Kondo state is an excellent source for spin polarized electrons and might serve as a magnetic probe in transport measurements, similar to the fully spin-polarized

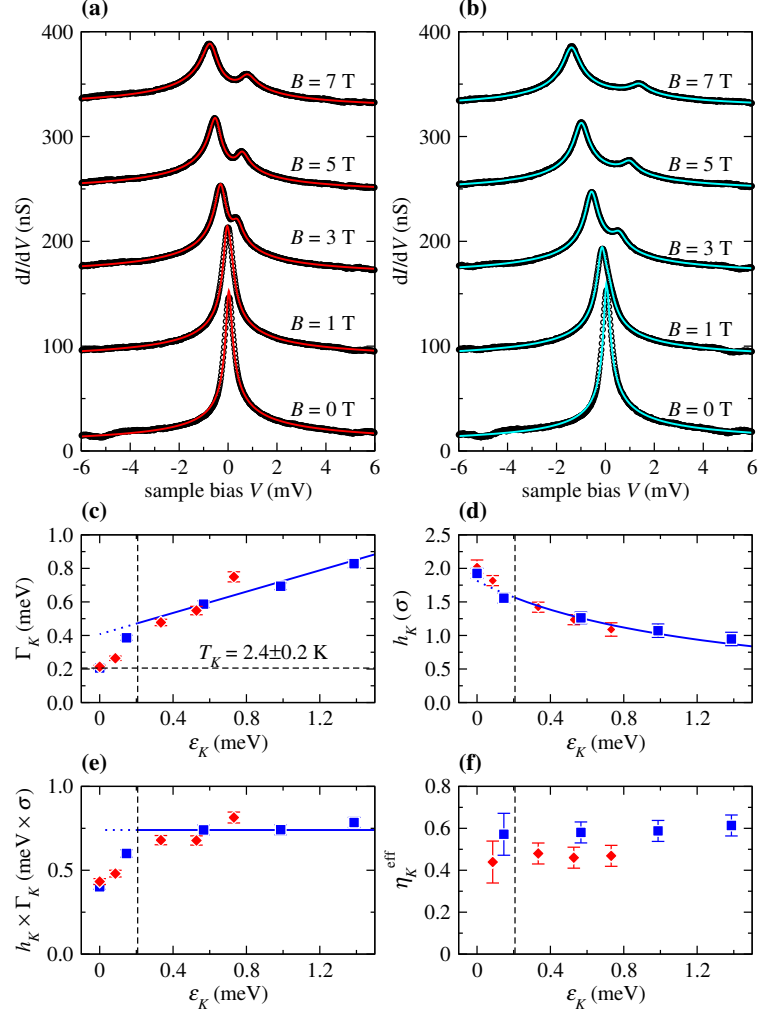


Figure 15: The splitting and the polarization of the Kondo peak. (a), (b) Kondo-related experimental data (circles) and fit with two Frota functions (solid lines) for magnetic fields applied along the vacancy row (a) and along the N-row (b). Curves in field are shifted vertically for better visualization. (c) Fit results for the width Γ_K , (d) the peak height h_K , (e) the area $\Gamma_K \times h_K$, and (f) the experimental peak asymmetry η_K^{eff} plotted against the splitting energy ε_K . Error bars indicate the 90% confidence interval of the fit and stem mainly from the interdependence of the parameters (nonzero off-diagonal covariance matrix elements). The horizontal and vertical dashed lines in (c)–(f) mark the characteristic Kondo energy. Figure adapted from reference [51].

magnetic field split superconducting state [151, 152]. Experimentally, this could be realized, for example, by attaching a magnetic molecule that exhibits a Kondo resonance to the tip apex. The Kondo resonance would then act as an energy-dependent spin filter for quantitative spin-resolved STM measurements.

4. Coupled spin systems

Up to now we have discussed the spectroscopic features due to second and third order scattering of electrons on single spin systems and the occurrence of correlation effects which lead to the Kondo effect. Now we will turn our attention to coupled systems where two or more individual spins interact. On one hand, this coupling can take place within a single molecule, where spin centers are coupled via exchange and superexchange interactions and the organic ligands control their properties, such as their anisotropies and effective spin states [153]. These molecules form a promising class of coupled spin systems called single molecule magnets and have been studied quite extensively (for a review see for example [42, 154, 153]). However, up to now few scanning tunneling spin excitation spectroscopy measurements have been performed due to the fragility of these molecules with complex geometry [52, 155] which, upon adsorption, easily alter their magnetic properties [156, 157, 158, 159, 160]. In section 4.1 we will briefly discuss the spectroscopic features measured on the prototypical single molecular magnet manganese-12-acetate [52].

On the other hand, the coupling between different spins can be achieved by deliberately organizing the individual spins, such as transition metal atoms, via lateral or vertical atom manipulation on thin insulating or metal substrates. Such experiments revealed, for example, that chains built of up to 10 Mn atoms on Cu₂N showed a pronounced odd-even behavior that was clearly visible in the spectroscopic data, which could be rationalized by considering the chains as a singular quantum mechanical object in which the Mn atoms are strongly coupled via Heisenberg exchange to their next neighbors [90, 161], and second-next neighbors [162]. Furthermore, bistable behavior and spin waves were observed in weakly antiferromagnetically coupled Fe chains on Cu₂N [163, 164]. Here, also ferromagnetically coupled 2D structures containing only a dozen Fe atoms demonstrated extremely long living Néel-states with lifetimes reaching hours at low temperatures [165]. Recently, it has been shown that the spin state of such structures can be read out by their influence onto the spin-dynamics of a near-by spin structure consisting of 3 Fe atoms [166]. Additionally, first successful attempts have been undertaken to use deliberately built spin-structures to explore the two-impurity Kondo system [53], the chiral magnetic interaction between atomic spin systems [167], or the quantum criticality of the *xxz* Heisenberg chain model [130].

In section 4.2 we will discuss the spectral features of a prototypical example: the antiferromagnetic coupling between two spins with $S = 1/2$ and $S = 1$. On such a system which has been recently studied in a vertical geometry, i. e. with the spins attached to tip and sample electrodes [168], we will show how correlations due to higher order scattering influences the spectrum. Then we will turn to the experimentally studied Fe-Co (section 4.3) [49] and Co-Co (section 4.4) [53] dimers on Cu₂N whereby the latter is an example for the two-impurity Kondo system [169, 170, 171] which can be deliberately tuned into different many-particle correlation phases. Furthermore, we will discuss correlation and entanglement in spin chains containing up to 12 spin sites which have been experimentally assembled from Fe and Mn atoms on Cu₂N [54].

4.1. The spectrum of a prototypical molecular magnet

In single molecular magnets, spin carrying atoms are arranged within a molecular framework in a way that their magnetic states can be described as a single giant spin. Manganese-12-acetate (Mn₁₂) is composed of a Mn₁₂O₁₂ core surrounded by 16 acetate groups and represents a prototypical molecular magnet with a total spin $S_T = 10$. Resulting from its relatively large magnetic anisotropy D , it has a magnetization reversal barrier height of $\Delta\varepsilon = DS^2 = 6$ meV in bulk, enough to produce very long spin relaxation times at low temperatures [172]. Throughout many studies, the immobilization of Mn₁₂ molecules at surfaces has been found to be difficult, as its fragile structure changes easily upon deposition, thus altering its magnetic properties [156, 157, 158, 159, 160]. To circumvent the fragmentation of the molecule during in-vacuo deposition due to its thermal instability, we use electrospray ion beam deposition (ES-IBD) as gentle

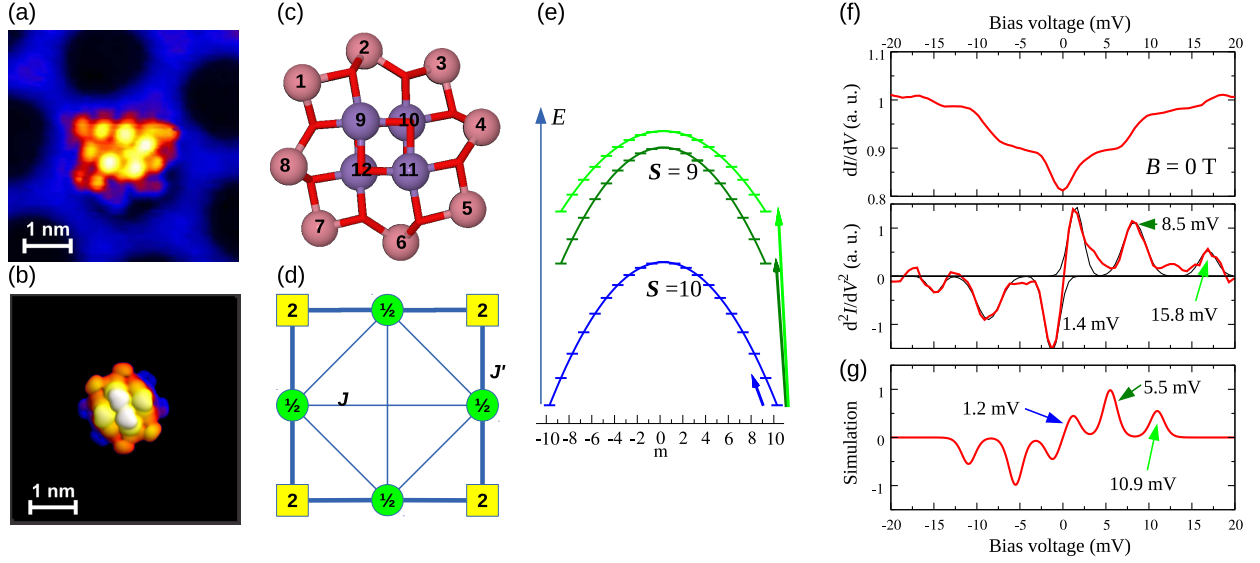


Figure 16: Spin excitations on the prototypical single molecular magnet $\text{Mn}_{12}\text{-Acetate}_{16}$. **(a)** STM constant-current topography of a Mn_{12} molecule adsorbed on $h\text{-BN/Rh(111)}$ measured at $T = 1$ K, $V = -1$ V, and $I = 45$ pA. **(b)** DFT calculation of the free molecule [52]. **(c)** Magnetic core of the Mn_{12} molecule. The 12 spin-sites are indexed. Pink circle correspond to a $S = 2$ site, violet circle to a $S = 3/2$ site. **(d)** Simplified 8-site model. **(e)** Schematic energy diagram of a Mn_{12} molecule in the giant spin approximation $H = DS_z^2$ with $S = 10$ ground state and easy axis anisotropy $D < 0$ without external magnetic fields applied. Arrows indicate possible excitations by interaction with the tunneling electron which obey the spin selection rule $\Delta m = 0, \pm 1$. **(f)** Typical dI/dV and d^2I/dV^2 spectra ($V = 100$ mV, $I = 20$ pA, $T = 1.5$ K) of a Mn_{12} molecule adsorbed on a $h\text{-BN/Rh(111)}$ surface at $B = 0$ T reveal low energy spin-flip excitations which manifest themselves as steps (peaks) in the dI/dV (d^2I/dV^2) spectrum. **(g)** Simulated d^2I/dV^2 spectra using the 8-spin model. Figure adapted from reference [52].

deposition method [173, 174, 175, 176, 177] to bring Mn_{12} molecules on the well-defined ultrathin insulating $h\text{-BN/Rh(111)}$ surface (Figure 16a).

To address the question of whether these molecules still exhibit their striking magnetic properties, we measured the differential conductance dI/dV at low temperature $T = 1.5$ K on top of the Mn_{12} molecules and observe symmetric features around the Fermi energy [52]. The spectra show a step-like structure in dI/dV which corresponds to peaks in the numerically derivated d^2I/dV^2 as shown in figure 16f. The innermost step is usually the most prominent one and can be found at 1–2 meV, while the outer steps can be observed in a range up to 16 meV. To interpret these features we omit for the moment the many spin nature of the system by using the giant spin approximation in which $S_T = 10$ is fixed. The magnetic anisotropy is responsible for the zero-field splitting of the spin eigenstates in the z -projection of the magnetic moment m_z and leads to a degenerate ground state for $|S_T, m_z\rangle = |10, -10\rangle$ and $|10, +10\rangle$ (see figure 16e). The model with fixed S_T reduces possible magnetic excitations to changes of m_z , explaining the inner step of the spectra at $\approx \pm 1.4$ mV as the excitation from $|S_T, m_z\rangle = |10, \pm 10\rangle$ to $|10, \pm 9\rangle$. In this approximation there are no transitions at higher energy possible which obey the conservation of angular momentum, i.e. which only changes m_z by ± 1 . Note, that this is also true when additional higher order anisotropy terms are accounted for in the Hamiltonian.

To cover excitations that change S_T , we have to go beyond the giant spin picture. The magnetic core of the Mn_{12} molecule contains 12 Mn atoms which are coupled via superexchange by oxygen bridges (Figure 16c). The eight ferromagnetically coupled outer atoms are thereby in the Mn^{3+} oxidation state and have an individual spin of $S = 2$ while the four inner atoms are in the Mn^{4+} state with a spin of $S = 3/2$ that are also ferromagnetically coupled [178]. Between the two ferromagnetically coupled sets of spins a strong antiferromagnetic coupling leads to a total spin of $S_T = 8 \times 2 - 4 \times 3/2 = 10$.

To calculate the low-energy eigenvalues and state vectors of the coupled spin system of the Mn_{12} molecule we use a simplified 8-site Hamiltonian which reduces the matrix size with n^2 elements from $n = 10^8$ to

acceptable $n = 10000$. In this model the exchange interaction of the four antiferromagnetically coupled dimers with the strongest coupling (1–9, 3–10, 5–11, 7–12 in figure 16c) are approximated by four spins $S = 2 - 3/2 = 1/2$ (Figure 16d) [178]. This can be done because the exchange interaction inside these dimers is much larger than all other exchange interactions and larger as the energy range of interest in our experiment. Thus, the four $S = 1/2$ "dimer" spins interact with each other and the remaining four $S = 2$ spins (sites 2, 4, 6, 8 in figure 16c).

We regard 3 types of exchange interactions in this system which are determined by DFT calculations [52] : (i) Easy-axis anisotropy on the individual spins $H_{\text{ani}} = D_z(\hat{S}_z^i)^2$, with $D_z = 0.48$ meV as the anisotropy term which is only relevant at the $S = 2$ sites due to the Kramer's degeneracy theorem. (ii) Direct Heisenberg spin-spin interaction $H_{\mathcal{J}} = \mathcal{J}_{ij}(\hat{\mathbf{S}}_i \cdot \hat{\mathbf{S}}_j)$, which couples different spin sites isotropically and has in the 8-spin model two distinct strengths: A relatively strong ferromagnetic coupling $\mathcal{J}' = -9.3$ meV between the $S = 2$ and $S = 1/2$ sites and a weaker coupling $\mathcal{J} = -0.25$ meV between the more distanced $S = 2$ sites. (iii) Non-collinear Dzyaloshinsky-Moriya interactions [179, 180] $H_{\text{DM}} = \mathcal{D}_{ij}(\vec{S}_i \times \vec{S}_j)$, in which the Dzyaloshinsky-Moriya vector parameter $\mathcal{D} = (2.1, 0, 0.1)^T$ meV couples neighboring $S = 2$ and $S = 1/2$ sites. Note, that similar anisotropy and coupling parameters have been found earlier by comparison to electron spin resonance measurements [178]. The total Hamiltonian is then diagonalized and the spin excitation spectrum is calculated up to second order in the scattering elements. The resulting spectrum (Figure 16g) agree well with the model, in particular considering that the influence of the substrate was neglected for the parameters of the Hamiltonian.

4.2. Coupling between a spin 1 and a spin 1/2

To gain insight into Kondo correlations in coupled structures, we will now continue the discussion with a rather small dimer system, which contains only two spin centers, one with $S^{(1)} = 1/2$ and the other with $S^{(2)} = 1$, where we want to assume that the degeneracies of the eigenstates are lifted by magnetic anisotropy of $D = -5$ meV and $E = 1$ meV (see section 2.1). When the isotropic antiferromagnetic Heisenberg exchange coupling \mathcal{J}_{12} between the two is switched on, we observe new step-like increases in the differential conductance that arise from spin-flip transitions on the $S^{(1)} = 1/2$ species that were absent before (Figure 17a and b). At small coupling strengths $\mathcal{J}_{12} \lesssim 1$ meV, the spectrum of the $S^{(2)} = 1$ is almost unaltered, while at higher coupling the energies and the intensities of the transitions change significantly. With increased antiferromagnetic coupling the inelastic transitions move to higher energy. On the spin-1 system the excitation step at lower energy decreases, while the excitation step at higher energy increases in intensity. In contrast, the step heights on the spin-1/2 system grow with increased coupling, whereas the energetically lower step is always significantly stronger than the energetically higher step. Most remarkably, with increased coupling the intensity of the zero-energy peak on the $S = 1/2$ spin diminishes while at the same time a zero-energy peak emerges at the $S = 1$ site.

To elucidate this behavior, we look at the (2×3) eigenstates of the combined system at a coupling $\mathcal{J}_{12} = |D| = 5$ meV (Figure 17c). These six states can be grouped into a doublet with the total spin expectation value of $\langle S_T \rangle \approx 1/2$ and $\langle m_z \rangle$ values of $\pm 1/2$.² This degenerate ground state doublet is separated from the four excited states with $\langle S_T \rangle \approx 3/2$ and $\langle m_z \rangle$ values of $\pm 1/2$ and $\pm 3/2$ by an energy of about $\frac{3}{2}\mathcal{J}_{12}$. Employing this set of states allows an easy rationalization of the observed spectroscopic features: The two symmetric steps in the conductance arise due to excitations of the system from the ground states $|\Psi_{1,2}\rangle = |S_T, m_z\rangle = |1/2, \pm 1/2\rangle$ to the excited states $|\Psi_{3,4}\rangle = |3/2, \pm 1/2\rangle$ and $|\Psi_{5,6}\rangle = |3/2, \pm 3/2\rangle$, induced by the tunneling electron. Note, that in these processes the total spin S_T is not conserved. Furthermore, we can attribute the zero-bias peak to scattering processes of third and higher orders between the two degenerate ground states $|\Psi_1\rangle$ and $|\Psi_2\rangle$.

²The total spin for a n -partite system is calculated as $\langle S_T \rangle = \sqrt{\langle \Psi | \hat{\mathbf{S}}_T^2 | \Psi \rangle + \frac{1}{4} - \frac{1}{2}}$, with $\hat{\mathbf{S}}_T^2 = \left(\bigotimes_{i=1}^n \hat{\mathbf{S}}_i \right)^2 = \left(\bigotimes_{i=1}^n \hat{S}_x^i \right)^2 + \left(\bigotimes_{i=1}^n \hat{S}_y^i \right)^2 + \left(\bigotimes_{i=1}^n \hat{S}_z^i \right)^2$. The total magnetic moment $\langle m_z \rangle$ is just the sum of the individual magnetic moments of the constituents.

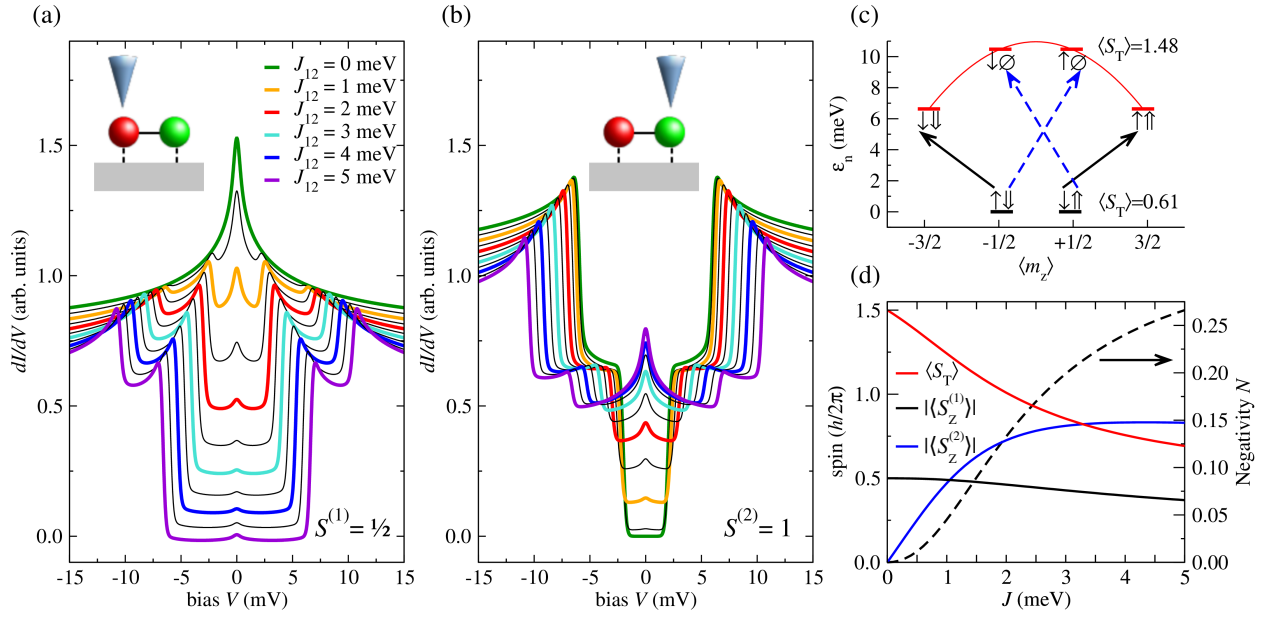


Figure 17: The spectra of an antiferromagnetically Heisenberg coupled dimer consisting of a $S^{(1)} = 1/2$ and a $S^{(2)} = 1$ system at $T = 1$ K and $B = 0$ T. **(a)** Simulated spectra on the $S^{(1)} = 1/2$ system for different coupling strengths. **(b)** Same as (a) for the $S^{(2)} = 1$ system with the anisotropy parameters $D = -5$ meV and $E = 1$ meV. Both spins are coupled to the substrate with $J\rho_s = -0.1$. Schematic insets illustrate the probing geometry. The spectra are shifted vertically with respect to each other for better visibility. **(c)** Schematic state diagram of the six eigenstates at a coupling strength of $J_{12} = 5$ meV. The black full arrow indicates the high transition rates on the $S^{(1)} = 1/2$ spin, the blue dashed arrows on the $S^{(1)} = 1$ spin, respectively. Arrows indicate the main m_z values of the combined state ($\uparrow = +1/2$, $\downarrow = -1/2$, $\uparrow\uparrow = +1$, $\emptyset = 0$, and $\downarrow\downarrow = -1$). **(d)** Full lines: Expectation values of the absolute magnetic quantum number $|\langle S_z^{(i)} \rangle|$ on each part of the dimer and the total quantum number $\langle S_T \rangle$ of the combined system for one of the two ground states. Dashed line: Negativity N as a measure of the quantum entanglement of the two spin systems.

The description of the eigenstates with quantum numbers S_T and m_z allows an easy understanding of even complex spin systems, but it fails to explain the different spectra of the individual parts of the dimer. Here, it is necessary to analyze the contributions to the states in the $|m_z^{(1)}, m_z^{(2)}\rangle$ basis, for which the main contributions are illustrated in figure 17c. The two ground states have the most weight in $|+1/2, -1\rangle$ and $|-1/2, +1\rangle$, respectively. Thus, the second order transition matrix elements to the low-lying excited states (at an energy of about 6.5 meV) are large, when the tunneling electron interacts with the $S^{(1)} = 1/2$ spin. The reason is that this transition requires a change of $\Delta m_z = \pm 1$ on the $S^{(1)}$ spin while the m_z value of the $S^{(2)}$ spin remains unchanged. In contrast, these transitions are unfavorable for a tunneling electron that interacts with the $S^{(2)}$ spin. However, on this site transitions to the high-lying excited states are preferred because they end in states with unchanged $m_z^{(1)}$ and a difference between initial and final $m_z^{(2)}$ of ± 1 .

Interestingly, the coupling has an effect on the spin-1 states similar to an applied magnetic field along the z -axis. Without coupling, the ground state is an antisymmetric superposition of the $m_z = \pm 1$ states, as discussed in section 2.1, leading to a total magnetic moment $\langle m_z \rangle = 0$. The Heisenberg coupling induces a duplication of states that effectively separates the m_z states and leads for the individual states of the $S = 1$ subsystem to an effective magnetization (Figure 17d). At $\mathcal{J}_{12} = 5$ meV the absolute magnetization for each ground state has reached ≈ 0.8 , where the difference to one stems mainly from some weight in $m_z = 0$. Similarly, the coupling decreases the average magnetization of the $S = 1/2$ subsystem, concomitant with the change of the total spin of the bipartite system approaching $S_T = 1/2$.

Both effects are a consequence of the emergence of quantum entanglement between the two spins which finally allows a description of the eigenstates in quantum numbers of the total spin S_T and the total magnetic moment m_z . There are many different approaches to measure quantum entanglement [181, 182, 183] that are based, for example, on the formation or distillation of entanglement [184], the entropy [185, 186, 187], the concurrence [188], or the tangle [189, 190]. Here, we will restrict ourselves to the "negativity" \mathcal{N} [191, 192, 193], which is the sum of the negative eigenvalues λ_j of the partially, with respect to the subsystem Γ_i of the i -th spin, transposed density matrix χ^{Γ_i} :

$$\mathcal{N}_i(\chi^{\Gamma_i}) = \sum_j \frac{|\lambda_j| - \lambda_j}{2}, \quad (29)$$

with χ as the total density matrix of the full system. The negativity is an excellent measure of the non-separability for spin-1/2 and spin-1 composite quantum systems enabling the quantization of non-classical quantum correlations [194, 195]. In the dimer system discussed here, the negativity \mathcal{N} increases steadily with the coupling \mathcal{J}_{12} , reaching $\mathcal{N} \approx 0.27$ at $\mathcal{J}_{12} = 5$ meV, close to the maximal possible entanglement in this system of $\mathcal{N} = 1/3$ at $\mathcal{J}_{12} \rightarrow \infty$ (Figure 17d).

These quantum correlations are the origin for the zero-energy peak at the spin-1 system. Naïvely, scattering between the two groundstates should be forbidden because it would require a spin-flip action on both subsystems when considering only the ground state components shown in figure 17c. It is the entanglement that gives weights to other components and leads finally to the appearance of logarithmic zero-bias peaks, which will diminish at the spin-1/2 site and grow at the spin-1 site when the coupling strengths $J\rho_s^{(1)}$ and $J\rho_s^{(2)}$ of both subsystems are equal.

Interestingly, this situation changes when $J\rho_s^{(1)} \neq J\rho_s^{(2)}$. Figure 18 displays the peak intensities at the sites of the two spins for different ratios of coupling strength to the substrate electrons and antiferromagnetic Heisenberg interactions. Surprisingly, when one of the $J\rho_s$ is small compared to the other, dips in the spectra can occur at certain Heisenberg coupling strengths (see insets in figure 18a and b). Note, that third order contributions can be significant even at negligible coupling to the substrate for the corresponding spin because of spin-spin interactions of electrons that originate and end in the substrate on other spins of the coupled system. When the spins are entangled, processes acting on all subsystems have to be accounted for and can interfere with each other. Figures 18c and 18d schematically illustrate the processes for a dimer: A tunneling electron scatters at the spin in proximity of the tip, leaving it in an intermediate state. The final state can now be reached either by a scattering event on this spin or on the other spin of the coupled system.

A dip-like reduction of the differential conductance at zero bias only occurs if one spin is loosely coupled

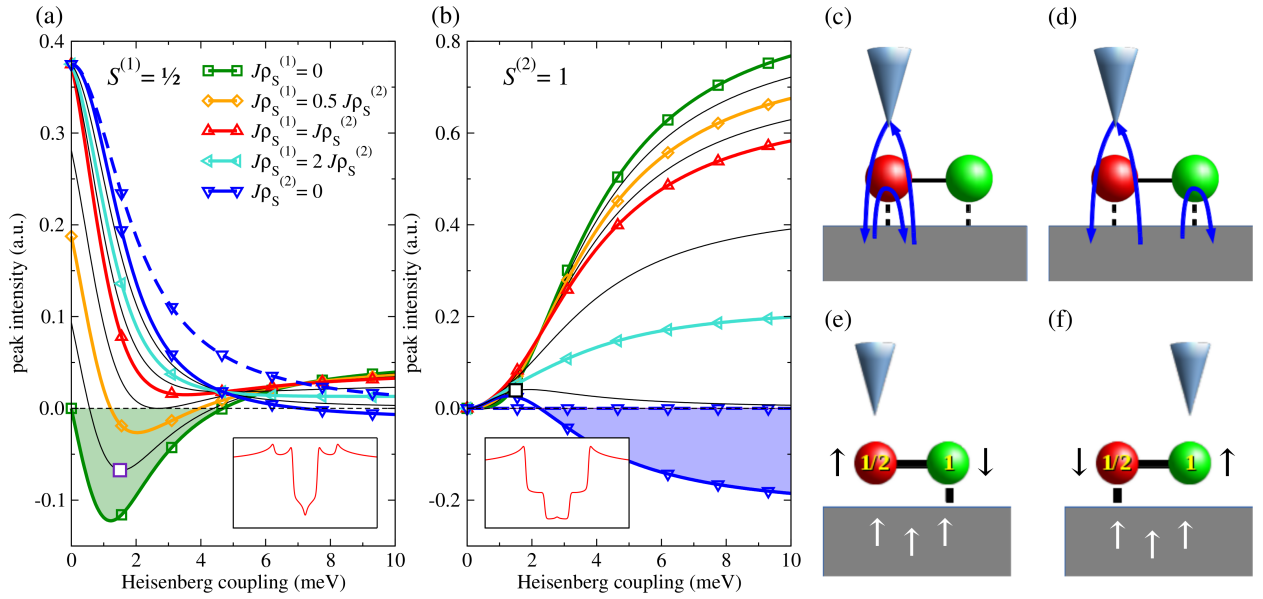


Figure 18: Zero bias peak intensities for a coupled dimer consisting of a $S^{(1)} = 1/2$ and a $S^{(2)} = 1$ spin ($D = -5$ meV, $E = 1$ meV) with different Heisenberg interactions \mathcal{J}_{12} and coupling strengths $J\rho_s$ to the substrate. **(a)** Peak intensities when the differential conductance is measured on the $S^{(1)} = 1/2$ spin. **(b)** Same as (a) when measured on the $S^{(2)} = 1$ spin. Dashed lines: Ising-like $\mathcal{J}_{12} = (0; 0; J_z)$ coupling at $J\rho_s^{(2)} = 0$. Insets in (a) and (b) illustrate the spectra at $\mathcal{J}_{12} = 1.5$ meV (white squares), with $J\rho_s^{(1)} = -0.025$, and $J\rho_s^{(2)} = -0.1$ at $T = 1$ K. The bias range is from -15 to $+15$ meV. **(c+d)** In third order scattering processes that originate and end in the substrate and interact on the probed spin (c) or on any other spin of the coupled spin-system (d) have to be accounted for. **(e)** Schematic of the situation illustrated by the green-shaded area in (a): The $S^{(1)} = 1/2$ is ferromagnetically coupled to the substrate electrons by superexchange via the $S^{(2)} = 1$ spin, leading to a dip in the spectrum. **(f)** Same as (e) for the blue-shaded area in (b).

to the substrate and a significant exchange interaction is established between the two subsystem. At low enough temperature, the states of the strongly coupled spin are antiferromagnetically correlated with the substrate electrons (see section 3), while the weakly coupled spin is ferromagnetically correlated with the substrate bath via the Heisenberg interaction (Figure 18e and f). This is equivalent to a ferromagnetic Kondo effect, which has been recently proposed to emerge for a triple spin system [196]. Note, however, that this requires a Heisenberg exchange interaction between both spins. If the interaction is Ising-like, i.e. couples only one direction of the magnetic moments, merely classical correlations occur, which are not sufficient to create the entanglement required to observe the Kondo effect for the spin-1 system (see dashed lines in figure 18a and b). However, the results presented here are obtained in the weak coupling limit. While it is known that a single spin will become asymptotically free for $T \rightarrow 0$ when ferromagnetically coupled to an electron bath [95, 197], it is not clear what happens in the coupled structures discussed here, where one spin is ferromagnetically and the other antiferromagnetically coupled to the substrate.

Note, that the two spins can be coupled also vertically by having one spin center adsorbed to the tip apex and the second one onto the substrate surface. In this situation, the antiferromagnetic exchange coupling has been found to be proportional to the tunneling coupling which depends exponentially on the distance between the two spins on tip and sample [198, 168]. Building a similar structure as discussed in this section with a $S = 1$ spin adsorbed on the sample and a strongly correlated half-integer spin on the tip lead to the observation of bias direction dependent step asymmetries at the energetically outer steps (blue dashed lines in Fig. 17d). These asymmetries enable to directly determine the correlation strength between the half-integer spin and the supporting electron bath [168].

4.3. Fe-Co dimers on Cu_2N

Dimer spin systems have been studied experimentally for different transition metal atoms on metallic and insulating surfaces. For Co atoms on Au(111), which show a pronounced Kondo effect with a $T_K \approx 70$ K, the disappearance of the Kondo effect due to the formation of a non-magnetic singlet state was observed only when the two adatoms were strongly coupled by placing them on neighboring adsorption sites [199]. In a similar experiment using Cu(100), the exchange interaction could be varied concomitantly with a change of the spectroscopic signature [200]. More recently, the coupling between two Kondo systems was established by attaching one Co atom to the apex of a Au tip and having the second Co atom adsorbed on a Au(111) surface [201] or between metal-molecule complexes in a non-consummate molecular lattice on Au(111) [202]. Furthermore, spin-spin interactions have been studied between Fe-Fe [66], Co-Co [53], and Co-Fe [49] adatoms adsorbed on Cu_2N .

We will revisit the latter Co-Fe dimer system and compare it to simulations done in the third order scattering model presented in reference [40]. In the experiment the two spins are separated by 0.72 nm and only weakly coupled via the Cu_2N surface (see inset of figure 19a), but the measurements of the differential conductance on both atoms reveal a change in the spectra compared to the individual atoms as discussed in section 2.3 and 3 and shown in figure 19a and b.

Simulating the data by using parameters almost identical to those employed for uncoupled single Co and Fe atoms, and an additional isotropic Heisenberg interaction of $\mathcal{J}_{12} = 0.16$ meV, renders the spectra obtained for the Fe atom almost perfectly, but only the main features and not all details are reproduced for the spectra measured on the Co atom. This stems from the fact, that our model only accounts for third order scattering contributions, neglecting higher order effects and reaches its limits in systems in the strong-coupling Kondo regime (see section 3.2).

At zero field we observe on the Fe atom a reduction of the intensity of the low-energy conductance steps compared to the uncoupled atom (Figure 7a). Furthermore, these steps diminish when a field along the main anisotropy axis of the Fe atom (z -axis) is applied, much more quickly than for the uncoupled Fe atom. Nevertheless, the overall spectral form is only weakly influenced by the coupling to the Co atom. The coupling is also not strong enough to produce a zero-energy feature at the high spin in this dimer, i.e. the Fe atom, as we would expect from the discussion of the coupled $S^{(1)} = 1/2$ and $S^{(2)} = 1$ system (Section 4.2). This can be understood by looking at the density matrices of the two degenerate groundstates of the combined system (Figure 19c and d). The two groundstates contain only contributions with weights at high $m_z = \pm 2$ values, inhibiting any scattering between them. Note that a description via quantum numbers

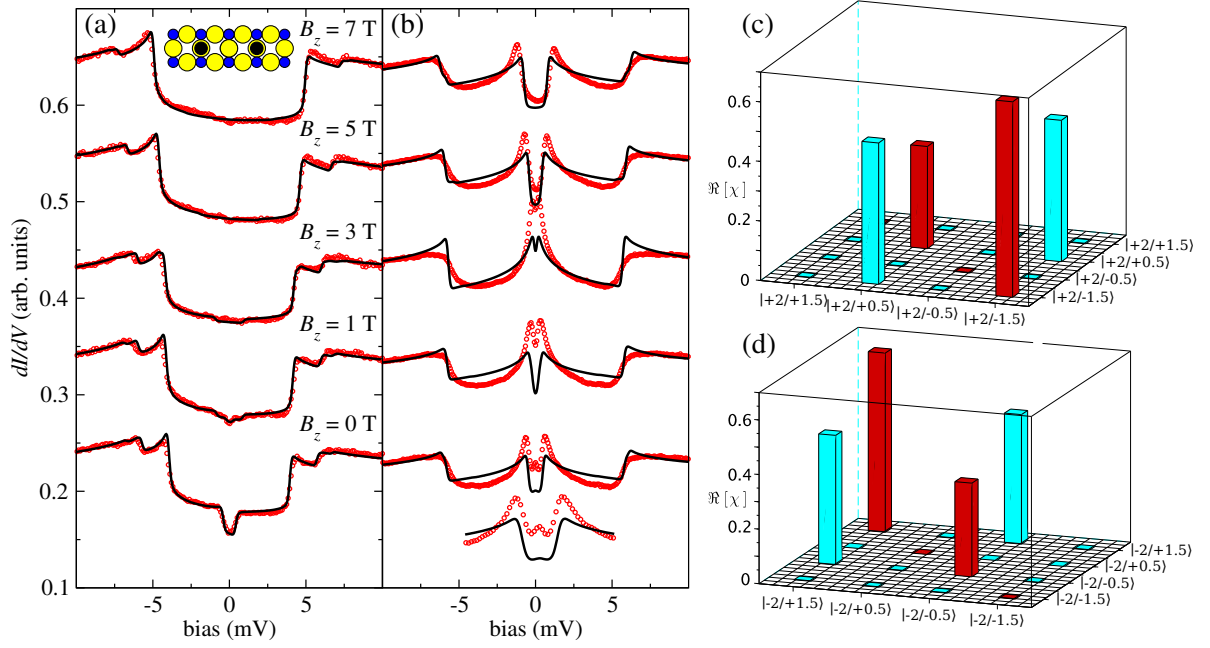


Figure 19: Tunneling spectra measured on a weakly coupled Co-Fe dimer on Cu_2N . **(a+b)** Experimental data from reference [49] obtained with the tip placed on top of the Fe (a) and Co (b) atom of the bipartite system at different fields applied along the main anisotropy axis of the Fe measured at $T = 550$ mK (red circles). The simulations (black lines) are performed using the following parameters for the Fe atom: $D = -1.53$ meV, $E = 0.31$ meV, $g = 2.11$, $J\rho_S = -0.085$, and $U = 0.35$; for the Co atom: $D = 2.7$ meV, $E = 0.5$ meV, $g = 2.16$, $J\rho_S = -0.25$, and $U = 0$. Note, that the main anisotropy axis for the Fe is along the N-rows, while for the Co it is along the vacancy rows. The isotropic Heisenberg exchange coupling between both atom was fixed to $\mathcal{J}_{12} = 0.16$ meV. Curves are vertically offset for clarity. The inset in (a) shows the adsorption site of the 3d atoms (black circle) on the Cu_2N (Cu yellow, N blue circle). The lowest curves in (b) are a zoom of the zero-field data measured on the Co atom. **(c + d)** Graphical representation of the real part of the reduced density matrices of the two lowest, at zero-field degenerated, ground states. The displayed parts contain $> 95\%$ of the state weights. The labels correspond to the $|m_z^{\text{Fe}}, m_z^{\text{Co}}\rangle$ values.

of the total system is not appropriate here due to the small coupling strength. Only when the Heisenberg coupling is comparable to the anisotropy energies, i.e. at $\mathcal{J}_{12} \gtrsim 3$ meV, these quantum numbers become a good description of the total system and the emergence of a zero-energy peak at the Fe atom is expected, similar to the dimer with $S^{(1)} = 1/2$ and $S^{(2)} = 1$.

Compared to the spectrum measured on the Fe atom, the zero-field spectrum on the Co atom is strongly affected by the creation of this bipartite system. Similar as for the $S^{(1)} = 1/2$ and $S^{(2)} = 1$ dimer, we observe in the experimental data, as well as in the simulation, conductance steps and peaks at an energy corresponding to the first excitation energy of the Fe atom. Additionally, the remainder of the zero-bias Kondo peak is clearly visible, but similar as in the example of the last section, the coupling to the Fe atom has already strongly reduced its intensity. At an applied field along the easy axes of both atoms, the energetic positions of the two peaks at low bias move towards zero and at a critical field of $B_c = (g_{\text{Co}}\mathcal{J}_{12})/(g_0\mu_B) \approx 2.6$ T, a novel Kondo peak at zero bias emerges. At even higher fields the spectra resemble those of an uncoupled Co atom, as shown in Figure 11, where the presence of the Fe atom has reduced the magnetic field to $B_{\text{eff}} = B_{\text{ext}} - B_c$.

Overall, it is surprising how well the perturbative model can reproduce the experimental data for this bipartite systems. Note, that not only does it enable us to determine the coupling strength and sign between interacting spins, but it also allows us to detect additional non-collinear couplings such as the Dzyaloshinskii-Moriya interaction, as it has been recently shown [167].

4.4. Co-Co dimers on Cu_2N

We now turn to the case where two Co atoms with $S = 3/2$ are coupled via Heisenberg interactions on the Cu_2N substrate [53]. This situation is in particular interesting, because at low enough temperature both spin sites form independently a correlated Kondo state with the substrate electrons as discussed in section 3. We have seen that the characteristic correlation energy of the Kondo state is $\Gamma_K = k_B T_K \approx 0.2$ meV (see section 3.4). This energy scale is of the same order as the Heisenberg exchange coupling strength in the previously discussed Fe-Co dimers. As illustrated in figure 20a, the competition between these two effects in combination with an external magnetic field embodies rich physics ranging from a correlated singlet or triplet state to complex Kondo states and has been of considerable theoretical interest since decades [203, 169, 170, 171, 204, 205, 206, 207, 208, 209]. Despite several studies on coupled quantum-dots [210, 211] and atoms [201, 212, 202], so far few experimental observations have been reported of the regime where both interactions have similar strengths and are thereby in direct competition with each other.

When the coupling \mathcal{J}_{12} is negligible compared to Γ_K and the magnetic field is zero, then the two spins are independently Kondo screened. An applied magnetic field which is strong enough will destroy the correlations between the localized spin and the bulk electrons as discussed in detail in section 3 leading to a situation where each spin acts like a free local magnetic moment.

The situation changes when \mathcal{J}_{12} is at similar order as Γ_K . For either sign of \mathcal{J}_{12} , the four lowest ground states of the combined spins govern now the behavior of the dimer. The zero-field energy difference between the lowest and the highest state of the quartet is thereby $4\mathcal{J}_{12}$ (see figure 20b and 20c). In the limit of $|\mathcal{J}_{12}|$ being much smaller than the magnetic anisotropy $|D|$ of the individual spins, the difference between the ground state and the first excited state is either $5/2\mathcal{J}_{12}$ or $3/2\mathcal{J}_{12}$ for anti-ferromagnetic (AFM) or ferromagnetic (FM) coupling, respectively. This different behavior enables even at zero-field to distinguish clearly from differential conductance measurements between AFM and FM coupled dimers [53].

In the case of FM coupling, the ground state can be written in the m_z base of the two spin sites as $\Psi_{\text{FM}} = \frac{1}{\sqrt{2}} (|+\frac{1}{2}, -\frac{1}{2}\rangle + |-\frac{1}{2}, +\frac{1}{2}\rangle)$, i.e. as the symmetric high-spin, low-magnetic moment triplet state. Any applied external magnetic field will polarize both spins moving the system closer to the free local magnetic moment regime as can be seen in figure 20b.

More interesting is the case where both spins are AFM coupled. The ground state in the m_z base of the two spin sites is the antisymmetric low-spin singlet state $\Psi_{\text{AFM}} = \frac{1}{\sqrt{2}} (|+\frac{1}{2}, -\frac{1}{2}\rangle - |-\frac{1}{2}, +\frac{1}{2}\rangle)$. This singlet state will compete with the many electron Kondo singlet between the *individual* spins and the substrate electrons. If the coupling \mathcal{J}_{12} is strong enough, the dimer-singlet becomes the energetically more favorable ground state and correlations with the substrate electrons concomitant with the Kondo peak disappear [53].

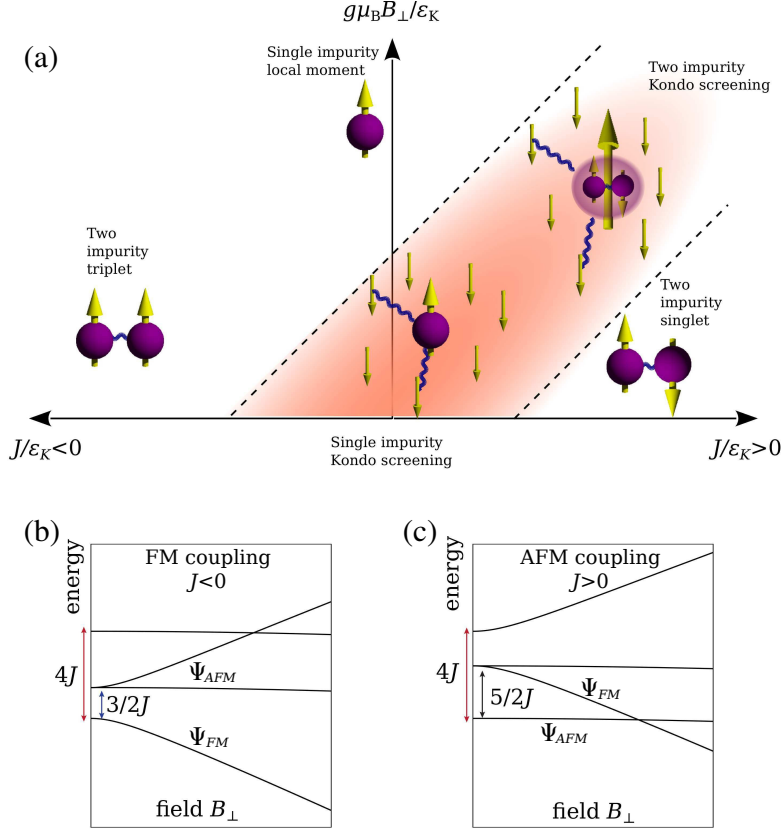


Figure 20: Phase diagram of the two-impurity Kondo problem. **(a)** Schematic phase diagram of two coupled Kondo-screened spins with varying interaction strength \mathcal{J}_{12} and external field B_\perp transverse to the main anisotropy axis of the individual spins with $S = 3/2$ and easy plane anisotropy $D > 0$. When $|\mathcal{J}_{12}|$ is small compared to the characteristic Kondo energy Γ_K , at $B = 0$ the two spins are independently screened by the substrate electrons, while for $|\mathcal{J}_{12}| \gg \Gamma_K$ a non-magnetic singlet or a high-spin triplet state form. For antiferromagnetic coupling, i. e. $\mathcal{J}_{12} > 0$, an applied magnetic field can lead to the formation of a new, combined correlated state in which both spins are screened. **(b + c)** Energy versus transverse magnetic field B_\perp of the four lowest energy states for ferromagnetic ($\mathcal{J}_{12} < 0$) and antiferromagnetic ($\mathcal{J}_{12} > 0$) coupling, respectively. In the ferromagnetic case (a) the groundstate ψ_{FM} does not change with applied field, while in the antiferromagnetic case, a state crossing between ψ_{FM} and ψ_{AFM} occurs at a critical field B_c . Figure adapted from reference [53].

However, as the state diagram in figure 20c suggests, a magnetic field orthogonal to the main anisotropy axis will decrease the energy difference between the ground state singlet and the lowest triplet state until the crossing field $B_c = (13/8) \times \mathcal{J}_{12}/(g\mu_B B_\perp)$ is reached, at which the two states become degenerate. At this point the two degenerated states ψ_{AFM} and ψ_{FM} form the basis for the emergence of a new Kondo state in which the substrate electrons are correlated with the *combined* state of the dimer [53].

4.5. Entanglement and the zero-energy peak in spin chains

Chains of exchange coupled spins have been of interest for studying fundamental questions since the early days of quantum mechanics, dating back to the exact solution found by H. Bethe [213] for the infinite spin-1/2 chain. Higher dimensional (anti-)ferromagnetically coupled spin lattices have led to the development of spin wave models [214, 215], which are the basis of descriptions of collective bosonic excitations, so called magnons, which have been observed in STM measurements, for example, on thin Co films on Cu(111) [216].

In one-dimensional spin-chains there is a peculiar difference between half-integer and integer spins: While infinite half-integer spin chains become gap-less [217], the energy difference between ground and first excited state in integer spins will always be finite, leading to the so called Haldane gap [218, 219]. Interestingly, as long as the magnetic anisotropy is small compared to the next-neighbor Heisenberg coupling strength, edge-states are expected to appear in finite integer spin-chains of odd lengths [220]. These half-spin degeneracies should reveal themselves by symmetric zero-energy Kondo peaks at the end of the chain together with a reduced lifetime. Very recently, the lifetime reduction at the ends of an antiferromagnetically coupled 3-spin Fe chain on Cu₂N has been observed [198]. Nevertheless, due to the relatively high magnetic anisotropy and low next-neighbor coupling strength, the formation of a zero-bias peak at the end was impeded.

Here, we want to explore and model spin-chains starting with the $S = 1$ and $S = 1/2$ dimer of section 4 where we assume an identical coupling $J\rho_0$ of the individual spins with the substrate and, for simplicity, a negligible magnetic anisotropy of the $S = 1$ spin. An antiferromagnetic Heisenberg interaction results then in a zero-bias peak mainly at the $S = 1$ site similar to the spectra shown in figure 17. To stay in the interesting $S^T = 1/2$ regime, we expand the dimer with additional $S = 1$ sites on the high-spin side, creating chains like $(1/2) \leftrightarrow (1) \leftrightarrow (1) \dots$. Now the question arises, where can we find the zero-bias peak for such chains and how will its intensity scale with the different parameters of the chain?

Figure 21a shows the differential conductance simulated for the different sites of an 11-spin chain where the first site is a spin-1/2 and all other sites are spin-1 without any magnetic anisotropy. The coupling between neighboring spins is $\mathcal{J}_{i,i+1} = 5$ meV and the coupling to the substrate is $J\rho_s = -0.1$ for all spins. Surprisingly, the zero-bias peak is strongest at the $S = 1$ end of the chain, extends spatially, and decays towards the $S = 1/2$ beginning of the chain. Furthermore, we observe many step-like inelastic excitations at increasing energy, which reveal rich features. The probabilities for second and third order scattering processes, i.e. the step heights and the additional peak-like structures, oscillate along the chain remarkably differently for the various excitation energies. This multitude of possible transitions stems from the enormous number of low lying excitations in this many-spin system. Figure 21b shows the 56 lowest eigenstates with energies $\varepsilon_n \leq 13$ meV. The groundstate is a doublet with total spin $S^T = 1/2$ and is separated by about 3.4 meV from the first excited states, a quadruplet with $S^T = 3/2$. However, there are many eigenstates in the chain that result in a total spin of 1/2 or 3/2, but with different contributions and weights of the individual spins. This is reflected in the oscillatory behavior of the transition probabilities and stems from the boundaries at the ends of the chain and the chain asymmetry, leading to a complex standing wave pattern for the coupling to the magnons of the chain [221, 222].

The amplitude of the zero-energy peak decays approximately exponentially along the chains as follows:

$$A_l(n) \approx A_l(l) \exp\left(\frac{l-n}{\lambda_l}\right). \quad (30)$$

Here, $A_l(n)$ is the peak amplitude measured at the n -th spin of a chain with length l , and λ_l is the decay length, which approaches $\lim_{l \rightarrow \infty} \lambda_l = 3$ for long chains. Odd-even fluctuations of the peak amplitude are due to some ferromagnetic exchange interactions of the spins in the chain with the substrate electron bath, similar to what we observed for the dimer (figure 18). Interestingly, the maximal zero-energy peak amplitude

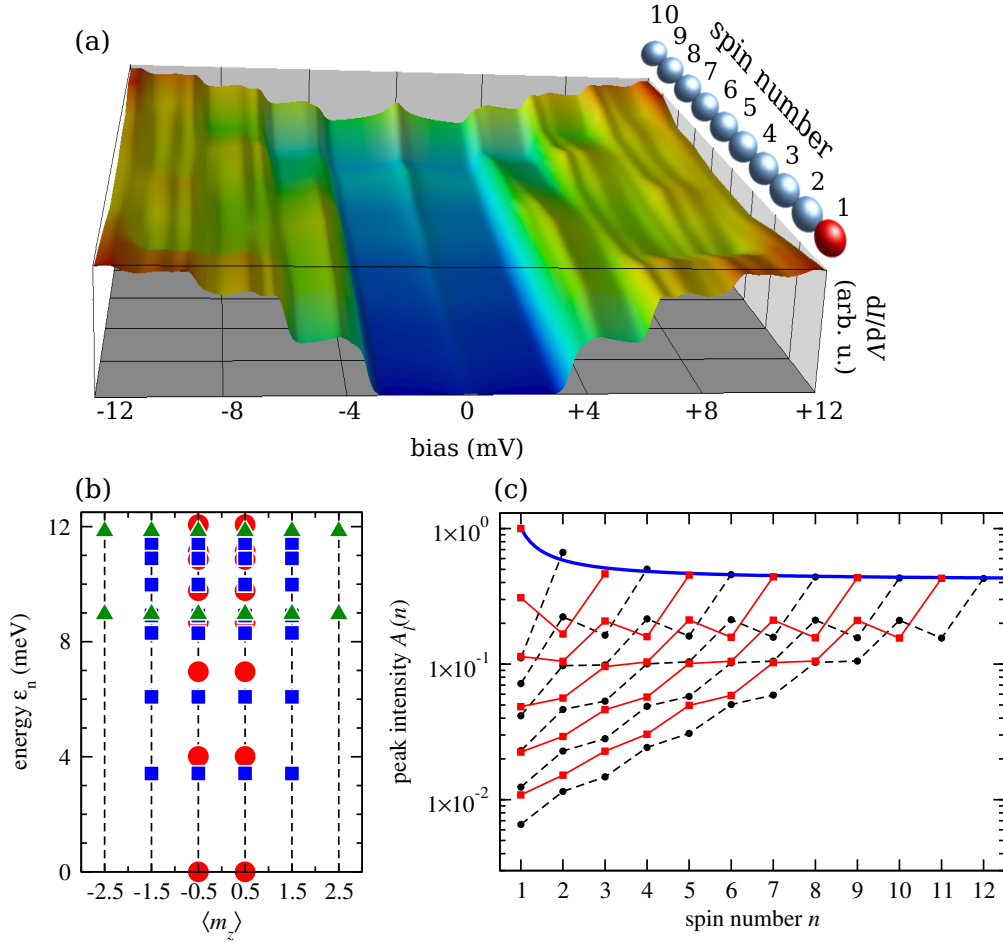


Figure 21: The zero-bias Kondo peak in spin chains without magnetic anisotropy. **(a)** 3D plot of simulated dI/dV spectra along a 10-spin chain with $S^{(1)} = 1/2$ (red sphere), $S^{(2)-(10)} = 1$ (gray spheres), $J\rho_s = -0.1$ on all spins, and a Heisenberg coupling between next neighbors of $\mathcal{J}_{i,i+1} = 5$ meV. **(b)** The energy of the lowest 56 eigenstates of the 10-spin chain in the giant spin basis $|S_T, m_z\rangle$. Red circles denote states with $S^T = 1/2$, blue squares with $S^T = 3/2$, and green triangles with $S^T = 5/2$, respectively. **(c)** Zero-bias peak intensity $A_l(n)$ for different chain lengths l with $S^{(1)} = 1/2$ and all other $S^{(n)} = 1$ relative to the peak intensity of a single $S = 1/2$ spin. Black circles and red squares mark the intensity $A_l(n)$ on the n -th spin for even and odd chain lengths, respectively. The thick blue line is a fit of the peak intensity of the last spin in the chain against the chain length l .

at the last spin of the chains diminishes for longer chains only slowly with $A_l(l) \approx 0.41A_1 \times l/(l - 0.59)$, and thus approaches a final value of $\approx 0.41A_1$ for long spin chains, with A_1 as the peak amplitude of a single $S = 1/2$ (see figure 21c).

This result is very remarkable. It means that the presence of a spin-1/2 at the beginning of an ideal, arbitrarily long, $S = 1$ chain determines the appearance of the zero-bias peak at the opposite end of the chain. Note that removing the spin-1/2 in chains with *odd* length results in an *even* spin-1 chain with a non-magnetic groundstate of $S_T = 0$ and a finite Haldane gap to the excited states [218]. Obviously, such a spin system cannot have any zero-bias peak.

Removing the spin-1/2 from chains with *even* length, makes the chain an *odd* chain that has a three-fold degenerate groundstate of $S^T = 1$ and topologically protected edge states which are expected to show a weak zero-energy peak at both ends of the chain [220]. Here too, the addition of a single spin-1/2 completely changes the properties.

Clearly, the ideal case as discussed above cannot be realized in real experiments. The adsorption of the spin-1 on a surface will break the symmetry inducing some magnetic anisotropy as we have discussed in section 2.1. Assuming an anisotropy of the same strength as the Heisenberg interaction between neighboring sites leads to much more quickly decaying peak-intensities (figure 22a and b). When the spin-1 sites have easy-axis anisotropy ($D < 0$) the peak-intensities drop very quickly and are only about $0.001A_1$ for a $l = 12$ chain. For the two groundstates the easy-axis anisotropy favors the high $m_z = \pm 1$ values at each site, and thus is effectively reducing any scattering between the groundstates. For easy-plane anisotropy ($D > 0$), which favors $m_z = 0$ values at each site, the peak-intensities do not drop as quickly, but the strongest peak occurs now no longer at the end of the chain, but is rather smeared out at approximately the center of the chain.

Interestingly, for all three cases discussed, the peak-intensities of the last spin of chains with different lengths l follow quite simple algebraic relations (see figure 22c):

$$\begin{aligned} A_l(l) &\approx A_1 \frac{0.41l}{l - 0.59}, & \text{if } D = 0, \\ A_l(l) &\approx 0.68A_1 \times l^{-0.84}, & \text{if } D = +\mathcal{J}, \\ A_l(l) &\approx 1.60A_1 \times \exp(-0.55l), & \text{if } D = -\mathcal{J}. \end{aligned} \tag{31}$$

Except for $D = 0$, all peak intensities decay either with an exponential law or an inverse power law. Note, that also for $|D/\mathcal{J}| \neq 1$ decay laws exist, which predict that the peak at the end of the chain disappears for $l \rightarrow \infty$.

We can understand this behavior if we look at the quantum mechanical entanglement inside the chain. For vanishing magnetic anisotropy the system is maximally entangled, while any anisotropy reduces the chain entanglement. To measure the entanglement inside the chain we calculate the negativity \mathcal{N}_n of different sites in the chain with respect to the total chain using equation 29. Figure 22d shows the results for a small chain of length $l = 6$ and different relative magnetic anisotropies D/\mathcal{J} . For moderately small easy-plane anisotropy or for easy-axis anisotropy, the entanglement of the total chain is strongest with the last spin, but decays with the strength of the magnetic anisotropy. For larger easy-plane anisotropy $D/\mathcal{J} \gtrsim 1$ the entanglement for spins closer to the beginning of the chain grows, and finally becomes larger than the entanglement with the chain end. Thus, quantum-mechanically, the chain separates in a moderately entangled short chain that consists of the spin-1/2 and a weakly entangled end chain.

Surprisingly, the entanglement measure correlates well with the calculated zero-bias peak intensities and positions. Thus, the observation of the Kondo peak at such spin chains is a direct measure of the quantum entanglement inside these chains. Recently, it was possible to verify this behavior in chains constructed atom-by-atom on Cu_2N with one Fe atom ($S = 2$) at the beginning and $2n + 1$ Mn atoms ($S = 5/2$) [54, 223]. The observations for these high-spin chains were similar to the calculations presented here. Chains up to FeMn_9 showed a spatially localized Kondo peak at the end of the chain. Due to the high spin of the chain constituents, odd chains of the form FeMn_{2n} showed no zero-bias peak because the groundstate of these chains is close to $S^T = 2$, the spin of the uncoupled Fe atom on Cu_2N .

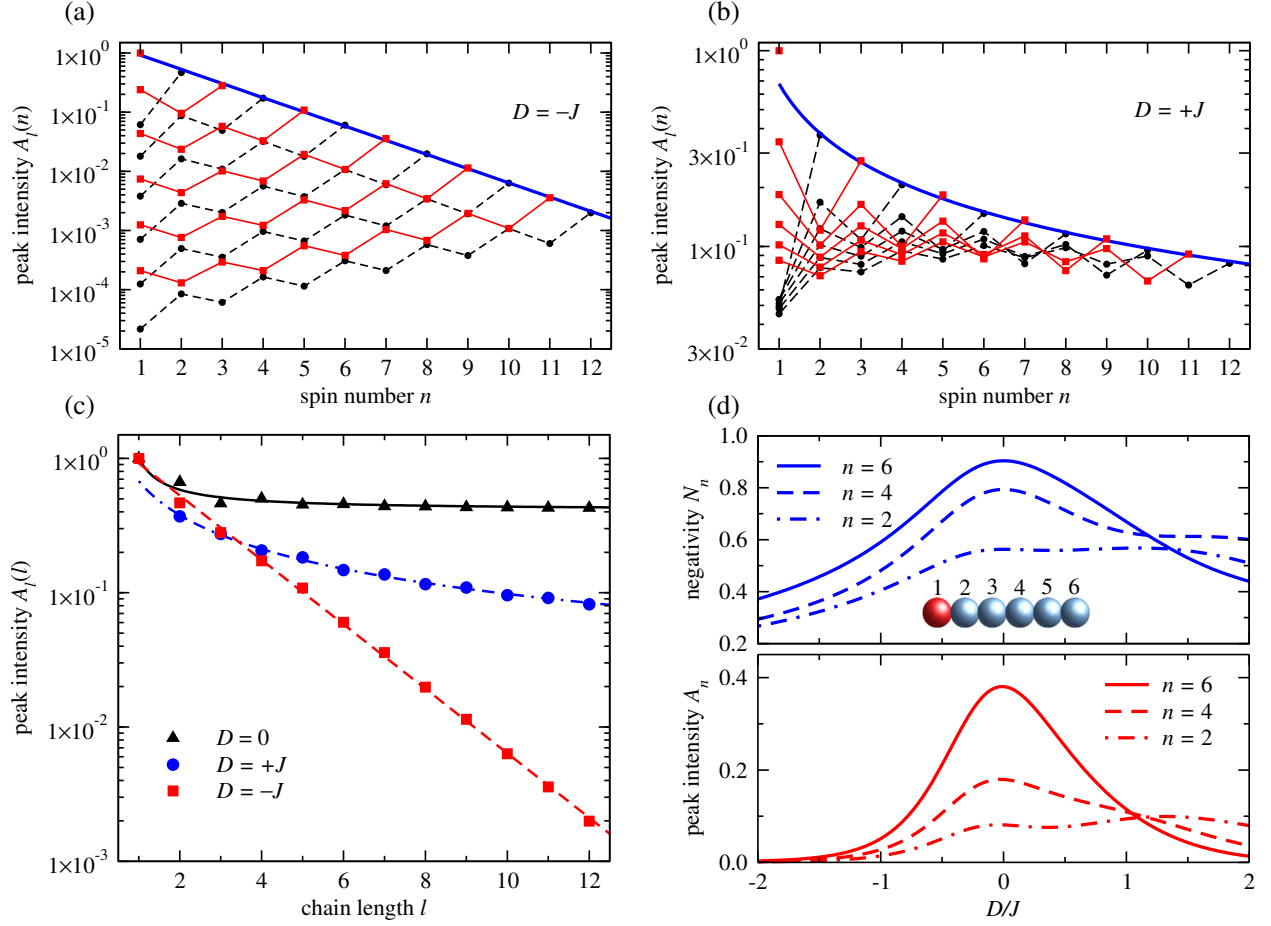


Figure 22: The zero-bias peak and entanglement in spin chains with different magnetic anisotropy. **(a+b)** Zero-bias peak intensity A_n for different chain lengths l with $S^{(1)} = 1/2$ and all other $S^{(n)} = 1$ relative to the peak intensity of a single $S = 1/2$ spin. In (a) easy axis anisotropy with $D = -J$, and in (b) easy plane anisotropy with $D = +J$ at the $S = 1$ sites is assumed. Black circles and red squares mark the intensity $A_l(n)$ on the n -th spin for even and odd chain lengths, respectively. The thick blue lines are fits of the peak intensity of the last spin in the chain against the chain length l . **(c)** Comparison of the decay of the zero-bias peak intensity with the chain-length l at the last spin A_l of chains with different anisotropy values. The full, dashed-dotted, and dashed line are fits with the corresponding decay function. **(d)** Comparison of the negativity N_n (top panel) and peak intensity A_n (bottom panel) of a 6-spin chain at different D/J ratios.

5. Summary and outlook

In this manuscript I have outlined how scanning tunneling spectroscopic methods can reveal the rich variety of effects individual and coupled quantum spins show when adsorbed on a supporting surface. The local environment influences the spins via crystal-field and spin-orbit coupling leading to magneto-crystalline anisotropy. Furthermore, we discussed how the exchange coupling to substrate electrons can drive the total quantum state into the highly correlated Kondo screening phase and how the very same interactions lead to renormalization effects influencing the anisotropy and the gyromagnetic factor. Not discussed in detail, but these interactions which couple the spin to the dissipative bath of the environment, are also of crucial importance for the state lifetime, coherence time, and the *einselection* of quantum states which generate classical behavior [224, 225].

Additionally, we inspected coupled spin systems and their ability to form entanglement. I expect that studying these non-classical correlations and their imprint in transport measurements, as for example seen in Kondo anomalies, will be of great importance for getting a deeper understanding of modern complex materials.

We have also seen that applying straight forward perturbation theory to such quantum spin systems allows to describe experimentally measured differential conductance spectra with very high accuracy. This enables one to obtain a profound understanding of the physical processes on play and to separate single- as well as many-electron effects, where perturbation theory and experiment must divert from each other.

Only during the last few years, both experiment and theory of individual and coupled spin systems have made tremendous progress. The versatility of low-temperature scanning tunneling measurements led me to believe that we should expect a multitude of exciting new experiments for the future, which will further deepening our fundamental knowledge on quantum systems in general and, in particular, quantum magnetism.

Acknowledgments

I like to thank the many people which have supported me for this manuscript: Kirsten von Bergmann, Oleg Brovko, Deung-Jang Choi, Katharina Franke, Andreas Heinrich, Tobias Herden, Cyrus Hirjibehedin, Peter Jacobson, Barbara Jones, Steffen Kahle, Klaus Kern, Alexander Khajetoorians, Gennadi Laskin, Sebastian Loth, Chris Lutz, Matthias Muenks, Stephan Rauschenbach, Anna Spinelli, Alexander Otte, Valerie Stepanyuk, Charlène Tonnoir, and Peter Wahl. I am also very grateful for the financial support by the Deutsche Forschungsgemeinschaft within the Sonderforschungsbereich at the University of Konstanz Controlled Nanosystems: Interaction and Interfacing to the Macroscale (SFB 767).

References

- [1] J. Frenkel. On the electrical resistance of contacts between solid conductors. *Phys. Rev.*, 36:1604, 1930.
- [2] I. Giaever. Energy gap in superconductors measured by electron tunneling. *Phys. Rev. Lett.*, 5:147, 1960.
- [3] I. Giaever. Electron tunneling between two superconductors. *Phys. Rev. Lett.*, 5:464, 1960.
- [4] N. B. Colthup, H. D. Lawrence, and S. E. Wiberley. *Introduction to Infrared and Raman Spectroscopy*. Academic Press, New York, 1990.
- [5] F. Hippert, E. Geissler, J. L. Hodeau, and J.-R. Regnard. *Neutron and X-ray Spectroscopy*. Springer, Dordrecht, The Netherlands, 2006.
- [6] R. C. Jaklevic and J. Lambe. Molecular vibration spectra by electron tunneling. *Phys. Rev. Lett.*, 17:1139, 1966.
- [7] J. Klein and A. Leger. Tunneling measurement of phonon spectrum in granular Al. *Phys. Lett. A*, 28:134, 1968.
- [8] J. M. Rowell, W. L. McMillan, and W. L. Feldmann. Phonon emission and self-energy effects in normal-metal tunneling. *Phys. Rev.*, 180:658, 1968.
- [9] J. Klein, A. Leger, M. Belin, and D. Defourneau. Inelastic-electron-tunneling spectroscopy of metal-insulator-metal junctions. *Phys. Rev. B*, 7:2336, 1973.
- [10] P. K. Hansma and J. Kirtley. Recent advances in inelastic electron tunneling spectroscopy. *Acc. Chem. Res.*, 11:440, 1978.
- [11] W. H. Weinberg. Inelastic electron tunneling spectroscopy: A probe of the vibrational structure of surface species. *Ann. Rev. Phys. Chem.*, 29:115, 1978.
- [12] A. F. G. Wyatt. Anomalous densities of states in normal tantalum and niobium. *Phys. Rev. Lett.*, 13:401, 1964.

- [13] E. L. Wolf and D. L. Losee. Spectroscopy of Kondo and spin-flip scattering: High-field tunneling studies of Schottky-barrier junctions. *Phys. Rev. B*, 2:3660, 1970.
- [14] A. F. G. Wyatt and R. H. Wallis. Exchange scattering in Ti-doped Al/Al oxide/Ag tunnel junctions. I. zero magnetic field. *J. Phys. C.: Solid State Phys.*, 7:1279, 1973.
- [15] A. F. G. Wyatt and R. H. Wallis. Exchange scattering in Ti-doped Al/Al oxide/Ag tunnel junctions. II. magnetic field. *J. Phys. C.: Solid State Phys.*, 7:1293, 1973.
- [16] S. Bermon, D. E. Paraskevopoulos, and P. M. Tedrow. Ultra-high magnetic field study of the Kondo-type zero-bias conductance peak in magnetically doped metal-insulator-metal tunnel junctions. *Phys. Rev. B*, 17:2110, 1978.
- [17] M. Ternes. *Scanning Tunneling Spectroscopy at the Single Atom Scale*. PhD thesis, École Polytechnique Fédérale de Lausanne, 2006. <http://library.epfl.ch/en/theses/?nr=3465>.
- [18] G. Binnig, H. Rohrer, Ch. Gerber, and E. Weibel. Surface studies by scanning tunneling microscopy. *Phys. Rev. Lett.*, 49:57, 1982.
- [19] G. Binnig, H. Rohrer, Ch. Gerber, and E. Weibel. Tunneling through a controllable vacuum gap. *Appl. Phys. Lett.*, 40:178, 1982.
- [20] G. Binnig, H. Rohrer, Ch. Gerber, and E. Weibel. 7×7 Si(111) resolved in real space. *Phys. Rev. Lett.*, 50:120, 1983.
- [21] D. P. E. Smith, G. Binnig, and C. F. Quate. Detection of phonons with a scanning tunneling microscope. *Appl. Phys. Lett.*, 49:1641, 1986.
- [22] B. C. Stipe, M. A. Rezaei, and W. Ho. Single-molecule vibrational spectroscopy and microscopy. *Science*, 280:1732, 1998.
- [23] L. J. Lauhon and W. Ho. Single-molecule vibrational spectroscopy and microscopy: CO on Cu(001) and Cu(110). *Phys. Rev. B*, 60:R8525, 1999.
- [24] A. J. Heinrich, C. P. Lutz, J. A. Gupta, and D. M. Eigler. Molecule cascades. *Science*, 298:1381, 2002.
- [25] M. Pivetta, M. Ternes, F. Patthey, and W. D. Schneider. Diatomic molecular switches to enable the observation of very-low-energy vibrations. *Phys. Rev. Lett.*, 99:126104, 2007.
- [26] F. D. Natterer, F. Patthey, and H. Brune. Quantifying residual hydrogen adsorption in low-temperature STMs. *Surf. Sci.*, 615:80, 2013.
- [27] S. Li, A. Yu, F. Toledo, Z. Han, H. Wang, H. Y. He, R. Wu, and W. Ho. Rotational and vibrational excitations of a hydrogen molecule trapped within a nanocavity of tunable dimension. *Phys. Rev. Lett.*, 111:146102, 2013.
- [28] F. D. Natterer, F. Patthey, and H. Brune. Resonant-enhanced spectroscopy of molecular rotations with a scanning tunneling microscope. *ACS Nano*, 8:7090, 2014.
- [29] T. M. Wallis, X. Chen, and W. Ho. Single molecule vibrational spectroscopy and microscopy: Cu(II) etioporphyrin-I on Cu(001). *J. Chem. Phys.*, 113:4837, 2000.
- [30] K. J. Franke and J. I. Pascual. Effects of electron-vibration coupling in transport through single molecules. *J. Phys.: Condens. Matter*, 24:394002, 2012.
- [31] A. J. Heinrich, J. A. Gupta, C. P. Lutz, and D. M. Eigler. Single-atom spin-flip spectroscopy. *Science*, 306:466, 2004.
- [32] J. T. Li, W. D. Schneider, R. Berndt, and B. Delley. Kondo scattering observed at a single magnetic impurity. *Phys. Rev. Lett.*, 80:2893, 1998.
- [33] F. Silly, M. Pivetta, M. Ternes, F. Patthey, J. P. Pelz, and W. D. Schneider. Creation of an atomic superlattice by immersing metallic adatoms in a two-dimensional electron sea. *Phys. Rev. Lett.*, 92:016101, 2004.
- [34] F. Silly, M. Pivetta, M. Ternes, F. Patthey, J. P. Pelz, and W. D. Schneider. Coverage-dependent self-organization: from individual adatoms to adatom superlattices. *New J. Phys.*, 6:16, 2004.
- [35] M. Ternes, C. Weber, M. Pivetta, F. Patthey, J. P. Pelz, T. Giamarchi, F. Mila, and W. D. Schneider. Scanning-tunneling spectroscopy of surface-state electrons scattered by a slightly disordered two-dimensional dilute “solid”: Ce on Ag(111). *Phys. Rev. Lett.*, 93:146805, 2004.
- [36] M. Ternes, M. Pivetta, F. Patthey, and W. D. Schneider. Creation, electronic properties, disorder, and melting of two-dimensional surface-state-mediated adatom superlattices. *Prog. Surf. Sci.*, 85:1, 2010.
- [37] M. Ternes, A. J. Heinrich, and W. D. Schneider. Spectroscopic manifestations of the Kondo effect on single adatoms. *J. Phys.: Condens. Matter*, 21:053001, 2009.
- [38] V. Madhavan, W. Chen, T. Jamneala, M. F. Crommie, and N. S. Wingreen. Tunneling into a single magnetic atom: Spectroscopic evidence of the Kondo resonance. *Science*, 280:567, 1998.
- [39] A. B. Shick, F. Máca, and A. I. Lichtenstein. Magnetic anisotropy of single 3d spins on a CuN surface. *Phys. Rev. B*, 79:172409, 2009.
- [40] M. Ternes. Spin excitations and correlations in scanning tunneling spectroscopy. *New J. Phys.*, 17:063016, 2015.
- [41] D. Gatteschi and R. Sessoli. Quantum tunneling of magnetization and related phenomena in molecular materials. *Angew. Chem. Int. Ed.*, 42:268, 2003.
- [42] D. Gatteschi, R. Sessoli, and D. Villani. *Molecular Nanomagnets*. Oxford University Press, 2006.
- [43] J. C. Oberg, M. R. Calvo, F. Delgado, M. Moro-Lagares, D. Serrate, D. Jacob, J. Fernández-Rossier, and C. F. Hirjibehedin. Control of single-spin magnetic anisotropy by exchange coupling. *Nature Nanotechnology*, 9:64, 2013.
- [44] P. Jacobson, T. Herden, M. Muenks, Laskin G., O. O. Brovko, V. S. Stepanyuk, M. Ternes, and K. Kern. Quantum engineering of spin and anisotropy in magnetic molecular junctions. *Nature Comm.*, 6:8536, 2015.
- [45] H. A. Kramers. Wellenmechanik und halbzahlige Quantisierung. *Z. Phys.*, 39:828, 1926.
- [46] J. Kondo. Resistance minimum in dilute magnetic alloys. *Prog. Theor. Phys.*, 32:37, 1964.
- [47] A. C. Hewson. *The Kondo Problem to Heavy Fermions*. Cambridge University Press, Cambridge, 1997.
- [48] Y. Zhang, S. Kahle, T. Herden, C. Stroh, M. Mayor, U. Schlickum, M. Ternes, P. Wahl, and K. Kern. Temperature and magnetic field dependence of a Kondo system in the weak coupling regime. *Nature Comm.*, 4:2110, 2013.
- [49] A. F. Otte, M. Ternes, S. Loth, C. P. Lutz, C. F. Hirjibehedin, and A. J. Heinrich. Spin excitations of a Kondo-screened

- atom coupled to a second magnetic atom. *Phys. Rev. Lett.*, 103:107203, 2009.
- [50] A. F. Otte, M. Ternes, S. Loth, K. von Bergmann, H. Brune, C. P. Lutz, C. F. Hirjibehedin, and A. J. Heinrich. The role of magnetic anisotropy in the Kondo effect. *Nature Physics*, 4:847, 2008.
 - [51] K. von Bergmann, M. Ternes, S. Loth, C. P. Lutz, and A. J. Heinrich. Spin-polarization of the split Kondo state. *Phys. Rev. Lett.*, 114:076601, 2015.
 - [52] S. Kahle, Z. Deng, N. Malinowski, C. Tonnoir, A. Forment-Aliaga, N. Thontasen, G. Rinke, D. Le, V. Turkowski, T. S. Rahman, S. Rauschenbach, M. Ternes, and K. Kern. The quantum magnetism of individual manganese-12-acetate molecular magnets anchored at surfaces. *Nano Lett.*, 12:518, 2012.
 - [53] A. Spinelli, M. Gerrits, R. Toskovic, B. Bryant, M. Ternes, and A. F. Otte. Exploring the phase diagram of the two-impurity Kondo problem. *Nature Comm.*, 6:10046, 2015.
 - [54] D.-J. Choi, R. Robles, S. Yan, J. A. J. Burgess, S. Rolf-Pissarczyk, J. P. Gauyacq, N. Lorente, M. Ternes, and S. Loth. Entanglement-induced Kondo screening in atomic spin chains. *arXiv:1507.04785 [cond-mat.mes-hall]*, 2015.
 - [55] D. Jacob and J. Fernández-Rossier. Competition between quantum spin tunneling and Kondo effect. *Eur. Phys. J. B*, 89:210, 2016.
 - [56] C. Rudowicz and C. Y. Chung. The generalization of the extended Stevens operators to higher ranks and spins, and a systematic review of the tables of the tensor operators and their matrix elements. *J. Phys.: Condens. Matter*, 16:5825, 2004.
 - [57] P. Gambardella, S. Rusponi, M. Veronese, S. S. Dhesi, C. Grazioli, A. Dallmayer, I. Cabria, R. Zeller, P. H. Dederichs, K. Kern, C. Carbone, and H. Brune. Giant magnetic anisotropy of single cobalt atoms and nanoparticles. *Science*, 300:1130, 2003.
 - [58] T. Miyamachi, T. Schuh, T. Märkl, C. Bresch, T. Balashov, A. Stöhr, C. Karlewski, S. Andre, M. Marthaler, M. Hoffmann, M. Geilhufe, S. Ostanin, W. Hergert, I. Mertig, G. Schön, A. Ernst, and W. Wulfhekel. Stabilizing the magnetic moment of single holmium atoms by symmetry. *Nature*, 503:242, 2013.
 - [59] B. W. Heinrich, G. Ahmadi, V. L. Müller, L. Braun, J. I. Pascual, and K. J. Franke. Change of the magnetic coupling of a metal-organic complex with the substrate by a stepwise ligand reaction. *Nano Lett.*, 13:4840, 2013.
 - [60] I. G. Rau, S. Baumann, S. Rusponi, F. Donati, S. Stepanow, L. Gragnaniello, J. Dreiser, C. Piamonteze, F. Nolting, S. Gangopadhyay, O. R. Albertini, R. M. MacFarlane, C. P. Lutz, B. A. Jones, P. Gambardella, A. J. Heinrich, and H. Brune. Reaching the magnetic anisotropy limit of a 3d metal atom. *Science*, 344:988, 2014.
 - [61] A. A. Khajetoorians, T. Schlenk, B. Schweglinghaus, M. dos Santos Dias, M. Steinbrecher, M. Bouhassoune, S. Lounis, J. Wiebe, and R. Wiesendanger. Spin excitations of individual Fe atoms on Pt(111): Impact of the site-dependent giant substrate polarization. *Phys. Rev. Lett.*, 111:157204, 2013.
 - [62] Q. Dubout, F. Donati, C. Wäckerlin, F. Calleja, M. Etzkorn, A. Lehnert, L. Claude, P. Gambardella, and H. Brune. Controlling the spin of Co atoms on Pt(111) by hydrogen adsorption. *Phys. Rev. Lett.*, 114:106807, 2015.
 - [63] F. Donati, Q. Dubout, F. Autés, Patthey, F. Calleja, P. Gambardella, O. V. Yazyev, and H. Brune. Magnetic moment and anisotropy of individual Co atoms on graphene. *Phys. Rev. Lett.*, 111:236801, 2013.
 - [64] A. A. Khajetoorians, M. Valentyuk, M. Steinbrecher, T. Schlenk, A. Shick, J. Kolorenc, A. I. Lichtenstein, T. O. Wehling, R. Wiesendanger, and J. Wiebe. Tuning emergent magnetism in a Hund's impurity. *Nature Nanotechnology*, 10:958, 2015.
 - [65] P. Jacobson, M. Muenks, Laskin G., O. O. Brovko, V. S. Stepanyuk, M. Ternes, and K. Kern. Potential energy driven spin manipulation via a controllable hydrogen ligand. *arXiv:1609.00612 [cond-mat.mes-hall]*, 2016.
 - [66] B. Bryant, A. Spinelli, J. J. T. Wagenaar, M. Gerrits, and A. F. Otte. Local control of single atom magnetocrystalline anisotropy. *Phys. Rev. Lett.*, 111:127203, 2013.
 - [67] F. Delgado, C. F. Hirjibehedin, and J. Fernández-Rossier. Consequences of Kondo exchange on quantum spins. *Surf. Sci.*, 630:337, 2014.
 - [68] T. Jurca, A. Farghal, P.-H. Lin, I. Korobkov, M. Murugesu, and D. S. Richeson. Single-molecule magnet behavior with a single metal center enhanced through peripheral ligand modifications. *J. Am. Chem. Soc.*, 133:15814, 2011.
 - [69] D. Wegner, R. Yamachika, X. Zhang, Y. Wang, T. Baruah, M. R. Pederson, B. M. Bartlett, J. R. Long, and M. F. Crommie. Tuning molecule-mediated spin coupling in bottom-up-fabricated vanadium-tetracyanoethylene nanostructures. *Phys. Rev. Lett.*, 103:087205, 2009.
 - [70] J. J. Parks, A. R. Champagne, T. A. Costi, W. W. Shum, A. N. Pasupathy, E. Neuscamman, S. Flores-Torres, P. S. Cornaglia, A. A. Aligia, C. A. Balseiro, G. K.-L. Chan, H. D. Abruña, and D. C. Ralph. Mechanical control of spin states in spin-1 molecules and the underscreened Kondo effect. *Science*, 328:1370, 2010.
 - [71] J. M. Zadrozny, D. J. Xiao, M. Atanasov, G. J. Long, F. Grandjean, F. Neese, and J. R. Long. Magnetic blocking in a linear iron(I) complex. *Nature Chem.*, 5:577, 2013.
 - [72] L. Ungur, J. J. Le Roy, I. Korobkov, M. Murugesu, and L. F. Chibotaru. Fine-tuning the local symmetry to attain record blocking temperature and magnetic remanence in a single-ion magnet. *Angew. Chem. Int. Ed.*, 53:4413, 2014.
 - [73] F. Donati, S. Rusponi, S. Stepanow, C. Wäckerlin, A. Singha, L. Persichetti, R. Baltic, K. Diller, F. Patthey, E. Fernandes, J. Dreiser, Ž. Šljivančanin, K. Kummer, C. Nistor, P. Gambardella, and H. Brune. Magnetic remanence in single atoms. *Science*, 352:318, 2016.
 - [74] W. A. Hofer, G. Teobaldi, and N. Lorente. Creating pseudo-Kondo resonances by field-induced diffusion of atomic hydrogen. *Nanotechnology*, 19:305701, 2008.
 - [75] T. Herden, M. Ternes, and K. Kern. Lateral and vertical stiffness of the epitaxial h-BN monolayer on Rh(111). *Nano Lett.*, 14:3623, 2014.
 - [76] R. Laskowski, P. Blaha, T. Gallauner, and K. Schwarz. Single-layer model of the hexagonal boron nitride nanomesh on the Rh(111) surface. *Phys. Rev. Lett.*, 98:106802, 2007.
 - [77] F. D. Natterer, F. Patthey, and H. Brune. Ring state for single transition metal atoms on boron nitride on Rh(111).

- Phys. Rev. Lett.*, 109:066101, 2012.
- [78] C. F. Hirjibehedin, C. Y. Lin, A. F. Otte, M. Ternes, C. P. Lutz, B. A. Jones, and A. J. Heinrich. Large magnetic anisotropy of a single atomic spin embedded in a surface molecular network. *Science*, 317:1199, 2007.
 - [79] N. Lorente and J. P. Gauyacq. Efficient spin transitions in inelastic electron tunneling spectroscopy. *Phys. Rev. Lett.*, 103:176601, 2009.
 - [80] J. A. Appelbaum. “ $s - d$ ” exchange model of zero-bias tunneling anomalies. *Phys. Rev. Lett.*, 17:91, 1966.
 - [81] P. W. Anderson. Localized magnetic states and Fermi-surface anomalies in tunneling. *Phys. Rev. Lett.*, 17:95, 1966.
 - [82] J. A. Appelbaum. Exchange model of zero-bias tunneling anomalies. *Phys. Rev.*, 154:633, 1967.
 - [83] J. Lambe and R. C. Jaklevic. Molecular vibration spectra by inelastic electron tunneling. *Phys. Rev.*, 165:821, 1968.
 - [84] C. Cohen-Tannoudji, J. Dupont-Roc, and G. Grynberg. *Atom-Photon Interaction*. Wiley and Sons, Inc., New York, 1989.
 - [85] C. Y. Lin and B. A. Jones. First-principles calculations of engineered surface spin structures. *Phys. Rev. B*, 83:014413, 2011.
 - [86] J. Fransson. Spin inelastic electron tunneling spectroscopy on local spin adsorbed on surface. *Nano Lett.*, 9:2414, 2009.
 - [87] S. Yan, D.-J. Choi, J. A. J. Burgess, S. Rolf-Pissarczyk, and S. Loth. Three-dimensional mapping of single-atom magnetic anisotropy. *Nano Lett.*, 15:1938, 2015.
 - [88] S. Loth, C. P. Lutz, and A. J. Heinrich. Spin-polarized spin excitation spectroscopy. *New J. Phys.*, 12:125021, 2010.
 - [89] A. Hurley, N. Baadji, and S. Sanvito. Perturbative approach to the Kondo effect in magnetic atoms on nonmagnetic substrates. *Phys. Rev. B*, 84:115435, 2011.
 - [90] C. F. Hirjibehedin, C. P. Lutz, and A. J. Heinrich. Spin coupling in engineered atomic structures. *Science*, 312:1021, 2006.
 - [91] S. Loth, K. von Bergmann, M. Ternes, A. F. Otte, C. P. Lutz, and A. J. Heinrich. Controlling the state of quantum spins with electric currents. *Nature Physics*, 6:340, 2010.
 - [92] W. Meissner and B. Voigt. Messungen mit Hilfe von flüssigem Helium XI Widerstand der reinen Metalle in tiefen Temperaturen. *Ann. D. Phys.*, 7:761, 1930.
 - [93] W. J. de Haas, J. de Boer, and G. J. van Den Berg. The electrical resistance of gold, copper and lead at low temperatures. *Physica*, 34:1115, 1934.
 - [94] J. Kondo. Effect of ordinary scattering on exchange scattering from magnetic impurity in metals. *Phys. Rev.*, 169:437, 1968.
 - [95] P. W. Anderson. A poor man’s derivation of scaling laws for the Kondo problem. *J. Phys. C.*, 3:2436, 1970.
 - [96] P. Gentile, L. de Leo, M. Fabrizio, and E. Tosatti. Lack of Kondo screening at nanocontacts of nearly magnetic metals. *Europhys. Lett.*, 87:27014, 2009.
 - [97] D. Goldhaber-Gordon, H. Shtrikman, D. Mahalu, D. Abusch-Magder, U. Meirav, and M. A. Kastner. Kondo effect in a single-electron transistor. *Nature*, 391:156, 1998.
 - [98] J. Nygård, D. H. Cobden, and P. E. Lindelof. Kondo physics in carbon nanotubes. *Nature*, 408:342, 2000.
 - [99] A. Kogan, S. Amasha, D. Goldhaber-Gordon, G. Granger, M. A. Kastner, and H. Shtrikman. Measurements of Kondo and spin splitting in single-electron transistors. *Phys. Rev. Lett.*, 93:166602, 2004.
 - [100] J. Paaske, A. Rosch, P. Wolffe, N. Mason, C. M. Marcus, and J. Nygård. Non-equilibrium singlet-triplet Kondo effect in carbon nanotubes. *Nature Physics*, 2:460, 2006.
 - [101] R. M. Potok, I. G. Rau, H. Shtrikman, Y. Oreg, and D. Goldhaber-Gordon. Observation of the two-channel Kondo effect. *Nature*, 446:167, 2007.
 - [102] A. V. Kretinin, H. Shtrikman, D. Goldhaber-Gordon, M. Hani, A. Weichselbaum, J. von Delft, T. A. Costi, and D. Mahalu. Spin-1/2 Kondo effect in a InAs nanowire quantum dot: the unitary limit, conductance scaling and Zeeman splitting. *Phys. Rev. B*, 84:245316, 2011.
 - [103] A. J. Keller, S. Amasha, I. Weymann, C. P. Moca, I. G. Rau, J. A. Katine, H. Shtrikman, G. Zarand, and D. Goldhaber-Gordon. Emergent SU(4) Kondo physics in a spin-charge-entangled double quantum dot. *Nature Physics*, 10:145, 2014.
 - [104] A. Georges, G. Kotliar, W. Krauth, and M. J. Rozenberg. Dynamical mean-field theory of strongly correlated fermion systems and the limit of infinite dimensions. *Rev. Mod. Phys.*, 68:13, 1996.
 - [105] P. Nozières. Kondo lattices and the Mott metal-insulator transition. *J. Phys. Soc. Jpn.*, 74:4, 2005.
 - [106] K. G. Wilson. The renormalization group: Critical phenomena and the Kondo problem. *Rev. Mod. Phys.*, 47:773, 1975.
 - [107] N. Andrei. Diagonalization of the Kondo Hamiltonian. *Phys. Rev. Lett.*, 45:379, 1980.
 - [108] F. Patthey, B. Delley, W. D. Schneider, and Y. Baer. Low-energy excitations in α - and γ -Ce observed by photoemission. *Phys. Rev. Lett.*, 55:1518, 1985.
 - [109] F. Patthey, W. D. Schneider, Y. Baer, and B. Delley. High-temperature collapse of the kondo resonance in CeSi₂ observed by photoemission. *Phys. Rev. Lett.*, 58:2810, 1987.
 - [110] F. Patthey, J. M. Imer, W. D. Schneider, H. Beck, Y. Baer, and B. Delley. High-resolution photoemission study of the low-energy excitations in 4f-electron system. *Phys. Rev. B*, 42:8864, 1990.
 - [111] C. Laubschat, E. Weschke, C. Holtz, M. Domke, O. Strebel, and G. Kaindl. Surface electronic structure of α -like Ce compounds. *Phys. Rev. Lett.*, 65:1639, 1990.
 - [112] E. Weschke, C. Laubschat, T. Simmons, M. Domke, O. Strebel, and G. Kaindl. Surface and bulk electronic structure of Ce metal studied by high-resolution resonant photoemission. *Phys. Rev. B*, 44:8304, 1991.
 - [113] D. Ehm, S. Hufner, F. Reinert, J. Kroha, P. Wolffe, O. Stockert, C. Geibel, and H. V. Lohneysen. High-resolution photoemission study on low- t_K Ce systems: Kondo resonance, crystal field structures, and their temperature dependence. *Phys. Rev. B*, 76:045117, 2007.

- [114] E. Wuilloud, H. R. Moser, W. D. Schneider, and Y. Baer. Electronic structure of γ - and α -ce. *Phys. Rev. B*, 28:7354, 1983.
- [115] K. A. Gschneidner and L. Eyring. *Handbook on the Physics and Chemistry of the Rare Earths*. North-Holland, Amsterdam, 1987.
- [116] K. Nagaoka, T. Jamneala, M. Grobis, and M. F. Crommie. Temperature dependence of a single Kondo impurity. *Phys. Rev. Lett.*, 88:077205, 2002.
- [117] N. Knorr, M. A. Schneider, L. Diekhoner, P. Wahl, and K. Kern. Kondo effect of single Co adatoms on Cu surfaces. *Phys. Rev. Lett.*, 88:096804, 2002.
- [118] M. A. Schneider, L. Vitali, N. Knorr, and K. Kern. Observing the scattering phase shift of isolated Kondo impurities at surfaces. *Phys. Rev. B*, 65:121406, 2002.
- [119] P. Wahl, L. Diekhoner, M. A. Schneider, L. Vitali, G. Wittich, and K. Kern. Kondo temperature of magnetic impurities at surfaces. *Phys. Rev. Lett.*, 93:176603, 2004.
- [120] L. Limot and R. Berndt. Kondo effect and surface-state electrons. *Appl. Surf. Sci.*, 237:576, 2004.
- [121] P. Wahl, L. Diekhoner, G. Wittich, L. Vitali, M. A. Schneider, and K. Kern. Kondo effect of molecular complexes at surfaces: Ligand control of the local spin coupling. *Phys. Rev. Lett.*, 95:166601, 2005.
- [122] M. A. Schneider, L. Vitali, P. Wahl, N. Knorr, L. Diekhoner, G. Wittich, M. Vogelgesang, and K. Kern. Kondo state of Co impurities at noble metal surfaces. *Appl. Phys. A*, 80:937, 2005.
- [123] P. Gentile, L. de Leo, M. Fabrizio, and E. Tosatti. Ferromagnetic Kondo effect at nanocontacts. page arXiv:0902.0254v1, 2009.
- [124] J. H. Osiecki and E. F. Ullman. Studies of free radicals. I. alpha-nitronyl nitroxides, a new class of stable radicals. *J. Am. Chem. Soc.*, 90:1078, 1968.
- [125] M. Tamura, Y. Nakazawa, D. Shiomi, K. Nozawa, Y. Hosokoshi, M. Ishikawa, M. Takahashi, and M. Kinoshita. Bulk ferromagnetism in the β -phase crystal of the *p*-nitrophenyl nitronyl nitroxide radical. *Chem. Phys. Lett.*, 186:401, 1991.
- [126] E. L. Wolf and D. L. Losee. *g*-shifts in the "s-d" exchange theory of zero-bias tunneling anomalies. *Phys. Lett. A*, 29:334, 1969.
- [127] T. Choi, C. D. Ruggiero, and J. A. Gupta. Tunneling spectroscopy of ultrathin insulating Cu₂N films, and single Co adatoms. *J. Vac. Sci. Technol. B*, 27:887, 2009.
- [128] T. Choi, M. Badal, S. Loth, J.-W. Yoo, C. P. Lutz, A. J. Heinrich, A. J. Epstein, D. G. Stroud, and J. A. Gupta. Magnetism in single metalloorganic complexes formed by atom manipulation. *Nano Lett.*, 14:1196, 2014.
- [129] B. Bryant, R. Toskovic, A. Ferrón, J. L. Lado, A. Spinelli, J. Fernández-Rossier, and A. F. Otte. Controlled complete suppression of single-atom inelastic spin and orbital cotunneling. *Nano Lett.*, 15:6542, 2015.
- [130] R. Toskovic, R. van den Berg, A. Spinelli, I. S. Eliens, B. van den Toorn, B. Bryant, J.-S. Caux, and A. F. Otte. Atomic spin-chain realization of a model for quantum criticality. *Nature Physics*, 12:656, 2016.
- [131] R. Bulla, T. A. Costi, and Th. Pruschke. Numerical renormalization group method for quantum impurity systems. *Rev. Mod. Phys.*, 80:395, 2008.
- [132] F. Delgado and J. Fernández-Rossier. Storage of classical information in quantum spins. *Phys. Rev. Lett.*, 108:196602, 2012.
- [133] H. Suhl. Dispersion theory of the Kondo effect. *Phys. Rev.*, 138:A515, 1965.
- [134] Y. Nagaoka. Self-consistent treatment of Kondo's effect in dilute alloys. *Phys. Rev.*, 138:A1112, 1965.
- [135] P. B. Wiegmann. Exact solution of *s* – *d* exchange model at *T* = 0. *Sov. Phys. JETP*, 31:392, 1980.
- [136] T. A. Costi. Kondo effect in a magnetic field and the magnetoresistivity of Kondo alloys. *Phys. Rev. Lett.*, 85:1504, 2000.
- [137] R. Zitko, R. Peters, and Th. Pruschke. Splitting of the Kondo resonance in anisotropic magnetic impurities on surfaces. *New J. Phys.*, 11:053003, 2009.
- [138] M. Tinkham. *Introduction to Superconductivity*. McGraw-Hill, New York, 1985.
- [139] P. Nozières. A "Fermi-liquid" description of the Kondo problem at low temperatures. *J. Low Temp. Phys.*, 17:31, 1974.
- [140] H. O. Frota. Shape of the Kondo resonance. *Phys. Rev. B*, 45:1096, 1992.
- [141] H. Prüser, M. Wenderoth, P. E. Dargel, A. Weismann, R. Peters, Th. Pruschke, and R. G. Ulbrich. Long-range Kondo signature of a single magnetic impurity. *Nature Physics*, 7:203, 2011.
- [142] R. Zitko. Kondo resonance lineshape of magnetic adatoms on decoupling layers. *Phys. Rev. B*, 84:195116, 2011.
- [143] U. Fano. Effects of configuration interaction on intensities and phase shifts. *Phys. Rev.*, 124:1866, 1961.
- [144] O. Ujsaghy, J. Kroha, L. Szunyogh, and A. Zawadowski. Theory of the Fano resonance in the STM tunneling density of states due to a single Kondo impurity. *Phys. Rev. Lett.*, 85:2557, 2000.
- [145] S. M. Cronenwett, T. H. Oosterkamp, and L. P. Kouwenhoven. A tunable Kondo effect in quantum dots. *Science*, 281:540, 1998.
- [146] X. Chen, Y. S. Fu, S.-H. Ji, T. Zhang, P. Cheng, X. C. Ma, X.-L. Zou, W. H. Duan, J. F. Jia, and Q. K. Xue. Probing superexchange interaction in molecular magnets by spin-flip spectroscopy and microscopy. *Phys. Rev. Lett.*, 101:197208, 2008.
- [147] K. R. Patton, S. Kettemann, A. Zhuravlev, and A. Lichtenstein. Spin-polarized tunneling microscopy and the Kondo effect. *Phys. Rev. B*, 76:100408, 2007.
- [148] A. C. Seridonio, F. M. Souza, and I. A. Shelykh. Spin-polarized STM for a Kondo adatom. *J. Phys.: Condens. Matter*, 21:095003, 2009.
- [149] Y. S. Fu, Q.-K. Xue, and R. Wiesendanger. Spin-resolved splitting of Kondo resonances in the presence of RKKY-type coupling. *Phys. Rev. Lett.*, 108:087203, 2012.
- [150] S. Loth, M. Etzkorn, C. P. Lutz, D. M. Eigler, and A. J. Heinrich. Measurement of fast electron spin relaxation times with atomic resolution. *Science*, 329:1628, 2010.

- [151] R. Meserve and P. M. Tedrow. Spin-polarized electron tunneling. *Phys. Rep.*, 238:173, 1994.
- [152] M. Eltschka, B. Jäck, M. Assig, O. V. Kondrashov, M. A. Skvortsov, M. Etzkorn, C. R. Ast, and K. Kern. Probing absolute spin polarization at the nanoscale. *Nano Lett.*, 14:7171, 2014.
- [153] J. R. Friedman and M. P. Sarachik. Single-molecule nanomagnets. *Ann. Rev. Cond. Mat. Phys.*, 1:109, 2010.
- [154] M. Cavallini, M. Faccini, C. Albonetti, and F. Biscarini. Single molecule magnets: from thin films to nano-patterns. *Phys. Chem. Chem. Phys.*, 10:784, 2008.
- [155] J. A. J. Burgess, L. Malavolti, V. Lanzilotto, M. Mannini, S. Yan, S. Ninova, F. Totti, S. Rolf-Pissarczyk, A. Cornia, R. Sessoli, and S. Loth. Magnetic fingerprint of individual Fe_4 molecular magnets under compression by a scanning tunnelling microscope. *Nature Comm.*, 6:8216, 2015.
- [156] F. Pineider, M. Mannini, R. Sessoli, A. Caneschi, D. Barreca, L. Armelao, A. Cornia, E. Tondello, and D. Gatteschi. Solvent effects on the adsorption and self-organization of Mn_{12} on Au(111). *Langmuir*, 23:11836, 2007.
- [157] S. Voss, O. Zander, M. Fonin, U. Rüdiger, M. Burgert, and U. Groth. Electronic transport properties and orientation of individual Mn_{12} single-molecule magnets. *Phys. Rev. B*, 78:155403, 2008.
- [158] M. Mannini, P. Saintcruvit, R. Sessoli, C. C. dit Moulin, F. Pineider, M.-A. Arrio, A. Cornia, and D. Gatteschi. XAS and XMCD investigation of Mn_{12} monolayers on gold. *Chem. Eur. J.*, 14:7530, 2008.
- [159] G. Rogez, B. Donnio, E. Terazzi, J.-L. Gallani, J.-P. Kappler, J. P. Bucher, and M. Drillon. The quest for nanoscale magnets: The example of $[\text{Mn}_{12}]$ single molecule magnets. *Adv. Mater.*, 21:4323, 2009.
- [160] A. Saywell, G. Magnano, C. J. Satterley, L. M. A. Perdigão, A. J. Britton, N. Taleb, M. del Carmen Gimenez-Lopez, N. R. Champness, J. N. O'Shea, and P. H. Beton. Self-assembled aggregates formed by single-molecule magnets on a gold surface. *Nature Comm.*, 1:75, 2010.
- [161] A. Hurley, N. Baadji, and S. Sanvito. Spin-flip inelastic electron tunneling spectroscopy in atomic chains. *Phys. Rev. B*, 84:035427, 2011.
- [162] J. Fernández-Rossier. Theory of single spin inelastic tunneling spectroscopy. *Phys. Rev. Lett.*, 102:256802, 2009.
- [163] A. Spinelli, B. Bryant, F. Delgado, J. Fernández-Rossier, and A. F. Otte. Imaging of spin waves in atomically designed nanomagnets. *Nature Materials*, 13:782, 2014.
- [164] A. Spinelli, M. P. Rebergen, and A. F. Otte. Atomically crafted spin lattices as model systems for quantum magnetism. *J. Phys.: Condens. Matter*, 27:243203, 2015.
- [165] S. Loth, S. Baumann, C. P. Lutz, D. M. Eigler, and A. J. Heinrich. Bistability in atomic-scale antiferromagnets. *Science*, 335:196, 2012.
- [166] S. Yan, L. Malavolti, J. A. J. Burgess, and S. Loth. Non-locally sensing the spin states of individual atomic-scale nanomagnets. *arXiv:1601.02723 [cond-mat.mes-hall]*, 2016.
- [167] A. A. Khajetoorians, M. Steinbrecher, M. Ternes, M. Bouhassoune, S. Lounis, M. dos Santos Dias, J. Wiebe, and R. Wiesendanger. Tailoring the chiral magnetic interaction between two individual atoms. *Nature Comm.*, 7:10620, 2016.
- [168] M. Muenks, P. Jacobson, M. Ternes, and K. Kern. Correlation driven transport asymmetries through coupled spins in a tunneling junction. *Nature Comm.*, 8:14119, 2017.
- [169] B. A. Jones and C. M. Varma. Study of two magnetic impurities in a Fermi gas. *Phys. Rev. Lett.*, 58:843, 1987.
- [170] B. A. Jones, C. M. Varma, and J. W. Wilkins. Low-temperature properties of the two-impurity Kondo Hamiltonian. *Phys. Rev. Lett.*, 61:125, 1988.
- [171] B. A. Jones and C. M. Varma. Critical point in the solution of the two magnetic impurity problem. *Phys. Rev. B*, 40:324, 1989.
- [172] R. Sessoli, D. Gatteschi, A. Caneschi, and M. A. Novak. Magnetic bistability in a metal-ion cluster. *Nature*, 365:141, 1993.
- [173] Z. Ouyang, Z. Takáts, T. A. Blake, B. Gologan, A. J. Guymon, J. M. Wiseman, J. C. Oliver, V. J. Davisson, and R. G. Cooks. Preparing protein microarrays by soft-landing of mass-selected ions. *Science*, 301:1351, 2003.
- [174] S. Rauschenbach, F. L. Stadler, E. Lunedei, N. Malinowski, S. Koltsov, G. Constantini, and K. Kern. Electrospray ion beam deposition of clusters and biomolecules. *Small*, 2:540, 2006.
- [175] S. Rauschenbach, R. Vogelgesang, N. Malinowski, J. W. Gerlach, M. Benyoucef, G. Costantini, Z. Deng, N. Thontasen, and K. Kern. Electrospray ion beam deposition: Soft-landing and fragmentation of functional molecules at solid surfaces. *ACS Nano*, 3:2901, 2009.
- [176] G. E. Johnson, Q. Hu, and J. Laskin. Soft landing of complex molecules on surfaces. *Ann. Rev. Anal. Chem.*, 4:83, 2011.
- [177] S. Rauschenbach, M. Ternes, L. Harnau, and K. Kern. Mass spectrometry as a preparative tool for the surface science of large molecules. *Ann. Rev. Anal. Chem.*, 9:473, 2016.
- [178] M. I. Katsnelson, V. V. Dobrovitski, and B. N. Harmon. Many-spin interactions and spin excitations in Mn_{12} . *Phys. Rev. B*, 59:6919, 1999.
- [179] I. E. Dzyaloshinskii. Thermodynamic theory of weak ferromagnetism in antiferromagnetic substances. *J. Exp. Theor. Phys.*, 5:1259, 1957.
- [180] T. Moriya. Anisotropic superexchange interaction and weak ferromagnetism. *Phys. Rev.*, 120:91, 1960.
- [181] M. B. Plenio and S. Virmani. An introduction to entanglement measures. *Quant. Inform. Proc.*, 7:1, 2007.
- [182] R. Horodecki, P. Horodecki, M. Horodecki, and K. Horodecki. Quantum entanglement. *Rev. Mod. Phys.*, 81:865, 2009.
- [183] X.-W. Hou, M.-F. Wan, and Z.-Q. Ma. Dynamical correlations of negativity and entropy for pure and mixed states in two coupled quartic oscillators. *Eur. Phys. J. D*, 62:279, 2011.
- [184] C. H. Bennett, G. Brassard, S. Popescu, B. Schumacher, J. A. Smolin, and W. K. Wootters. Purification of noisy entanglement and faithful teleportation via noisy channels. *Phys. Rev. Lett.*, 76:722, 1996.
- [185] B. Schumacher. Quantum coding. *Phys. Rev. A*, 51:2738, 1995.

- [186] J. I. Kim, M. C. Nemes, A. F. R. de Toledo Piza, and H. E. Borges. Perturbative expansion for coherence loss. *Phys. Rev. Lett.*, 77:207, 1996.
- [187] V. Vedral, M. B. Plenio, M. A. Rippin, and P. L. Knight. Quantifying entanglement. *Phys. Rev. Lett.*, 78:2275, 1997.
- [188] S. Hill and W. K. Wootters. Entanglement of a pair of quantum bits. *Phys. Rev. Lett.*, 78:5022, 1997.
- [189] V. Coffman, J. Kundu, and W. K. Wootters. Distributed entanglement. *Phys. Rev. A*, 61:052306, 2000.
- [190] T. J. Osborne and F. Verstraete. General monogamy inequality for bipartite qubit entanglement. *Phys. Rev. Lett.*, 96:220503, 2006.
- [191] A. Peres. Separability criterion for density matrices. *Phys. Rev. Lett.*, 77:1413, 1996.
- [192] K. Życzkowski, P. Horodecki, A. Sanpera, and M. Lewenstein. Volume of the set of separable states. *Phys. Rev. A*, 58:883, 1998.
- [193] G. Vidal and R. F. Werner. Computable measure of entanglement. *Phys. Rev. A*, 65:032314, 2002.
- [194] P. Horodecki. Separability criterion and inseparable mixed states with positive partial transposition. *Phys. Lett. A*, 232:333, 1997.
- [195] K. Audenaert, J. Eisert, M. B. Plenio, and R. F. Werner. Entanglement properties of the harmonic chain. *Phys. Rev. A*, 66:042327, 2002.
- [196] P. P. Baruselli, R. Requist, M. Fabrizio, and E. Tosatti. Ferromagnetic Kondo effect in a triple quantum dot system. *Phys. Rev. Lett.*, 111:047201, 2013.
- [197] J. Voit. One-dimensional Fermi liquids. *Rep. Prog. Phys.*, 58:977, 1995.
- [198] S. Yan, D.-J. Choi, J. A. J. Burgess, S. Rolf-Pissarczyk, and S. Loth. Control of quantum magnets by atomic exchange bias. *Nature Nanotechnology*, 10:40, 2015.
- [199] W. Chen, T. Jamneala, V. Madhavan, and M. F. Crommie. Disappearance of the Kondo resonance for atomically fabricated cobalt dimers. *Phys. Rev. B*, 60:R8529, 1999.
- [200] P. Wahl, P. Simon, L. Diekhöner, V. S. Stepanyuk, P. Bruno, M. A. Schneider, and K. Kern. Exchange interaction between single magnetic adatoms. *Phys. Rev. Lett.*, 98:056601, 2007.
- [201] J. Bork, Y. Zhang, L. Diekhöner, L. Borda, J. Kroha, P. Wahl, and K. Kern. A tunable two-impurity Kondo system in an atomic point contact. *Nature Physics*, 7:901, 2011.
- [202] T. Esat, B. Lechtenberg, T. Deilmann, C. Wagner, P. Krüger, R. Temirov, M. Rohlfing, F. B. Anders, and F. S. Tautz. A chemically driven quantum phase transition in a two-molecule Kondo system. *Nature Physics*, 12:867, 2016.
- [203] C. Jayaprakash, H. R. Krishna-Murthy, and J. W. Wilkins. Two-impurity Kondo problem. *Phys. Rev. Lett.*, 47:737, 1981.
- [204] J. B. Silva, W. L. C. Lima, W. C. Oliveira, J. L. N. Mello, L. N. Oliveira, and J. W. Wilkins. Particle-hole asymmetry in the two-impurity Kondo model. *Phys. Rev. Lett.*, 76:275, 1996.
- [205] P. Simon, R. López, and Y. Oreg. Ruderman-Kittel-Kasuya-Yosida and magnetic-field interactions in coupled Kondo quantum dots. *Phys. Rev. Lett.*, 94:086602, 2005.
- [206] L. G. G. V. Dias da Silva, N. P. Sandler, K. Ingersent, and S. E. Ulloa. Zero-field Kondo splitting and quantum-critical transition in double quantum dots. *Phys. Rev. Lett.*, 97:096603, 2006.
- [207] R. Zitko and Th. Pruschke. Many-particle effects in adsorbed magnetic atoms with easy-axis anisotropy: the case of Fe on the CuN/Cu(100) surface. *New J. Phys.*, 12:063040, 2010.
- [208] T. Jabbens, N. Grewe, and S. Schmitt. Spectral properties of the two-impurity Anderson model with varying distance and various interactions. *Phys. Rev. B*, 85:045133, 2012.
- [209] A. K. Mitchell, E. Sela, and D. E. Logan. Two-channel Kondo physics in two-impurity Kondo models. *Phys. Rev. Lett.*, 108:086405, 2012.
- [210] N. J. Craig, J. M. Taylor, E. A. Lester, C. M. Marcus, M. P. Hanson, and A. C. Gossard. Tunable nonlocal spin control in a coupled-quantum dot system. *Science*, 304:565, 2004.
- [211] D. Y. Baines, T. Meunier, D. Mailly, A. D. Wieck, C. Bäuerle, L. Saminadayar, P. S. Cornaglia, G. Usaj, C. A. Balseiro, and D. Feinberg. Transport through side-coupled double quantum dots: From weak to strong interdot coupling. *Phys. Rev. B*, 85:195117, 2012.
- [212] H. Prüser, P. E. Dargel, M. Bouhassoune, R. G. Ulbrich, Th. Pruschke, S. Lounis, and M. Wenderoth. Interplay between the Kondo effect and the Ruderman-Kittel-Kasuya-Yosida interaction. *Nature Comm.*, 5:5417, 2014.
- [213] H. Bethe. Zur Theorie der Metalle. I. Eigenwerte und Eigenfunktionen der linearen Atomkette. *Z. Für Phys.*, 71:205, 1931.
- [214] P. W. Anderson. An approximate quantum theory of the antiferromagnetic ground state. *Phys. Rev.*, 86:694, 1952.
- [215] R. Kubo. The spin-wave theory of antiferromagnetics. *Phys. Rev.*, 87:568, 1952.
- [216] T. Balashov, A. F. Takacs, W. Wulfhekkel, and J. Kirschner. Magnon excitation with spin-polarized scanning tunneling microscopy. *Phys. Rev. Lett.*, 97:187201, 2006.
- [217] E. Lieb, T. Schulz, and D. Mattis. Two soluble models of an antiferromagnetic chain. *Ann. Phys. (N. Y.)*, 16:407, 1961.
- [218] F. D. M. Haldane. Nonlinear field theory of large-spin Heisenberg antiferromagnets: Semiclassically quantized solitons of the one-dimensional easy-axis Néel state. *Phys. Rev. Lett.*, 50:1153, 1983.
- [219] I. Affleck. Quantum spin chains and the Haldane gap. *J. Phys.: Condens. Matter*, 1:3047, 1989.
- [220] F. Delgado, C. D. Batista, and J. Fernández-Rossier. Local probe of fractional edge states of $S = 1$ Heisenberg spin chains. *Phys. Rev. Lett.*, 111:167201, 2013.
- [221] J. P. Gauyacq and N. Lorente. Excitation of spin waves by tunneling electrons in ferromagnetic and antiferromagnetic spin-1/2 Heisenberg chains. *Phys. Rev. B*, 83:035418, 2011.
- [222] J. P. Gauyacq and N. Lorente. Magnetic excitation by tunneling electrons of frustrated ferromagnetic spin-1/2 chains and rings. *Phys. Rev. B*, 84:085415, 2011.

- [223] D.-J. Choi, R. Robles, J.-P. Gauyacq, M. Ternes, S. Loth, and N. Lorente. Structural and magnetic properties of FeMn_x ($x = 1 \dots 6$) chains supported on $\text{Cu}_2\text{N}/\text{Cu}$ (100). *Phys. Rev. B*, 94:085406, 2016.
- [224] W. H. Zurek. Decoherence, einselection, and the quantum origins of the classical. *Rev. Mod. Phys.*, 75:715, 2003.
- [225] F. Delgado, S. Loth, M. Zielinski, and J. Fernández-Rossier. The emergence of classical behavior in magnetic adatoms. *Europhys. Lett.*, 109:57001, 2015.